TAL
TECH

DOCTORAL THESIS

Hierarchically Structured Functional Ceramic Composites with Graphene Augmented Nanofibers

Ali Saffarshamshirgar

Hierarchically Structured Functional Ceramic Composites with Graphene Augmented Nanofibers

ALI SAFFARSHAMSHIRGAR

TALLINN UNIVERSITY OF TECHNOLOGY
School of Engineering
Department of Mechanical and Industrial Engineering
This dissertation was accepted for the defence of the degree 29/06/2021

Supervisor: Dr. Irina Hussainova, Professor
        School of Engineering
        Department of Mechanical and Industrial Engineering
        Tallinn University of Technology
        Tallinn, Estonia

Opponents: Dr. Iwona Jasiuk, Professor
        Department of Mechanical Science and Engineering
        University of Illinois at Urbana-Champaign
        1206 West Green Street, Room 2101C MEL
        Urbana, IL 61801, USA

        Dr. Tanel Tätte, Associate Professor
        Institute of Physics
        University of Tartu,W. Ostwaldi 1-D304
        Tartu, Estonia

Defence of the thesis: 26/08/2021, Tallinn

Declaration:
Hereby I declare that this doctoral thesis, my original investigation and achievement, submitted for the doctoral degree at Tallinn University of Technology has not been submitted for doctoral or equivalent academic degree.

Ali Saffarshamshirgar

_____
           signature

European Union
European Regional
Development Fund

Investing
in your future

Hierarhiliselt struktureeritud funktsionaalsed keraamilised komposiidid grafeenlisandiga nanokiududega

ALI SAFFARSHAMSHIRGAR

Dedicated to my family

Contents

List of publications

The PhD thesis is based on the following publications:

I **Saffar Shamshirgar, A.**, Rojas Hernández, R. E., Tewari, G. C., Ivanov, R., Mikli, V., Karppinen, M., & Hussainova, I. (2020). Layered structure of alumina/graphene-augmented-inorganic-nanofibers with directional electrical conductivity. Carbon, 167, 634–645. https://doi.org/10.1016/j.carbon.2020.06.038.

II Hussainova, I., **Saffar Shamshirgar, A.**, Ivanov, R., Volobujeva, O., Romanov, A. E., & Gasik, M. (2020). Directional conductivity in layered alumina. Current Applied Physics. https://doi.org/10.1016/j.cap.2020.06.009.

III **Saffar Shamshirgar, A.**, Rojas Hernández, R. E., Tewari, G. C., Fernández, J. F., Ivanov, R., Karppinen, M., & Hussainova, I. (2021). Functionally Graded Tunable Microwave Absorber with Graphene-Augmented Alumina Nanofibers. ACS Applied Materials & Interfaces, acsami.1c02899. https://doi.org/10.1021/acsami.1c02899.

IV **Saffar Shamshirgar, A.**, Belmonte, M., Tewari, G. C., Rojas Hernández, R. E., Seitsonen, J., Ivanov, R., Miranzo, P., Karppinen, M., & Hussainova, I. (2021). Thermal Transport and Thermoelectric Effect in Composites of Alumina and Graphene-Augmented Alumina Nanofibers. Materials, 14(9), 2242. https://doi.org/10.3390/ma14092242.

Author's contribution to the publications

Contribution to the papers:

I First author. Methodology. Design of experiments. Preparation of precursors and test specimens. Conducting experiments. Formal analysis. Data analysis. Discussion of the results. Manuscript preparation.

II Methodology. Preparation of precursors and test specimens. Conducting experiments. Data analysis. Discussion of the results. Manuscript preparation.

III First author. Methodology. Design of experiments. Preparation of precursors and test specimens. Conducting experiments. Formal analysis. Data analysis. Discussion of the results. Manuscript preparation.

IV First and corresponding author. Methodology. Design of experiments. Preparation of precursors and test specimens. Conducting experiments. Formal analysis. Data analysis. Discussion of the results. Manuscript preparation.

Introduction

Intensive interest in graphene and graphene related materials has been centered on their remarkable properties, which offer unique opportunities to address ever-increasing global demand of functional materials. The past years have witnessed considerable advances in the fabrication of graphene-based materials and significant breakthroughs in advanced applications. Nanotechnology has facilitated the development of graphene-based hybrid and composite materials with extraordinary performance and properties. Many reports have shown significant potentials and a wide variety of possible applications of carbon structures in optics, quantum devices, photocatalysis, photovoltaics, thermal management, etc.

One of the areas that graphene-based nanomaterials have recently entered in is microwave absorption using nanoscale-modified heterostructures. Many applications such as antenna designs, and microelectronics, require materials to interact with microwave radiations in a certain fashion, namely broadband absorption or filtering a narrow bandwidth of the frequencies. These applications often pose further constraints on the functionality of the materials, such as geometrical requirements, operational frequency, system compatibility, and structural integrity. To mitigate these often mutually exclusive requirements, most material inventions for microwave absorption are of nanoscale. It has been well-proven, that continuous progress in development of new multifunctional nanomaterials and understanding their dielectric and magnetic interactions, especially at gigahertz range is imperative to the technological advancements such as 5G and 6G network development. In such regards, carbon nanostructures such as carbon nanotubes, carbon fibers, graphene, and graphene related materials are the bedrocks of the inventions. Among them, graphene has shown a vast potential for advanced high performance microwave absorption. In various forms of graphene related materials, several polarization mechanisms such as defect polarization-relaxation, electronic dipole relaxation, etc. can be simultaneously present, which greatly increase microwave absorption performance. Furthermore, much effort has been devoted to the fabrication of nanocomposites that host graphene related materials to enforce synergetic effect of additional space charge polarization and multiple internal reflection to enhance the performance even further. These nanocomposites can be designed to serve as advanced multifunctional structures that combine mechanical, thermal, electrical, and chemical requirements of the system.

Acknowledging the importance of the topic, this work is devoted to development and study of novel multifunctional graphene-ceramic nanocomposites of a high-performance microwave absorption and further thermo-mechanical functionalities. The cornerstone of the work is the recently developed graphene augmented alumina nanofibers representing a great potential for microwave application due to their core-shell conductive-dielectric morphology and a unique band structure that has stemmed from the doping effect of the alumina and morphology of the graphene coating. Moreover, hierarchically structured nanocomposites, which employ the hybrid graphene-alumina nanofibers are proposed to complement the tunability of the absorber structure, enhance microwave absorption, and provide anisotropic thermal and electrical properties. In addition, the alumina matrix used in this work, can ensure the mechanical reliability of the developed hierarchical structures which can render them excellent choices for harsh environments.

Abbreviations

ALD	Atomic Layer Deposition
ANF	Alumina Nanofiber
CMC	Ceramic Matrix Composite
CNT	Carbon Nanotube
CVD	Chemical Vapor Deposition
EM	Electro-Magnetic
EMI	Electro-Magnetic Interference
EMI SE	Electro-Magnetic Interference Shielding Effectiveness
fcc	Face-Centered Cubic
FESEM	Field Emission Scanning Electron Microscope
FSM	Fibonacci Sequenced Multilayer
GAIN	Graphene Augmented Inorganic Nanofibers
GO	Graphene Oxide
GRM	Graphene Related Materials
hBN	Hexagonal Boron Nitride
hcp	Hexagonal Closed-Packed
HR-TEM	High Resolution Transmission Electron Microscope
HV	Hardness Value (Vicker's Hardness)
MAM	Microwave Absorbing Material
MFP	Mean Free Path
MWCNT	Multi-Walled Carbon Nanotube
N-doped	Nitrogen doped
NRW	Nicolson-Ross-Weir
PEC	Perfect Electric Conductor
PPMS	Physical Property Measurement System
RF	Radio Frequency
rGO	Reduced Graphene Oxide
RL	Reflection Loss
sccm	Standard cubic centimeters per minute
SEA	Shielding Effectiveness Due to Absorption
SEM	Scanning Electron Microscope
SER	Shielding Effectiveness Due to Reflection
SPS	Spark Plasma Sintering
SWCNT	Single-Walled Carbon Nanotube
TE	Thermoelectric
TE10	Transverse Electric
TPS	Transient Plane Source
Vol.%	Volume percentage
WR-90	Rectangular Waveguide 90

Wt.%	Weight percentage
XRD	X-Ray Diffraction
ZT	Thermoelectric Figure of Merit

Symbols

ε	Permittivity
ε''	Dielectric loss factor
μ	Permeability
μ	Carrier mobility
n	Carrier density/concentration
Ω	Resistance
σ	Electrical conductivity
ρ	Resistivity
C_p	Specific heat capacity
Tan δ_ε	Dielectric loss tangent
Tan δ_μ	Magnetic loss tangent
k	Thermal conductivity
α	Thermal diffusivity
λ	Phonon mean free path
$\perp$	Perpendicular direction (through-plane)
$\parallel$	Parallel direction (in-plane)
CH_4	Methane
H_2	Hydrogen
N_2	Nitrogen
γ	Propagation constant
η	Characteristic impedance
Z_0	Impedance of free space
Z_{in}	Input impedance
p	Power

1 Review of the literature

This chapter provides state of the art of the performed research in the area of graphene-ceramic composites, their properties, routes of sintering, as well as the mechanisms of thermal, and electrical transport related to the presence of carbon nanostructures in the materials. Moreover, an overview of electromagnetic interference shielding with a focus on carbon-based microwave absorbers is provided.

1.1 Ceramic matrix composites

Ceramic matrix composites (CMCs) are usually materials that provide the desirable set of properties combining excellent mechanical properties and chemical inertness of a ceramic matrix with specific properties of the additives (Bansal & Lamon, 2003). CMCs are considered as inverse composites, that is to say the brittle ceramic matrix is the first to fail under load. Hence, the filler reinforcement in such structures arrest and/or deflect cracks at the filler-matrix interface to reduce brittle failure of the composite (Krenkel & Renz, 2008). The crack trajectory deflection at the interface is achieved through weakening of the interface by employing a thin interphase layer, functioning as mechanical fuse. Examples are hexagonal boron nitride (hBN) and pyrolytic carbon (Krenkel & Renz, 2008). For fiber reinforced CMCs, oxide fibers (such as alumina), despite having excellent oxidation resistant and mechanical properties are less desirable over carbon and SiC based fibers due to their high creep rates. Therefore, coating interfaces such as monazite (LaPO$_4$), ZrO$_2$, TiO$_2$, and layered perovskites on various oxide fibers, create a more effective, even though more complex, reinforcement (Bansal & Lamon, 2003). Recently, the nanostructured carbon-alumina hybrid fibers as an emerging area has shown a vast potential for optimization of the bulk composite properties (Ivanov et al., 2015). In addition to mechanical properties of CMCs, by employing ferroelectrics, piezoelectrics, ion-conductors, and optical ceramics, CMCs have been tuned for electrical, thermal, electromagnetic, and catalytic applications (Phelps & Wachtman, 2000).

1.1.1 Alumina phases

Aluminum oxide (Alumina, Al$_2$O$_3$) is one of the most widely used technical ceramics and industry standard for electronic substrates due to its low production costs as well as high strength, maximum service temperature, relatively low chemical inertness, low electrical resistivity, and low dielectric loss factor (ε''). Alumina has a broad range of applications in cutting tools, gas purifications systems, and radio frequency (RF) window materials (de Faoite, Browne, Chang-Díaz, & Stanton, 2012). Besides the thermodynamically stable α-Al$_2$O$_3$, several metastable polymorphs of alumina can be divided into two main categories: (I) face-centered cubic (fcc) and (II) hexagonal close-packed (hcp). The distribution of oxygen anions follows the main two crystal structures; therefore, the distribution of the cations makes up the subgroup metastable polymorphs. The fcc subgroup (also known as transition polymorphs) includes cubic γ and η, monoclinic θ, and tetragonal or orthorhombic δ phases. In the **Figure 1.1**a–d the hcp position of oxygen atoms and cubic structured oxygen and aluminum atoms are shown for α and γ, respectively. In crystallography terms, α-Al$_2$O$_3$ has a trigonal symmetry with rhombohedral Bravais centering with a space group R-c (number 167 in (Bradly & Cracknell, 1972)). The metastable γ-Al$_2$O$_3$ with O atoms in cubic close-packed arrangement and Al atoms occupying octahedral and tetrahedral sites is commonly accepted to have symmetry of ideal spinel (Levin & Brandon, 2005) with Fd-m (number 227 in (Bradly &

Cracknell, 1972)). The γ phase undergoes a transition process towards the more stable α-Al$_2$O$_3$ at temperature interval of 1050–1200 °C depending on the initial particle size and heating rates, through γ→δ→θ→α phase transformation sequence. This transition is one of the synthesis routes for preparation of commercial α-Al$_2$O$_3$ powder and fibers via thermal dehydration of a crystalline aluminum oxyhydroxide (boehmite, AlO(OH)) phase. The sequences of the phase transformation are not definitive. That is to say, neither experimental evidence show that δ→θ necessary happens, nor there is enough evidence to disprove a direct γ→α transition (Levin & Brandon, 2005). Nonetheless, it was shown that at around 950 °C partial transformation to δ phase begins which coexists with γ-Al$_2$O$_3$, while beyond that temperature, θ-Al$_2$O$_3$ and correspondingly θ→α occurs (Lamouri et al., 2017).
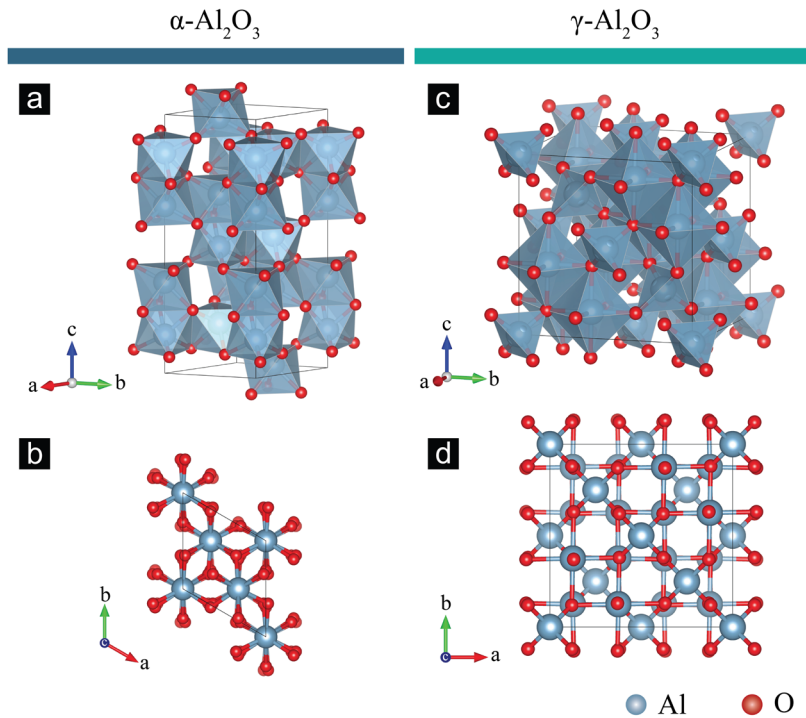

Figure 1.1 *Standard orientation and projections along [001] direction of (a,b) conventional unit cell of hexagonal α-Al$_2$O$_3$* (Lewis, Schwarzenbach, & Flack, 1982)*; and (b,c) cubic γ-Al$_2$O$_3$ phase* (L. Deyu, B.H. O'Connor, G.I.D Roach, 1990)*.*

1.1.2 Graphene

The two-dimensional sheet of *sp^2* hybridized carbon atoms possesses several extraordinary intrinsic properties such as extreme electron mobility (200000 cm^{2}v^{-1}s^{-1}), ultra-high modulus of elasticity (~1 TPa), and high thermal conductivity (~5000 Wm^{-1}K^{-1}), while being optically transparent with almost 98 % transmittance in visible region of the spectrum (Foa Torres, Roche, & Charlier, 2013). Since the isolation of monolayer graphene in 2004, various approaches have been developed to scale-up the production and improve the quality of the sheets (Geim & Novoselov, 2007). In general, the production methods consist of the top-down approach which starts with graphite, and the bottom-up approach which mostly relies on synthesis of graphene from hydrocarbon precursors for

low-cost production. Chemical vapor deposition (CVD) is one of the most widely used methods to deposit graphene sheets from methane (CH_4) on a variety of substrates. Most of these processes result in various forms of carbon structures such as bilayer, trilayer, and few-layer graphene (depending on the basal plane counts), 2D films, polycrystalline and nanocrystalline forms (depending on grain size), twisted graphene, and a number of unintentionally functionalized products containing OH groups or N atoms.

1.1.2.1 Graphene on oxide substrates

In general, evolution of CVD graphene takes place via two distinct processes: catalytic growth at high and low temperatures, and the high temperature spontaneous growth. The catalytic growth includes deposition on transition metal substrates such as Cu via surface adsorption and Ni via surface segregation or precipitation due to the difference in solubility of C atoms between the two (<0.001 on Cu,~1.3 on Ni at 1000 °C) (X. Li, Cai, Colombo, & Ruoff, 2009; Wu et al., 2012). However, these processes require further chemical treatment to transfer the grown sheets, through which often contamination and/or defects are introduced. The second approach is a transfer free deposition via spontaneous dehydration of the C precursor on a variety of oxide substrates. This includes deposition on sapphire, quartz, and SiO_2 at high temperature and on MgO and ZrO_2 at low temperature (J. Park, Lee, Choi, Hwang, & Song, 2015). The spontaneous dehydration of C precursor can be done on virtually any nonmetallic substrates that withstand high temperatures of hydrocarbon pyrolysis (1000 °C) without a need for a catalyst (Cole, Lindvall, & Yurgens, 2012).
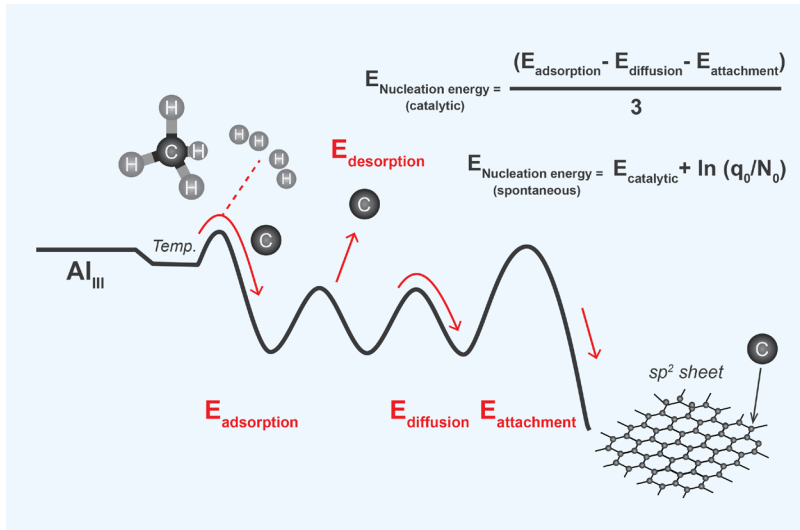
Figure 1.2 *Energy path for the sequence of graphene nucleation on γ-Al_2O_3 substrate via low temperature catalytic and high temperature spontaneous (non-catalytic) processes. The concept is adopted from (Park et al., 2015).*

Among the available oxide substrates, γ-Al_2O_3 offers a unique potential for graphene growth owing to its weak bonding with carbon and a promising application range due to its dielectric nature with a low leakage current density provided by its large band gap (~8.2 eV) (Tanner, Perng, Frewin, Saddow, & Chang, 2007). The highly reactive tricoordinated Al (Al_{III}) sites on the surface act as catalytic sites that lower the activation

energy for a surface-regulated nucleation and growth. These sites can accommodate decomposed C adatoms which attach themselves to sp^2 graphene rings via diffusion process (Lee, Park, Park, Choi, & Song, 2017). Recently, using hot-walled CVD, polycrystalline graphene was grown on γ-Al$_2$O$_3$ nanofibers and demonstrated a remarkable potential for various technological applications (Hussainova et al., 2015). **Figure 1.2** is a demonstration of the barriers on activation energy for graphene nucleation and sp^2 formation for low temperature catalytic growth and high temperature spontaneous dehydrogenation of CH$_4$.

1.1.3 Spark Plasma Sintering

Spark Plasma Sintering (SPS) is a sintering technology that combines uniaxial mechanical pressure and heating that is resulted from electrical discharge. In this approach, raw powder or pre-sintered green body is placed in a graphite die, mechanical pressure is applied onto the top and bottom punches, and DC current is passed through the die or the sample (depending on the resistivity of the sample). In many cases where the electrical conductivity of the sample (either at room temperature or at elevated temperature) is higher than the graphite die, current is forced through the sample, which results in local joule heating. This phenomenon, results in heating rates as high as 1000 °C/min. Therefore, SPS allows significantly faster sintering rates as compared to conventional convection based sintering approach, which often is a crucial consideration in sintering of ceramics as an effective measure to limit grain growth during densification (Guillon et al., 2014).

1.2 Graphene-ceramic nanocomposites

Since the introduction of graphene and carbon nanotubes, a significant interest in the topic of ceramic matrix composites added by graphene, graphene related materials (GRM), and CNTs has proven many possible applications. Ceramic precursors often bond with graphene at molecular level, creating hierarchical structures with anisotropic properties (Huang & Wan, 2020). It has been shown that graphene and GRMs such as graphene oxide (GO), reduced graphene oxide (rGO), and graphene nanoplatelets (GNP), as well as single-wall carbon nanotubes (SWCNT), and multi-wall carbon nanotubes (MWCNT) can act as reinforcing agents and fillers to provide electrical, thermal, chemical, and electromagnetic performance (Ramírez et al., 2021; Singh et al., 2011). In the following sections, a brief overview of the state of the art in the areas of thermal, thermoelectric, and microwave absorbing graphene-based composites is provided.

1.2.1 Thermal applications

Although there are similarities in phonon dispersion and crystal lattice inharmonicity of graphene and graphite, it has been experimentally shown that thermal transport is more efficient in graphene than in the basal planes of graphite (Balandin, 2011). The first reports on thermal conductivity of a suspended single-layer graphene have revealed a room temperature value of ~2000 W·m^{-1}·K^{-1} (Balandin et al., 2008). This is attributed to the fact that the mean free path (MFP) of the long-wavelength phonons in a 2D graphene sheet is only limited by the size of the graphene sheet and is experimentally proven to have logarithmic divergence to intrinsic values as the size increases (Xu et al., 2014). In other studies, it was observed that thermal transport crossover from 2D graphene to 3D graphite for few layer graphene when the number of layers change from 2 to ~8 (Balandin, 2011). This is explicitly related to the suppressed Umklapp scattering in single

layer graphene (limited only by the boundary scattering) which unlike for 3D systems, is insufficient for restoration of thermal equilibrium. This excellent property coupled with versatility of graphene and its related materials initiated a vast number of studies regarding the application of graphene in advanced thermal management (Malekpour & Balandin, 2018). CVD graphene coating on porous foams of Al_2O_3 have shown low sheet resistivity of 0.11 $\Omega \cdot sq^{-1}$ and thermal conductivity of 8.28 $W \cdot m^{-1} \cdot K^{-1}$ (Zhou et al., 2013). In a different work, (Zhang et al., 2017) have produced a hybrid material consisting of 3D graphene template coated by Al_2O_3 nanoparticles using atomic layer deposition (ALD). The remarkably lightweight resulting product has shown super-elastic response, electrical conductivity of 102 $S \cdot m^{-1}$ and insulating thermal conductivity of 0.05 $W \cdot m^{-1} \cdot K^{-1}$. Addition of 16 vol.% GNPs in the matrix of Si_3N_4 has resulted in an anisotropic thermal response with in-plane values reaching 40 $W \cdot m^{-1} \cdot K^{-1}$, twice the thermal conductivity of the matrix (Miranzo et al., 2012). In contrast, introducing GNP and CNT to the matrix of Al_2O_3 is often associated with a decrease in room temperature thermal conductivity (Çelik, Çelik, Flahaut, & Suvaci, 2016; Zhan & Mukherjee, 2005). However, by increasing the length of MWCNT to 1–7 µm, (Kumari et al., 2008) have obtained thermal conductivity value of ~90 $W \cdot m^{-1} \cdot K^{-1}$ at 100 °C for a composite with 7.39 wt.% of MWCNT in Al_2O_3 matrix sintered at 1550 °C. This increase was attributed to the increased MFP due to the high aspect ratio of the filler MWCNTs and reduced tube-tube interactions, which promoted a more dominant contribution of Umklapp scattering. It was also found that the thermal conductivity of such structures is highly dependent on the bulk density and sintering temperature (Kumari et al., 2008).

1.2.2 Thermoelectric applications

Tunability of graphene and GRMs has attracted attention in the field of thermoelectric (TE) materials. Thermoelectric energy harvesting is a technologically viable solution that utilizes Seebeck effect through which, a temperature gradient on two sides of a material is converted into a potential difference (voltage). The opposite of this process is called Peltier effect with applications in cooling systems. The efficiency of a thermoelectric material can be quantified by the dimensionless thermoelectric Figure of Merit (ZT) which is directly proportional to the Seebeck coefficient and electrical conductivity of the material; and is inversely proportional to its thermal conductivity (**Equation 1**). Therefore, a high efficiency can be achieved through designing a material with high Seebeck coefficient and electrical conductivity, while keeping thermal conductivity low. Though, the tradeoff that exists between the three properties makes the design challenging (Ju, Kim, Yook, Han, & Cho, 2019; Russ, Glaudell, Urban, Chabinyc, & Segalman, 2016). The magnitude of the Seebeck coefficient and value of electrical conductivity in a material are closely in connection with the shape of the density of states near the Fermi level. **Equation 2** shows the correlation of thermopower (Seebeck voltage, α) and Fermi energy (E_f). In this equation, K_B is the Boltzmann constant, T is the temperature, e is the elementary charge, and N(E) is the density of states.

$$ZT = \frac{\sigma S^2 T}{k} \qquad (1)$$

$$\alpha(E_f) = -\frac{\pi}{3}\frac{k_B}{e}k_B \left[\frac{\partial \ln[N(E)]}{\partial E}\right]_{E-E_f} \qquad (2)$$

In this regard, carbon family, in particular graphene and GRMs, offer promising potential for tuning their electronic properties to mitigate the requirements of a high efficiency TE material (Wei et al., 2020). Carrier density in graphene and GRMs can be precisely tuned to correspond to the optimal Seebeck coefficient and electrical conductivity following the $\sigma = ne\mu$ relationship and **Equation 1**. Introducing bandgap through doping, controlling carrier density, and Fermi engineering, all have direct influence on the Seebeck coefficient and subsequently ZT. Additionally, employing graphene and GRMs in the matrix of traditional TE materials, can decrease thermal conductivity of the host matrix by introducing interface scattering and thermal boundary resistance (Blackburn, Ferguson, Cho, & Grunlan, 2018). Figure 1.3 shows the correlation between various properties and carrier density in a TE material.
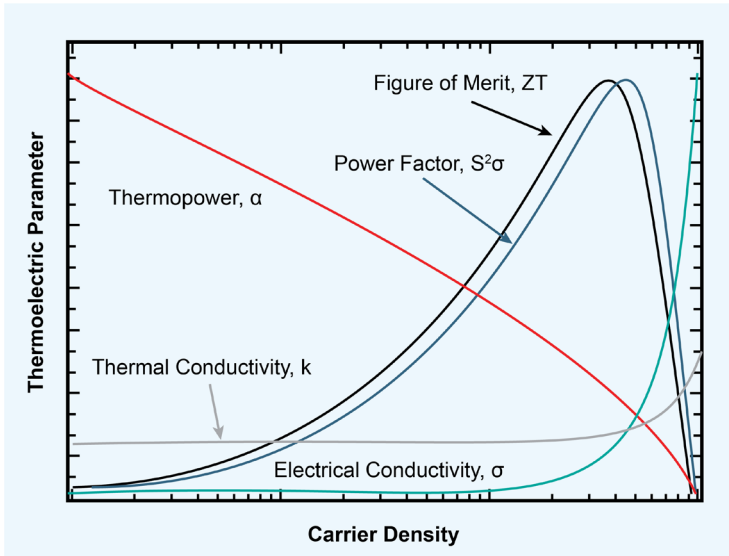

Figure 1.3 *Schematic depicting co-dependence of various TE properties on carrier density (over three orders of magnitude). The figure is reproduced with permission* (Blackburn et al., 2018)*.*

It is demonstrated that incorporation of rGO in undoped perovskite $SrTiO_3$ weakens the double Schottky barrier and thereby simultaneously increase carrier concentration and mobility (Rahman et al., 2019). It was shown that addition of 1 wt.% rGO to $SrTiO_3$ yields ZT of 0.25 at 1000 K (Srivastava et al., 2019). The ZT value of $SrTiO_3$ (0.22 at 800 K) was almost doubled by incorporation of 0.6 wt.% rGO which strongly prohibited the phonon transport and increased electrical conductivity (Okhay et al., 2019). Incorporation of 7 wt.% rGO in Si_3N_4 yielded ZT value of 0.09 at 300 K (Ramirez, Leborán, Rivadulla, Miranzo, & Osendi, 2016). (Ghosh, Harish, Ohtaki, & Saha, 2020) achieved ZT value of 0.01 at 300 K by incorporation of 10 wt.% graphene and ZnO in a cement composite.

1.2.3 Electromagnetic interference shielding and RF absorption

Electromagnetic (EM) radiations play a major role in everyday life. These radiations ranging from radio frequencies, through visible spectrum, to cosmic rays; are emitted by natural sources in cosmos such as the sun and artificial EM sources such as antennas and electronic devices. The ability to control the undesirable portion of these radiations

and channel them towards a safe path is an essential design requirement that its state-of-the-art must go hand in hand with technological advancements. EM interference (EMI) shielding is defined as the reduction in the power of the incident wave by one or combination of the three phenomena of reflection, absorption, and multiple internal reflections (**Figure 1.4**) (Sebastian, 2017). For most application, such as those in miniature devices, microelectronics, and antenna designs, absorption is the desired mode of shielding (H. Chen et al., 2019).
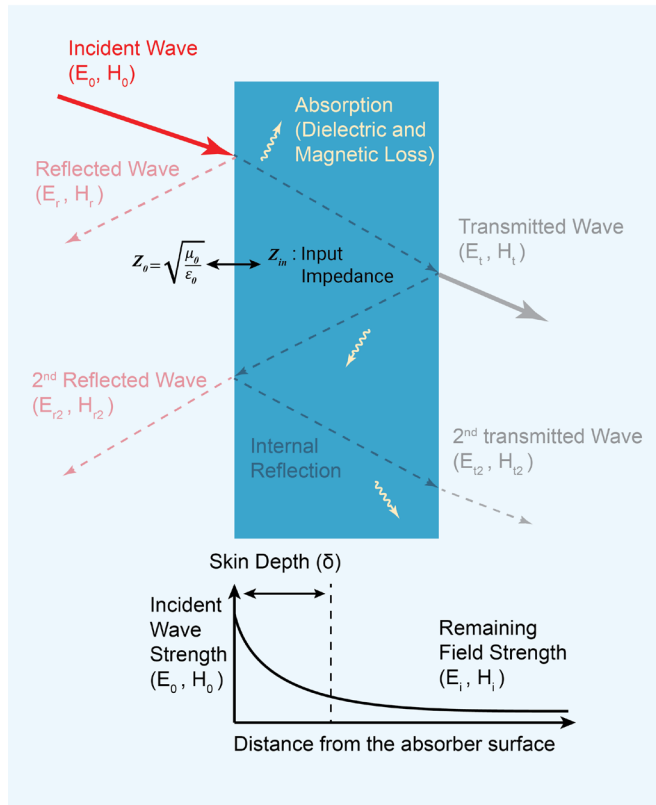

Figure 1.4 *Mechanisms of interaction of electromagnetic wave with matter.*

The challenge of designing an efficient EM absorber is embedded into the characteristic nature of EM radiations and their modes of interaction with matter. In fact, every portion of this wide range of wavelengths undergoes a different mode(s) of interaction/polarization while encountering matter. Therefore, to design a viable solution for EM absorption, one has to consider the bandwidth restrictions, and correspondingly, pick the right materials and structural geometries. Nowadays, with the extensive use of portable electronics and radio frequency developments such as 5G network, the microwave frequencies have become the most widely used frequency range for their applications in stealth, communications, and information technologies. Microwave absorption has recently emerged as an area of nanomaterial development since the intrinsic behavior of the microwave absorbing materials (MAMs) dictates their efficiency and modes of interaction with microwave radiations (Green & Chen, 2019). These materials often require functionalization at the nanoscale in order to tune their

permittivity and permeability to achieve the desired absorption efficiency. Microwave radiations can be attenuated by an external impact on their electric or magnetic component. The attenuation of the electric component can be done via atomic, electronic, orientational, and space charge polarizations, each having their own cut-off frequencies (**Figure 1.5**). Among them, space charge polarizations emanate from the presence of various interfaces in the structure such as composites, core-shell fillers, etc. Similarly, the magnetic component can be influenced by mechanisms of domain wall resonance, natural resonance, and eddy current loss (Green & Chen, 2019).
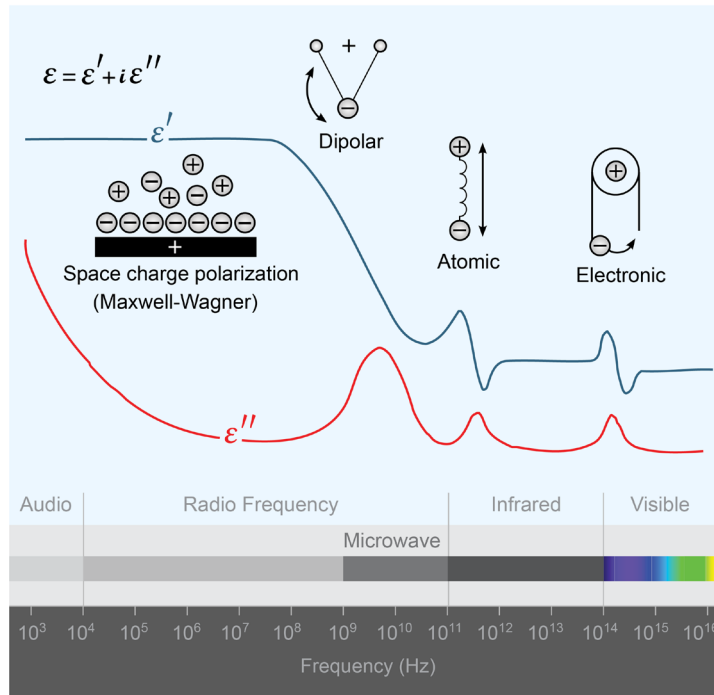

Figure 1.5 *Frequency dependence of dielectric polarizations.*

Due to their various response times, each of those phenomena are effective at certain frequency range (Sebastian, 2017). Therefore, a precise structuring and fine-tuning of the properties can give rise to high performance microwave absorbers that employ synergetic abilities to cover a broad range of spectrum. Specifically, the magnetic component is effective at the lower end of the microwave spectra <10 GHz, while at higher frequency range the dielectric loss is responsible for microwave absorption (Thomas, 2018). Carbon nanomaterials, including carbon nanotubes (CNT) (Shi & Liang, 2008) (Vázquez & Prato, 2009), carbon fibers (Rohini & Bose, 2019), nanocoils (Wang et al., 2012), graphene, and GRMs (H. Chen et al., 2019) are considered as competitive candidates for MAMs due to their outstanding features of lightweight, large specific surface area, physical and chemical stability, and excellent dielectric loss. In addition, embedding carbon-based fillers in ceramic matrix materials with low permittivity, promotes additional space-charge polarization, and multiple internal reflection, which can strongly improve absorption performance (Micheli, Apollo, Pastore, & Marchetti, 2010). (Yuchang, Qinlong, Fa, & Wancheng, 2016) tested a 1.5 mm composite with incorporation of 2 vol.% GNP in the matrix of Al_2O_3 at X-band. The result showed a -25 dB

narrowband absorption peak at ~10 GHz while temperature dependence test showed a full X-band 25 dB EMI shielding effectiveness (EMI SE) at 100 °C. It is worth noting that X-band is intensively employed for satellite communications, weather monitoring, terrestrial mapping, and radar applications. (C. Chen et al., 2018) embedded 2.5 vol.% graphene nanosheets in MgO matrix and obtained a full X-band -10dB absorption with a narrowband -36.5 dB peak centered at 10.7 GHz. Several other works have portrayed the significant potential of carbon structures such as graphene and GRMs embedded into ceramic matrices for EM absorption at microwave and terahertz frequencies (Delfini et al., 2018; Meng et al., 2018).

1.2.4 Multilayer and hierarchical structures

In addition to monolithic graphene-ceramic composite structures, double-layer and multilayer designs can help to reduce surface scattering and enhance absorption. In an ideal case of MAM, the surface impedance equals that of the free space ($Z_0 = Z_{in}$). If this condition is met, the surface reflection is avoided, and the entire power of the incident wave is transferred to the absorber (no surface scattering). Impedance matching is a technique that can be used as an effective tool by designing a lossless window layer on the surface that modulates the bulk's impedance. Addition of electrically conductive graphene and GRMs into dielectric matrices can decrease impedance of the bulks whose magnitudes are affected by the fillers' contents. As an impedance mismatch between the surface of an absorber and the impedance of the free space is the root cause of surface scattering, which limits power transfer to the absorber structure, an additional surface layer can match the impedance of the free space and minimize power loss at the surface (**Figure 1.6**a).
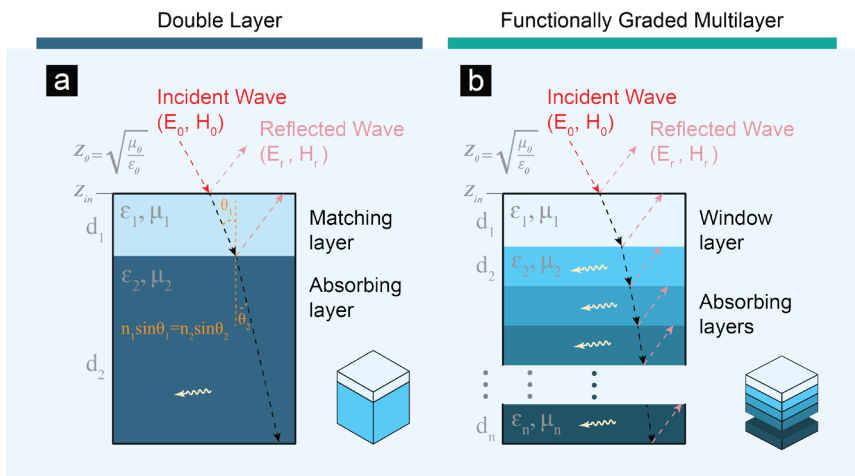
Figure 1.6 Microwave absorber designs (a) double layer; (b) functionally graded multilayer absorber. The dash lines are the representation of the EM field with electric (E) and magnetic (H) component propagating through the absorber layers.

Furthermore, when EM radiations encounter an absorber at angle θ_1, if the refractive index of the absorber (n_2) differ from the medium in which the radiations are propagating (n_1), a reflection phenomenon occurs that has angle θ_2 following Snell's law (**Figure 1.6**a). Design of a functionally graded multilayer structure, in which the conductive filler

content is gradually increasing on the path of the incoming incident wave, ensures an impedance gradient, which greatly enhances the attenuation ability of the bulk as a result of the efficient use of the entire cross-section of the bulk (**Figure 1.6**b).

A similar strategy was used to prepare multilayers of CNTs/SiO$_2$ with a gradient in CNT content comprising of 2.5 wt.%, 5 wt.%, 7.5 wt.%, and 10 wt.% layers. The X-band absorption result was compared to that of a homogenous composite sample with 5 wt.% CNTs. It was shown that the insertion loss stayed the same while absorption efficiency was greatly improved in the whole X-band (M. Chen et al., 2011). Graphene based microwave absorbers with multilayer structures can be tuned by tailoring the intrinsic properties of the utilized materials, controlling the composition of the layers, and tuning the thicknesses of the layers. This tuning ability allows designing high efficiency broadband or frequency specific composite microwave absorbers (W. Li et al., 2017; Mencarelli, Pierantoni, Stocchi, & Bellucci, 2016; Micheli et al., 2012; Panwar & Lee, 2019; K. Park, Lee, Kim, & Han, 2006; Ye et al., 2018).

1.3 Objectives of the study

This research was motivated by the pressing need for lightweight, cost-effective, and high-performance microwave absorbers. Graphene augmented alumina nanofibers (GAIN) represent a remarkable potential for applications as high-performance microwave absorbers, which stems from their core-shell conductive-dielectric-conductive morphology and intrinsic electronic properties of polycrystalline graphene. With the extensive use of the portable electronics and radio frequency developments such as 5G network, design and exploration of high-performance and lightweight microwave absorbing materials are highly desired. Suitable microwave absorbing materials require functionalization at nanoscale to acquire on-demand tunability in order to match them with applications such as broadband or frequency specific absorbing components. Therefore, the **overall objective** of the study is the development, optimization and evaluation of anisotropic hierarchically structured composite as an efficient microwave absorber. To achieve the goal, the hybrid graphene-alumina nanofibers were incorporated into the matrix of α-Al$_2$O$_3$ to prepare an efficient multilayered architecture for providing a range of the required properties including but not limited to enhanced X-band absorption, high strength, and anisotropic thermal and electrical properties.

The **specific goals** of the work are as following:

I.   Design and deposition of graphene layers onto γ-Al$_2$O$_3$ nanofibrous substrate and thorough characterization of their structural features, and transport properties.

II.   Fabrication of homogeneous composite structures of GAIN/α-Al$_2$O$_3$ with various contents of GAIN by spark plasma sintering to study the influence of GAIN fibers on the microwave absorption performance of the host matrix.

III. Comprehensive study of phase and microstructural evolution, electronic and dielectric properties, thermal transport, thermoelectric effect, and microwave absorption performance of the developed homogeneous composite structures as a function of added GAIN fillers.

IV.   Design a protocol for fabrication of sandwiched and multilayer structures of GAIN/α-Al$_2$O$_3$ and optimization of their sintering routes.

V.   Design and simulation of the microwave absorption performance of functionally graded multilayer structures to enhance power transfer and absorption performance of the bulk.

VI.   Manufacturing and characterization of the functionally graded multilayer structures in terms of graphene structure, microstructural evolution, mechanical properties, and microwave absorption performance at X-band.

VII.   Design functional multilayer structure with a full X-band absorption.

2 Materials and methods

2.1 Precursors

2.1.1 Alumina nanopowder

Commercially available ultra-fine α-alumina (purity >99.99 %, TM-DAR, Taimei Chemicals Co, Ltd, Japan) with an average particle size of 100 nm was used as the matrix material in homogeneous composites and multilayer structures. The manufacturer specifies the density of 3.96 g·cm^3.

2.1.2 Alumina nanofibers

Alumina nanofibers network, produced by a recently developed process of controlled liquid phase oxidation from aluminum melt (Kutuzov, 2013) was employed as the substrate for CVD graphene deposition. The network represents a highly aligned mesoporous structure with a single nanofiber diameter ranging from 5 up to 10 nm and aspect ratio of up to 10^7 (Aghayan, Hussainova, Gasik, Kutuzov, & Friman, 2013). Optical image of a typical block of the fibers before CVD processing together with SEM and TEM images are provided in **Figure 2.1**.
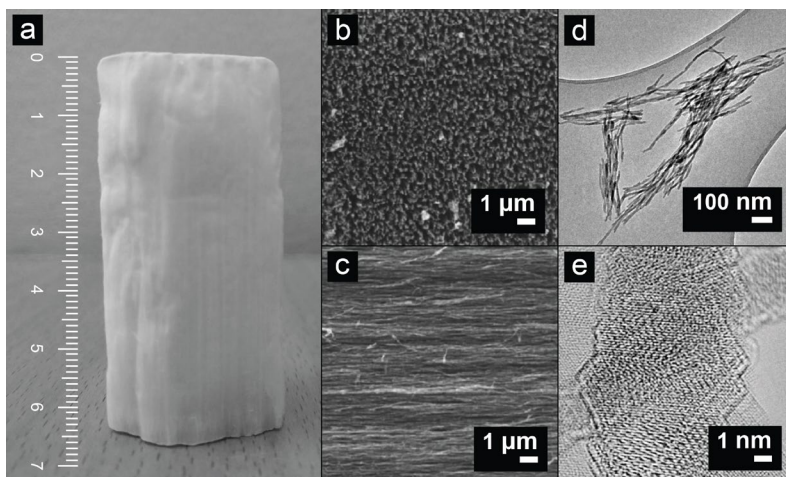

Figure 2.1 (a) Optical image of a block of alumina nanofibers; (b) SEM image of the cross section of the block; (c) SEM image of the block portraying the self-alignment of the nanofibers; (d-e) HR-TEM images of the fibers.

2.1.3 Graphene augmented alumina nanofibers

Graphene augmented inorganic nanofibers (GAIN) were produced using a single step catalyst-free hot-wall CVD technique in a tube furnace kept at 1000 °C for 30 min total time. The baseline process is detailed in (Ivanov et al., 2015). A modification on the baseline process in terms of flow rates and dwell time was made in order to minimize graphene layer count while maintaining homogeneous and conformal deposition. Aligned γ-Al$_2$O$_3$ bundles of 4 cm long and 0.7 × 0.7 cm^2 in cross section were cut and used as substrate for graphene deposition. Dried weight of the γ-Al$_2$O$_3$ nanofibrous bundle prior to the CVD deposition was ~0.15 g. Firstly, the nanofibers were loaded into the tube furnace and dried for 10 minutes in air (open furnace) at 1000 °C to remove organic residues and OH adatoms. Second, the furnace was sealed on both sides and the fibers

were treated in 1000 sccm of N_2 for 10 minutes to further purify the substrate from surface adsorbed impurities. Third, N_2 was closed, and deposition started using 25 sccm H_2 and 50 sccm CH_4. In this approach, H_2 acts as etching gas to remove loosely bonded and out of plane carbon atoms promoting more sp^2 hybridization. The process was stopped after 10 minutes of deposition and coated fibers were quenched to room temperature in 4000 sccm N_2 stream to prevent reduction of carbon at elevated temperature. Optical images and schematic of GAIN fibers are provided in **Figure 2.2**.
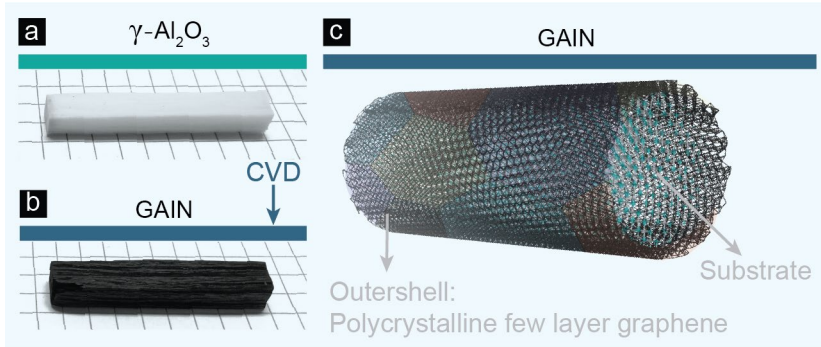

***Figure 2.2** (a) Optical image of a γ-Al$_2$O$_3$ nanofibers bundle before CVD; (b) optical image of the GAIN obtained from CVD process; (c) schematic representation of polycrystalline graphene augmenting alumina nanofibers (constructed using VESTA by jp-minerals and Nanotube Modeler by JCrystal Soft).*

2.2 Processing routes

Processing of the composites consisted of powder processing for preparation of homogeneous composites and solution-based filtration technique for implementation of the layered structures. A schematic of the full process from CVD coating to SPS is provided in **Figure 2.3**.

2.2.1 Powder processing

To prepare composites of GAIN and α-Al$_2$O$_3$, the fibers were ground in a mortar, dispersed in ethanol, then sonicated using a sonication rod (Hielscher UP400S) for 20 min with 20 W and procedure of "2 s on – 1 s off" as detailed in **Paper I**. The suspension was dried at 70 °C for 12 h in air; and GAIN fibers of 300–600 nm in length were collected. To prepare the power compositions, the as-prepared GAIN and α-Al$_2$O$_3$ nanopowder were weighed corresponding to 1, 3, 5, 15, and 25 wt.% of GAIN, dispersed in ethanol and further sonicated for 20 min with 20 W and procedure of "2 s on – 1 s off". The powder compositions were dried at 70 °C for 12 h in a muffle furnace in air. In order to prepare the multilayer structures, the as-prepared short GAIN fibers were weighed and mixed with corresponding amounts of α-Al$_2$O$_3$, dispersed in chloroform ($CHCl_3$) and sonicated for 20 min with 20 W and procedure of "2 s on – 1 s off" as detailed in **Paper I**. The suspensions were directly used for fabrication of multilayers.

2.2.2 Colloidal suspension

The colloidal suspension obtained from the sonication of GAIN and α-Al$_2$O$_3$ in chloroform was used in layer-by-layer deposition directly inside SPS die (**Figure 2.3**). Prior to that, two green pellets of α-Al$_2$O$_3$ nano-powder corresponding to a sintered thickness of

2–10 mm (varied for various studies) were produced without plasticizer under 5 MPa of pressure to insert as the top and bottom layers of the structures. One of the green pellets was placed inside the SPS die, the die was placed on a glass flask coupled with a vacuum pump. The colloidal suspension of GAIN and α-Al_2O_3 was dropped slowly using a pipette and filtered through the die. The process could be repeated as many times as needed to prepare designed architecture. After the filtration, another green pellet was inserted in the die (as the top layer) and the entire structure was further rinsed by filtration of chloroform. Then, the die was removed and placed in a muffle furnace for drying at 70 °C for 12 h in air.
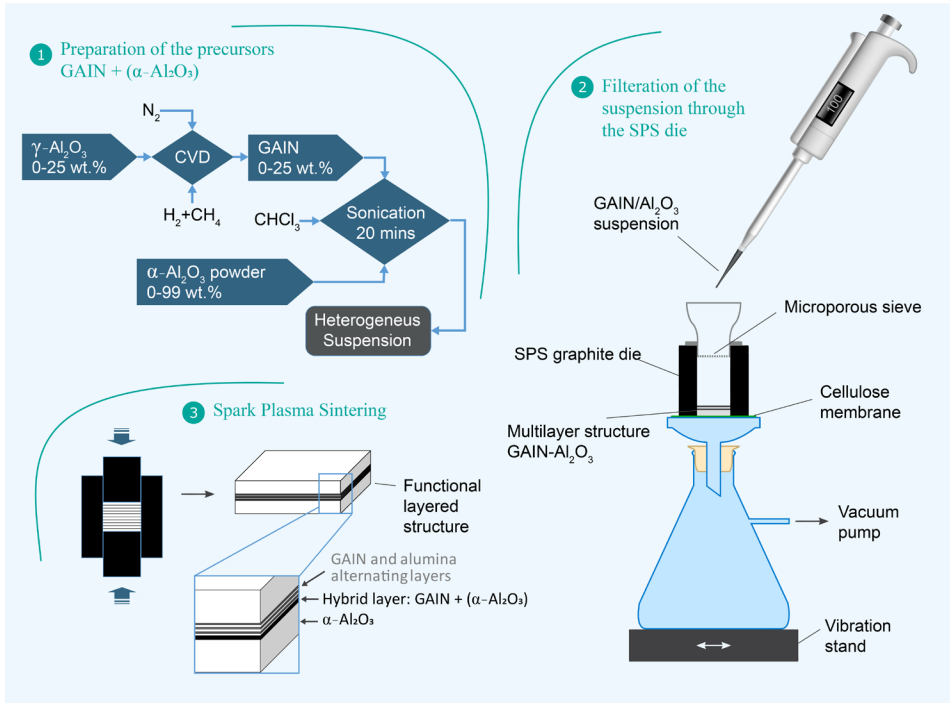

Figure 2.3 *Processing steps for fabrication of composite structures.*

2.2.3 Consolidation approaches

The powder compositions were weighed for desired thickness of the final specimen (according to theoretical density calculations using the rule of mixtures), loaded to SPS dies of 20 and 30 mm in diameters and consolidated using spark plasma sintering (FCT System GmbH SPS furnace, Germany). Two separate approaches employed for consolidation of the structures are as follows: I) 1150 °C, 75 MPa uniaxial pressure in a vacuum (cycle designation – LT); II) 1450 °C, 50 MPa uniaxial pressure in 1 bar N_2 (cycle designation – HT). The SPS cycles for temperature and force as a function of process time for both approaches are illustrated in **Figure 2.4**. To prepare the sintered bulks for physical characterizations, approximately 200 µm was grinded off from both sides of the samples to eliminate impurities due to diffusion of carbon into the cylinder top and bottom faces. Lastly, the procedure was complete by polishing down to 0.5 µm using diamond discs and to 0.05 µm using diamond slurry.
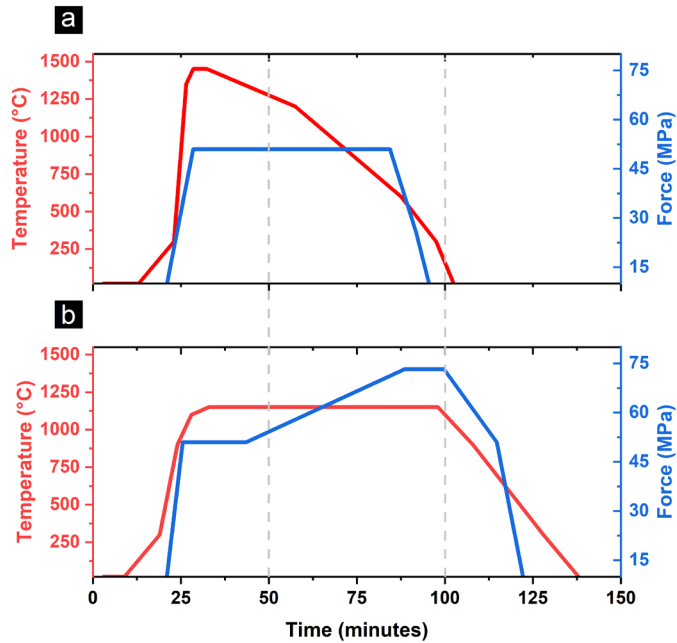
Figure 2.4 *Spark plasma sintering cycle for consolidation of structures using (a) high temperature with dwell temperature of 1450 °C; and (b) low temperature approach with dwell temperature of 1150 °C.*

2.3 Characterization methods

In this section, characterization methodologies and analysis methods are described.

2.3.1 Microstructural analysis

For microstructural characterization of the GAIN fillers and composite structures, a field emission scanning electron microscope (FEG-SEM Zeiss ULTRA-55, Germany) equipped with EDS (energy dispersive X-ray spectrometer, BRUKER, Esprit 1.82 system, USA) with voltage of up to 20 kV and magnifications up to 50 kX was used. Some of the microstructural analysis in this study were carried out using a second electron microscope (HR-SEM Zeiss Merlin, Germany) equipped with an energy dispersive X-ray spectrometer (Bruker EDX-XFlash6/30 detector) with operating voltage of 5 kV. Grain size analysis was carried out by image analysis of SEM images considering at least 500 readings using Image Pro Plus 7.0 package by Media Cybernetics. All the SEM images for this analysis were recorded at the same magnification (5000x) and at least three micrographs from each sample were analyzed to get reliable statistics. Resulting size of the GAIN fibers after solution-based mixing process was determined by laser scattering method using Mastersizer 3000, Malvern Panalytical, equipped with a λ = 632.8 nm He–Ne laser. The morphology of the hybrid GAIN was examined by JEOL JEM-2800 high resolution transmission electron microscope (HRTEM, JEOL Ltd., Tokyo, Japan).

2.3.2 Phase characterization

Carbon content of the CVD graphene augmented alumina nanofibers was determined using a LECO CS 200 Carbon-Sulphur analyzer. Three measurements were made, and the arithmetic mean was used to calculate the corresponding carbon content of the composites.

Raman spectroscopy was carried out using Horiba LabRAM 800 high-resolution spectrometer equipped with a 532 nm laser excitation wavelength at room temperature (RT) and a 50X objective lens (NA = 0.95). The incident laser power was 2–7 mW. Raman spectral resolution of the system was 1.5 cm^{-1}. Raman mapping of the multilayers was carried out by confocal Raman microscopy (Witec ALPHA 300RA) employing a 532 nm Nd:YAG laser at RT equipped with a 20× objective lens. The grating of 600 g/mm BLZ = 500 nm and incident laser power of 0.17 mW was used. The optical diffraction resolution of the confocal microscope was limited to about 200 nm laterally. Raman spectral resolution of the system was 0.02 cm^{-1} under the best measurement conditions. A piezoelectric scanning table allowed three-dimensional displacements in steps of 3 nm, giving a very high spatial resolution for the confocal Raman spectroscopy.

Crystalline phases were characterized by Rigaku, Japan, X-ray diffraction equipment (XRD) with a copper sealed 2 kW tube target producing Cu Kα and Kβ emission lines from a generator operating at 40 kV. The collected data was acquired and analyzed using Rigaku SmartLab SE software with a D/teX Ultra 250 1D detector.

2.3.3 Mechanical properties

The densities (ρ) of the sintered structures were determined using the Archimedes method, ME204 Mettler Toledo, United States, with distilled water as the immersive media. The rule of mixtures using the manufacturers' density specification for alumina powder (3.96 g·cm^{-3}), alumina fibers (3.65 g·cm^{-3}), and published density value for graphene (2.2 g·cm^{-3}) was used to calculate the relative densities.

Vickers microhardness tests were carried out under 4.9 N load (HV0.5) using BUEHLER MICROMET 2001 equipped with a square-based orthogonal pyramidal diamond indenter. The HV values were converted to SI unit using **Equation 3** according to Annex F, ISO 14577–1:2015. In this equation, HV is the Vicker's hardness, H_{IT} is the indentation hardness, A_P is the projected area of the indenter, A_S is the contact surface area, and g is the gravitational acceleration equal to 9.81 m·s^2.

$$HV = \frac{H_{IT} \times A_P}{g \times A_s} = 0.0945 \; H_{IT} \; GPa \qquad (3)$$

Nanoindentation was carried out using NanoTest Vantage (MicroMaterials ltd, UK) nanoindenter equipped with a diamond Berkovich tip. Prior to the test, calibration was performed on the Berkovich diamond indenter with hardness of 1140 GPa and Poisson's ratio of 0.07 using a standard fused silica specimen. Loading was performed at 10 mN/s with dwell time of 5 s and unloading rate of 10 mN/s. The drift rate was preset to <0.05 nm/s before the beginning of each indentation test.

2.3.4 Electrical transport measurement

To measure in-plane resistivity of the multilayer structures, a two-probe setup coupled with a tube furnace operating from room temperature to 400 K was used. To prepare the contact areas, first, using a Cressington 308R sputtering system, 80 nm of Pt was deposited on the opposite lateral faces of the rectangular bar shaped specimens, then 500 μm Ag conductive paste was applied, and lastly, samples were thermal treated at 100 °C for 12 h.

The same procedure was employed to prepare contact areas of homogeneous composites and GAIN fibers for a five terminal method to be measured using a physical property measurement system (PPMS; Quantum design; equipped with 9 T magnetic field) with Hall bar configuration from 4 K to 400 K. In this method, resistance and Hall resistance are simultaneously measured (**Figure 2.5**).
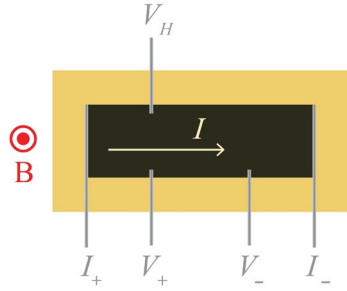

Figure 2.5 *Schematic of a sample mounted in five terminal configurations for simultaneous measurement of resistance and Hall resistance using PPMS.*

2.3.5 Thermal transport measurement

Simultaneous measurement of thermal conductivity, diffusivity, and specific heat capacity was done on homogeneous composites and multilayers employing transient plane source method using HotDisk 2500S equipment. Two identical specimens were placed in between two XPS insulators; and 5501 Kapton sensor with 6.4 mm diameter was placed between the two specimens for a double-sided isotropic measurement (**Figure 2.6**). For this measurement cylindrical samples with 30 mm diameter and 20 mm thickness were used. The power of 300 mW and 40 s probing time was used for every reading. In total, 10 readings for each sample were recorded and the arithmetic mean average was used for analysis.

For in-plane and cross-plane thermal transport measurement, laser-flash method (Thermaflash 2200, Holometrix, Netzsch GmbH, Selb, Germany) was employed. The in-plane thermal diffusivity ($\alpha_{||}$) (perpendicular to the SPS pressure axis) was obtained for discs with 20 mm diameter and 600 µm thickness. The through-plane thermal diffusivity ($\alpha_{\perp}$) (Transversal to the SPS pressure axis) was obtained for square samples (8.8×8.8 mm^2) from 298 K to 1073 K. Prior to the procedure, thin matte graphite layers were sprayed onto the surfaces of the samples exposed to the laser excitation; to avoid energy loss due to surface scattering and maximize absorption.
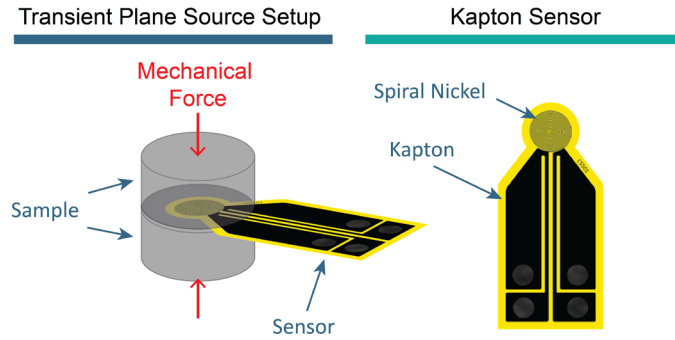
Figure 2.6 Measurement setup for double-sided transient plane source (TPS) thermal transport measurement.

2.3.6 Thermoelectric characterization

For low temperature thermal transport and thermoelectric study, a physical property measurement system (PPMS, Quantum Design GmbH, USA); equipped with 9 T magnetic field) was used. A set of specimens were cut using a precision diamond wheel to bars of $5 \times 10 \times 1$ mm^3. Simultaneously, resistivity (ρ), Seebeck coefficient (S), and thermal conductivity (k) were measured using the thermal transport puck (TTO) of the PPMS on the rectangular bars with the four-probe contact arrangement (**Figure 2.7**). In this procedure, at the steady state, a small amount of heat is applied to one end of the rectangular bars and simultaneously temperature difference and Seebeck voltage are recorded. The Seebeck coefficient is estimated by dividing the Seebeck voltage by the temperature difference. The in-plane thermal conductivity ($k_{||}$) is calculated using the dimensions of the specimen, distance between the probes, and the temperature difference.
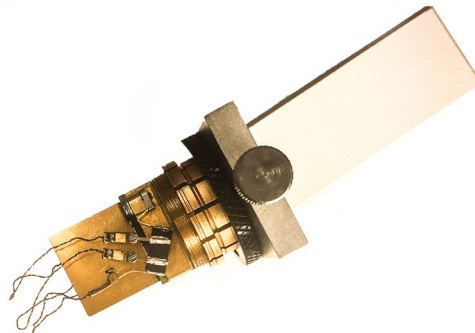
Figure 2.7 Image of a GAIN/α-Al$_2$O$_3$ specimen mounted on the puck of PPMS with four probes placed prior to thermoelectric test.

2.3.7 Dielectric characterization

Complex permittivity and permeability of the composite structures were determined using two-port transmission line method in a rectangular waveguide (WR-90). In accordance with ASTM D5568, the scattering parameters [S11(S22) and S21(S12)] were recorded at X-Band frequencies (8.2–12.4 GHz) using an N5222A PNA Vector Network Analyzer (Keysight Technologies) on the fundamental waveguide mode TE10

(transverse electric) (**Figure 2.8**). The N1500A Materials Measurement Suite (Keysight Technologies) was used to directly convert the obtained S-parameters to complex permittivity and permeability using the Nicholson–Ross–Weir (NRW) method. Prior to the measurement, the specimens were cut using a precision diamond (ATM BRILLANT 220) saw and fine polished to the exact geometrical requirement of the waveguide (22.86 × 10.16 mm^2). In accordance with ASTM D5568, the final transverse geometries of all samples were in the ±100 μm range.
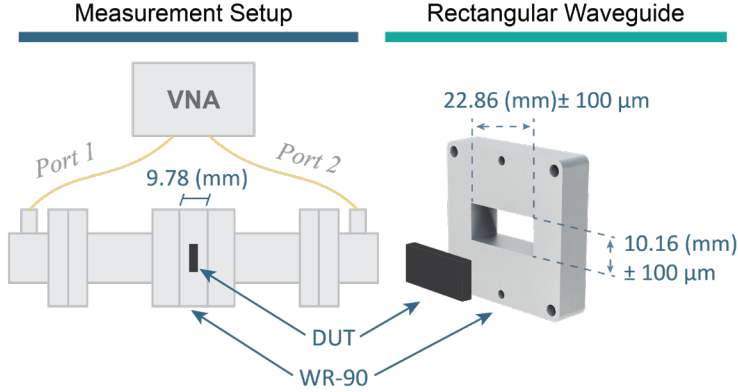

Figure 2.8 Measurement setup for microwave S-parameters and dielectric properties using two-port network analyzer. A one-port version of the setup backed with short was used for microwave absorption characterization.

2.4 Design and simulation

The obtained dielectric parameters were used in impedance matching technique in order to design functionally graded multilayer structures. Considering the samples are backed with a perfect electric conductor (PEC) the input impedance of a homogeneous bulk can be calculated using **Equation 4**. In this equation, where Z_0 is the characteristic impedance of free space (377 Ω), Z_{in} is the input impedance of the absorber, f is the measured frequency, d is the thickness of the material, and c is the speed of light. **Equation 5** is used to calculate the input impedance of a multilayer with *i* number of layers in which η_i is the characteristic impedance of each layer which is calculated using $\eta_i = \eta_0\sqrt{\mu_{ri}/\varepsilon_{ri}}$ and propagation constant γ_i can be calculated using $\gamma_i = j(2\pi f/c)\sqrt{\mu_{ri}\varepsilon_{ri}}$. Using **Equation 6**, the reflection loss (RL) and correspondingly absorption efficiency can be calculated.

$$Z_{in} = Z_0\sqrt{\frac{\mu_r}{\varepsilon_r}}\,tanh\left[j\left(\frac{2\pi fd}{c}\sqrt{\mu_r\varepsilon_r}\right)\right] \qquad (4)$$

$$Z_{in} = \eta_i\frac{[Z_{i-1}+\eta_i\tanh{(\gamma_i d_i)}]}{[\eta_i+Z_{i-1}\tanh{(\gamma_i d_i)}]} \qquad (5)$$

$$RL(dB) = -20log\left|\frac{Z_{in}-Z_0}{Z_{in}+Z_0}\right| \qquad (6)$$

33

To optimize layer thicknesses and compositions, an algorithm was developed in Matlab based on Monte Carlo simulation. Monte Carlo simulation relies on random sampling in order to find accidental solutions to otherwise deterministic equations of impedance and surface reflection loss. In this work, utilizing Monte Carlo, the defined boundary conditions stipulated total thickness limitations, and RL <-10 dB, while for each iteration 3×10^7 random layer thickness values were solved. Some of the Monte Carlo findings were chosen for implementation, others are reported as potential multilayer configurations and future work.

Ansys HFSS was used to simulate the multilayer structures considering a partially filled rectangular waveguide with the TE10 mode incident. The simulation results were used to compare power transfer rates variations between simulation and experiment.

3 Results and discussions

This section summarizes the cumulative data on characterization of GAIN fibers, homogeneous GAIN/α-Al$_2$O$_3$ composites, and functional multilayers.

3.1 Characterization of the precursors

3.1.1 GAIN fibers

After CVD graphene deposition on γ-Al$_2$O$_3$ nanofibers, phase identification using X-ray diffraction and Raman spectroscopy; and morphological features using TEM were studied to characterize the resulting GAIN fibers (**Paper I, III, IV**). Additionally, using gas chromatography, carbon content was measured at 12 wt.% estimated from mean value of five readings. XRD has shown no phase transformation (γ→α) after the CVD process performed at 1000 °C and for post thermal treatment of GAIN at 1150 °C in air. However, a partial γ→α transformation in the case of heat treatment at 1450 °C in N$_2$ and a full transformation after heat treatment at 1450 °C in air is detected (**Figure 3.1**). The heat treatment conditions were chosen to replicate the sintering temperature of the composites in order to elucidate the temperature effect on the phase transformation during consolidation.
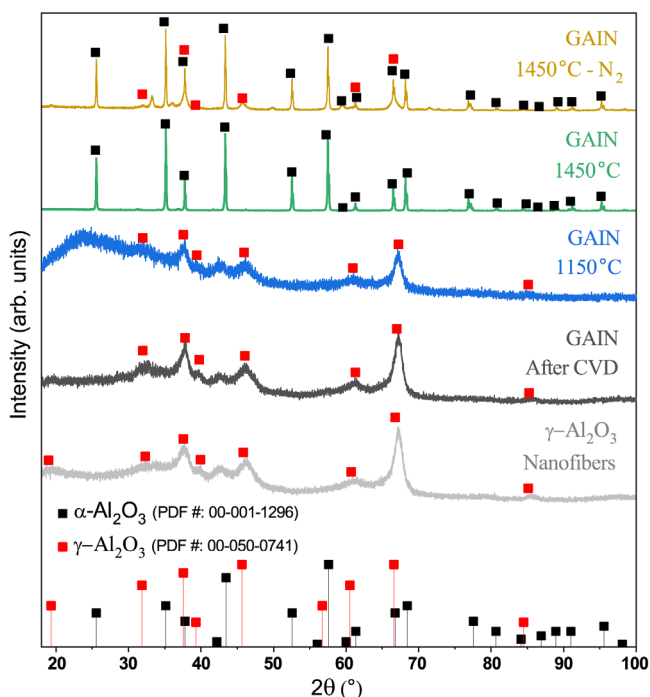
Figure 3.1 *X-Ray diffraction spectra of pristine γ-Al$_2$O$_3$ nanofibers, fibers after CVD, and a series of thermal treatments on GAIN.*

A schematic representation of GAIN, optical and SEM images of alumina nanofibers before and after CVD, and TEM images of GAIN are shown in **Figure 3.2**a–h. Raman peak positions and FWHMs obtained from Lorentzian fitting are listed in **Table 1**. In various TEM micrographs, a discontinuous nanocrystalline few-layer graphene with 1–5 layers is

evident (**Figure 3.2**c–e). The discontinuity is shown to have stemmed from the substrate topological defects giving rise to various nucleation centers for sp^2 carbon growth. The single crystalline graphene sheets originated from the point defects grow until eventually merge to one another. As a result, grain boundaries (GB) form between them that give rise to various properties change such as introduction of band gap. Unlike bulk materials, displacement is allowed for carbon atoms in 2D graphene sheets which manifests as buckled out-of-plane grow in various angles. As is evident from **Figure 3.2**f–g, the high intensity of the defect modulated D peak at 1342 cm^{-1} as compared to G peak at 1585 cm^{-1} (I_D/I_G ratio ~1.81) indicates presence of small sp^2 domains, consistent with HRTEM observations (Stankovich et al., 2007). The $I_D/I_{D'}$ ratio of ~5.5 corresponds to a combination of hopping and vacancy-like defects (Venezuela, Lazzeri, & Mauri, 2011).
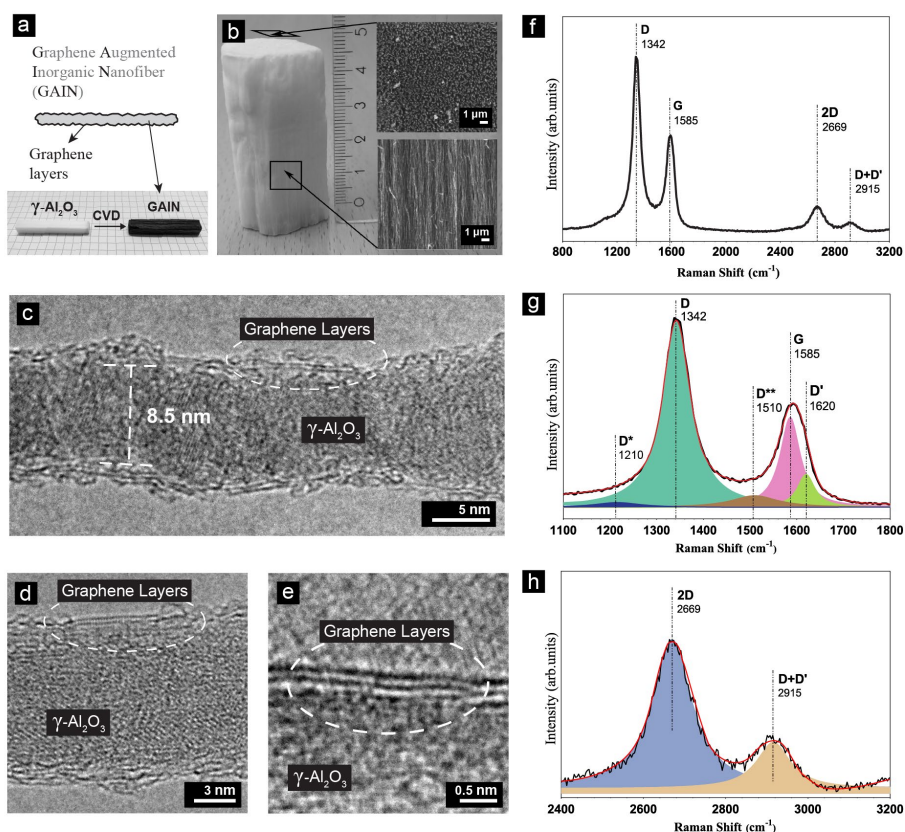
***Figure 3.2** (a) Schematic of GAIN with γ-Al₂O₃ core and graphene coating together with optical images of before and after the CVD process; (b) optical image and SEM images of self-aligned γ-Al₂O₃ nanofibers; (c–e) HRTEM images of a GAIN fiber with 2–3 layers of graphene coating; (f) Raman spectrum of GAIN; (g) deconvolution of the peaks providing details on the Raman shift ranging from 1100 to 1800 cm⁻¹; and (h) 2400 to 3200 cm⁻¹. The figure is adopted from **Paper III** with permission (Shamshirgar et al., 2021).*

The 2D Raman mode in graphene is caused by double resonance scattering of TO phonons at the k-point of the zone edge. In GAIN fibers, the 2D peak at 2669 cm^{-1} is broadened (in comparison with a typical Raman for single layer graphene) with a FWHM of ~116 and a I_{2D}/I_G ratio of 0.32. In few-layer graphene, the I_{2D}/I_G ratio is peak is ~4 (the wider the peak gets at 2D region, the more layers of graphene are expected (Andrea C. Ferrari, 2007)). For GAIN fibers, the low I_{2D}/I_G ratio, position and FWHM of the 2D peak, and existence of a notable D peak can be attributed to the presence of turbostratic carbon (Andrea C. Ferrari, 2007).

The D+D' peak at ~2915 cm^{-1} is the second order of the intra-valley D' peak at ~1620 cm^{-1} and its presence can be in response to hydrogen functionalization (employed during CVD procedure) and sp^3 hybridization (Andrea C. Ferrari & Basko, 2013). The 2D band is 21 cm^{-1} redshifted as compared to a typical single layer graphene. This redshift presumably has stemmed from the local strain caused by the lattice mismatch between γ-Al$_2$O$_3$ substrate and graphene; resulting in a decrease in phonon energies (Andrea C. Ferrari & Basko, 2013). Even though, the same physical mechanism is expected to redshift the G peak, the ~5 cm^{-1} blueshift of this peak is likely to have originated from the doping effect of the substrate (Stamatin, Hussainova, Ivanov, & Colavita, 2016). As a point of comparison, the G peak for a typical single layer graphene is at ~1580 cm^{-1} measured with similar wavelength laser (Saito, Hofmann, Dresselhaus, Jorio, & Dresselhaus, 2011). In fact, both n- and p-doping shift Fermi level away from the Dirac point and decrease the recombination probability of the charge carriers. This, results in non-adiabatic perturbation of the phonons, removing the Kohn anomaly with the outcome of an increase in phonon energy of the G peak and the subsequent blueshift (Pisana et al., 2007a) (Das et al., 2008). The defect-driven D* and D** peaks at 1210 cm^{-1} and 1510 cm^{-1}, respectively, can be attributed to sp^2-bonded configurations of transpolyacetylene segments at grain boundaries and surfaces of CVD carbon postulated by (A C Ferrari & Robertson, 2001).

Table 1 *Peak position, FWHM, intensity ratio comparison for GAIN.*

D		G		D'		2D		D+D'	
Peak Position	FWHM	Peak Position	FWHM	Peak Position	FWHM	Peak Position	FWHM	Peak Position	FWHM
1342	73	1585	52	1620	45	2669	116	2915	100

3.1.2 Powder compositions

As was described in **Section 2.2** GAIN/α-Al$_2$O$_3$ powder mixtures in the ratios of 1, 3, 5, 15, and 25 wt.% GAIN were prepared using sequences of grinding and sonication. The SEM micrographs of the resulting powder mixtures are shown in **Figure *3.4***a-f. Length of the GAIN fibers after processing are reduced to 300 ± 100 nm, which corresponds to 40:1 to 60:1 aspect ratios. Although in general, the distribution of the fibers is rather homogeneous, the fibers are partially overlapping, forming moderate level agglomeration. This is particularly valid for high concentration of GAIN visible in **Figure *3.4***e,f for 15 and 25 wt.% of GAIN, respectively.

3.2 GAIN/α-Al$_2$O$_3$ homogeneous composites

The 1–25 wt.% GAIN/α-Al$_2$O$_3$ composites were sintered using SPS detailed in **Section 2.2.3**. The dwell temperature was considered 1150 °C in order to prevent γ→α-Al$_2$O$_3$ phase transformation. This phase and the connotation of its formation on sintering procedure and microstructural integrity of the composites is explained in the next section. All samples were sintered in a 20 mm and 30 mm graphite die with final sintered thickness of 5–10 mm. A summary of the densities, compositions, and carbon contents of the samples is provided in **Table 2**.

Table 2 *Graphene content and relative density of the produced samples.*

Sample Name	α-Al$_2$O$_3$ [wt.%]	GAIN [wt.%]	GAIN [vol.%]	Graphene * [vol.%]	Relative Density
α-Al$_2$O$_3$	100	0	0	0	99.99
G1	99	1	1.13	0.21	99.32
G3	97	3	3.39	0.63	99.45
G5	95	5	5.65	1.04	98.98
G15	85	15	16.74	3.10	93.80
G25	75	25	27.56	5.10	89.51

* Calculated based on the measured 12 wt.% graphene content of GAIN.

3.2.1 Microstructural features

A comparison between the microstructure of sintered as-received α-Al$_2$O$_3$ and a sample with 1 wt.% GAIN fillers is provided in **Figure 3.3**. It is evident that grain refinement is achieved by addition of 1 wt.% GAIN where the grains of 200–400 nm are in contrast to 1–5 μm grains observed for as-received alumina. Presence of both inter and intra granular porosity is visible in **Figure 3.3**a–b (marked with orange arrows) for bulk alumina sintered at 1150 °C. Addition of GAIN fillers assists the sintering by introducing local joule heating provided by the conductive fillers, resulting in diminished porosity and full densification (**Figure 3.3**c–d). To clarify, the distribution of the fillers throughout the grain boundaries of the matrix ceramic, contributes to preservation of their migration (impeding GB diffusion) during sintering, resulting in grain refinement. This effect was also observed for graphene nanosheet/Al$_2$O$_3$ (Fan et al., 2010). In **Figure 3.3**d, GAIN nanofillers are mainly located at the grain boundaries or junctions of Al$_2$O$_3$ grains. Therefore, the mechanism responsible for a higher densification can be defined as the pinning effect of the fillers on the Al$_2$O$_3$ grains. The SEM images in **Figure 3.4**g–l show the microstructural features of the GAIN/α-Al$_2$O$_3$ homogeneous composites and reference sintered polycrystalline alumina. An increase in GAIN concentration further impedes grain growth. The grains of ~100 nm in G25 are comparable to the particle size of the precursor powder (**Figure 3.4**l). Evidently, the porosity also increases for GAIN contents higher than 5 wt.% which is consistent with density measurements. This grain size reduction is postulated to be in connection with the pinning effect of the GAIN fibers and reduced mass transport in the presence of high carbon content, both result in hindered densification.
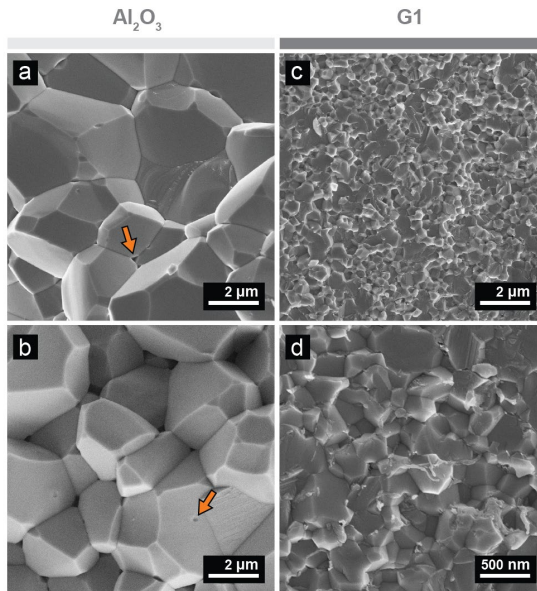
Figure 3.3 *SEM micrographs of (a, b) alumina sintered bulk; and (c, d) with 1 wt.% GAIN content sintered at 1150 °C under 75 MPa uniaxial pressure.*

In addition to the contribution of carbon content to the evolution of the microstructure and grain refinement, the presence of γ-Al$_2$O$_3$ (core of GAIN fibers) in the vicinity of α-Al$_2$O$_3$ (the matrix phase) can lead to the γ→α-Al$_2$O$_3$ transformation process. This phase transformation encompasses several transition alumina phases as detailed in **Section 1.1.1**. In particular, as the θ phase crystallizes into α-Al$_2$O$_3$, a vermicular microstructure with a network of wide pores is anticipated which requires temperatures higher than 1600 °C for high densification (Lamouri et al., 2017; Yalamaç, Trapani, & Akkurt, 2014). The γ → δ → θ → α-Al$_2$O$_3$ phase transformation process is expected to initiate in the temperature interval of 1050–1200 °C. Albeit, under the sintering conditions of 1150 °C, 70 MPa, none of the homogeneous composites demonstrate features of vermicular microstructure, this structure was observed for a sample sintered at 1450 °C discussed in the next Chapter.

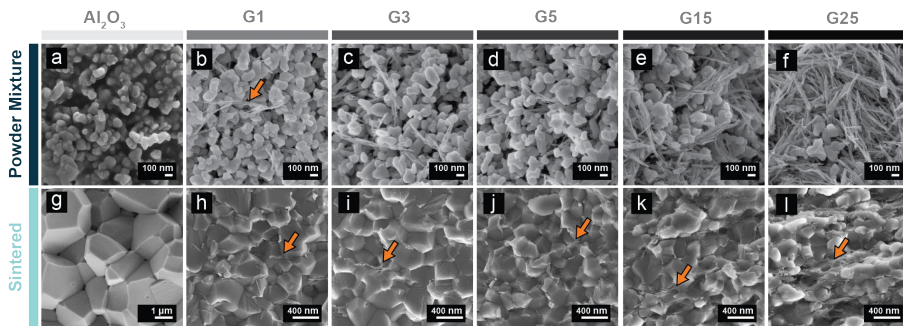***Figure 3.4*** *SEM micrographs of (a–f) alumina powder with various GAIN content; (g–l) sintered bulks consisting of reference alumina and GAIN/α-Al$_2$O$_3$ compositions. The figure is adopted from **Paper IV** (Saffar Shamshirgar et al., 2021).*

3.2.2 Structural characterization

The Raman spectra of the homogenous composites are presented in **Figure 3.5**a. The main features of defected graphene, namely: The G peak at ~1587 cm^{-1} and the 2D peak at ~2688 cm^{-1} are present together with a notable defect driven D peak at ~1347 cm^{-1}. However, some key changes in the intensity ratios, peak positions, and FWHM of the peaks exist. To begin with, the blue shift of the G and 2D peaks and the broadening of FWHM of the G peak in comparison with GAIN can be evidences of both n- and p-doping (Andrea C. Ferrari, 2007) (**Figure 3.5**b–g). Granted that Al interstitials and O vacancies in the matrix α-Al_2O_3 can act as electron accepting point defects (Fan, Jiang, & Kawasaki, 2012), the p-doping of the top graphene layers on GAIN fibers during the sintering can be justified. Additionally, the next layers of graphene can be affected via charge transfer mechanism. In general, blue shift of the G peak in graphene, can be a response to the presence of both n- and p-doping. Doping in graphene results in nonadiabatic removal of the Kohn anomaly at the Γ point and increase phonon energies for the G peak (Pisana et al., 2007b). On the other hand, blue shift of the 2D peak in graphene is often associated with p-doping as a response to the change of the equilibrium lattice parameters (Das et al., 2008).

Strain also has an effect on shifting the G and 2D peak in graphene. In fact, tension is associated with a red shift, while compression is proven to result in blue shift. In this case, a tension force can be in connection with cooling procedure of the CVD process as discussed in Section 3.1.1 originated from the opposite thermal expansion and contraction behavior of carbon and alumina. Whereas compressive stresses can emanate from compaction during SPS, increasing the phonon frequency of various bands and virtually causing an upshift of the spectrum (Tsoukleri et al., 2009).
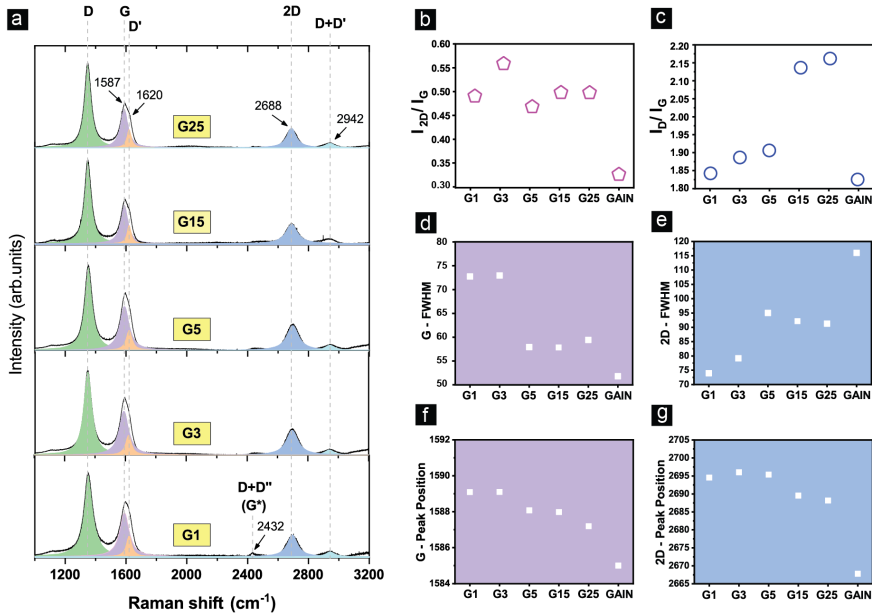
***Figure 3.5** (a) Raman spectra of composites with 1–25 wt.% GAIN content; (b) I_{2D}/I_G ratio; (c) I_D/I_G ratio; (d) G peak FWHM; (e) 2D peak FWHM; (f) G peak positions; (g) 2D peak position for GAIN and composites containing 1–25 wt.% GAIN fillers. The figure is adopted from Paper IV (Saffar Shamshirgar et al., 2021).*

3.2.3 Electrical transport

In **Figure *3.6*a**, electrical resistance of GAIN fibers is plotted versus temperature. For this measurement, a 0.021 cm^3 GAIN fibrous specimen was manually pressed and mounted onto the probe of PPMS in a five terminal configuration explained in **Section 2.3.4**. Since the fibrous specimen had low transverse linear density, resistance values are considered for discussion to avoid inaccuracy in the measurement attributed to the geometries of the specimen. A well pronounced semiconducting behavior is visible in **Figure *3.6*a** with a band gap of 5.6 meV calculated from the slope of the line of Arrhenius plot. The presence of GBs in polycrystalline graphene gives rise to band gap by forming small scale p-n junctions (Tapasztó et al., 2012; Yazyev & Chen, 2014), while mobility is largely suppressed by the presence of various disorders, point defects, and impurities (Koepke et al., 2013). In addition, the power-law dependent semiconducting behavior and absence of a temperature crossover prove no transition in transport mechanism in the measurement temperature. However, the room temperature n-type transport undergoes a transition to a majority p-type transport which occurs in the temperature interval of 250–280 K visible in the **Figure *3.6*a**-inset. In fact, in polycrystalline graphene, the graphene grains are often p-type while the GBs are n-type. However, the contribution of surface adatoms such as physisorbed water or H bonding, and the doping effect of the substrate can modulate carrier mobility and concentration. It can be stated that in GAIN fibers, surface adsorbed water contributes to charge transfer, resulting in a p-type conduction at room temperature. This contribution is reversed below freezing point of water due to a change in water contact angle and a decrease in work function. It was shown that in CVD graphene where Fermi level is shifted away from the Dirac point the hydrophilicity is enhanced, subsequently, a decrease in water contact angle to values ≤60°, p-dopes graphene while at higher values n-doping is expected (Hong et al., 2016). More details can be found in **Paper I**.

By integrating the GAIN fillers into the matrix of α-Al$_2$O$_3$, the electrical conductivity increases as function of GAIN loading and temperature from 4 K to 400 K (**Figure *3.6*b**), while the p-doping is done through interaction with Al interstitials and O vacancies as discussed in **Section 3.1.1**. The percolation threshold was estimated at 1 wt.% of GAIN and conductivity reached ~2000 S·m^{-1} at room temperature for a sample with 25 wt.% GAIN (**Figure *3.6*b–c**). The slope of the ρ vs. T shows a semi-metallic behavior more pronounced at higher filler contents with the bandgap for 1–25 wt.% GAIN/α-Al$_2$O$_3$ composites ranging from 1.0 to 0.6 meV. Similarly, carrier density increases as a function of GAIN (**Figure *3.6*d**), while Hall coefficient decreases at higher filler content attributed to the presence of more n-type fillers.
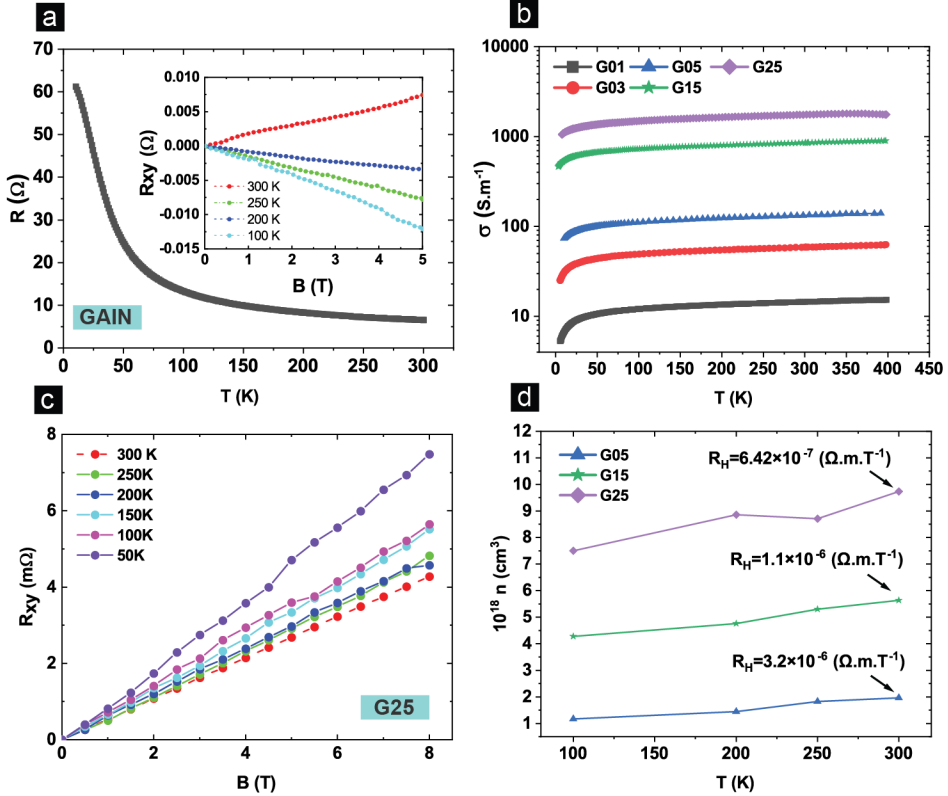
Figure 3.6 *(a) Temperature dependency of DC resistance of GAIN fibers - Inset: Hall resistance as a function of magnetic field for various temperatures; (b) electrical conductivity as a function of temperature of GAIN/α-Al$_2$O$_3$ composites; (c) Hall resistance as a function of magnetic field at various temperatures for a sample with 25 wt.% GAIN; (d) carrier density in composites of GAIN/α-Al$_2$O$_3$.*

3.2.4 Thermal transport and thermoelectric effect

A thorough characterization of thermal and thermoelectric properties of the full composites is provided in **Paper IV**. Laser flash method was used to measure diffusivity (**Figure 3.7**a). To calculate thermal conductivity (k) (**Figure 3.7**b) using the following equation k = α·ρ·C$_p$, the specific heat capacity values (C$_p$) for γ-Al$_2$O$_3$, α-Al$_2$O$_3$, and carbon were considered from NIST-JANAF database (Chase Jr., 1998) (**Figure 3.7**b-inset). Both in-plane and through-plane diffusivity and conductivity decrease by increasing GAIN fillers. However, for GAIN contents higher than 5 wt.%, in-plane values decay at a lower rate, indicating anisotropic alignment of the fibers and more efficient filler connections in the direction perpendicular to the pressure axis of SPS. This deviation can be seen in the in-plane versus through-plane values as a function of GAIN content in the **Figure 3.7**a-inset. On the same note, the sudden drop in the k values for composites with filler contents lower than 5 wt.% can be attributed to large contribution of thermal contact and boundary resistance enforced by the presence of the GAIN fibers at the GBs. In addition to that, the p-doping of the graphene by the matrix alumina can further limit the thermal transport by promoting phonon-defect scattering. Even though microstructural features such as reduction in grain size by increasing filler contents can

attribute to decreasing k, in the GAIN/α-Al₂O₃ composites, much smaller phonon mean free path (few nanometers) as compared to grain sizes (few hundred nanometers) elucidate the defect and impurity scatterings as higher contributing factors to the mean free path reduction than the contribution of the boundary scattering. For a discussion regarding phonon mean free path, please refer to **Paper IV**.
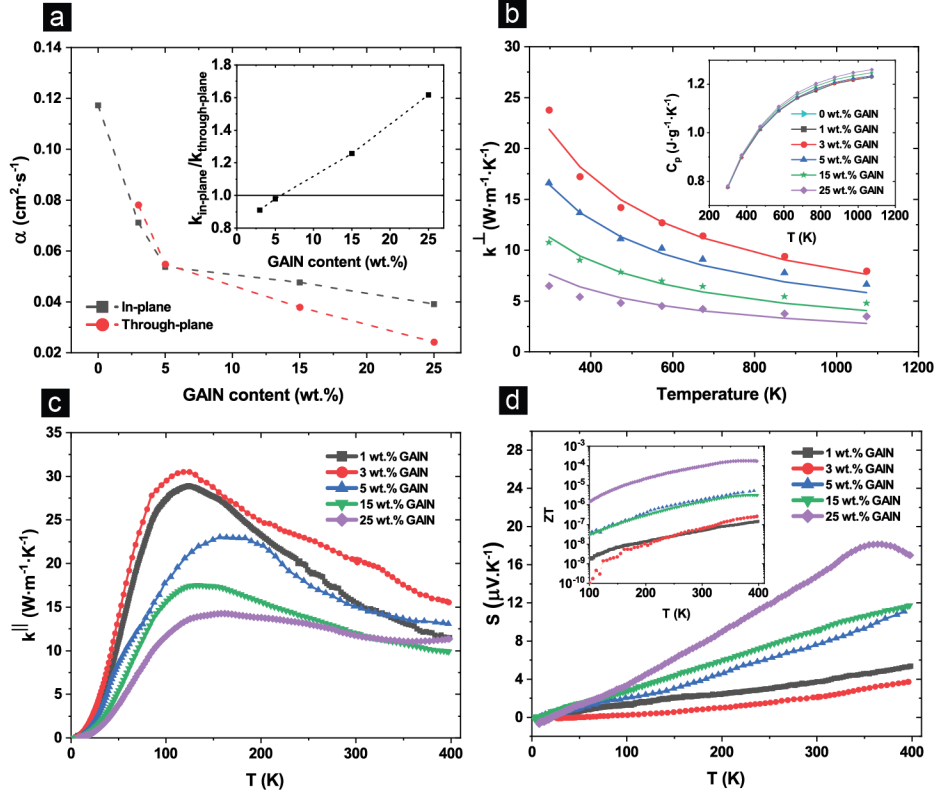

Figure 3.7 (a) Diffusivity as a function of GAIN filler content for in-plane and through-plane directions – inset: in-plane vs. through-plane thermal conductivity; (b) through-plane thermal conductivity as a function of temperature in GAIN/α-Al₂O₃ composites – inset: specific heat capacity vs. temperature; (c) in-plane low temperature thermal conductivity measured with PPMS; (d) Seebeck coefficient vs. temperature in composites of GAIN/α-Al₂O₃ – inset: thermoelectric Figure of Merit vs. temperature.

By simulating the temperature dependency of GAIN/α-Al₂O₃ composites from 293 K to 1100 K, it is evident that the values follow $k\sim T^{-B}$ relation with the exponent "B" varying from 0.82 to 0.78 for G3 to G25, respectively. In **Figure 3.7**b, the straight lines follow the simulated data and scattered points correspond to the measured data. Furthermore, by plotting the k values versus reciprocal of temperature, the presence of extra phonon scattering mechanisms other than anharmonic Umklapp phonon scattering was confirmed. Low temperature in-plane thermal conductivity using the thermal transport puck of PPMS, from 4 K to 400 K is shown in **Figure 3.7**c. A rapid increase of k up to 120 K can be observed attributed to increase in thermally enabled vibration modes. Above 120 K up to 400 K, a decline in k values of all composites can be associated with promotion of more charge carriers and impurity scattering (Amollo, Mola, Kirui, &

43

Nyamori, 2018). Here, the p-doping can be confirmed once more, by the positive values of the Seebeck coefficient (**Figure *3.7***d), while for GAIN/α-Al$_2$O$_3$ composites the Seebeck coefficient increases both with temperature and GAIN content. The Seebeck coefficient is inversely proportional to carrier density and band gap. In contrast, increase in carrier mobility, augments both electrical conductivity and the Seebeck coefficient (Blackburn et al., 2018). It was shown in **Section 3.2.3** that both carrier density and mobility increase by increasing GAIN filler content. Therefore, rather intuitively, the highest Seebeck coefficient was achieved in the sample with 25 wt.% GAIN reaching 18 μ·V·K^{-1} at 350 K.

Using **Equation 1** and the measured values of electrical conductivity (σ), Seebeck coefficient (S), and thermal conductivity (k), the thermoelectric Figure of Merit (ZT) is calculated and plotted versus temperature in **Figure *3.7***d-inset. The highest ZT is achieved in G25 with the highest filler content due to a lower thermal conductivity and highest Seebeck coefficient and electrical conductivity.

3.2.5 Dielectric properties and microwave absorption

Complex permittivity and permeability were obtained from NRW technique (explained in **Section 2.3.7**). The real part permittivity (ε') and dielectric loss tangents (Tan δ$_\varepsilon$) are plotted as a function of GAIN content for sample frequencies of 8.5, 9, 10, 11, and 12 GHz in **Figure *3.8***a. For a detailed analysis of real and imaginary parts permittivity and permeability as a function of frequency at X-band, please refer to **Paper III**.

In general, complex permittivity represents polarization of the charges under an induced electric field. The real part is in connection with energy storage (charge capacity) and the imaginary part (ε'') is the power dissipation ability of the material often in the form heat (Ohmic resistance). The latter is a response to the rearrangement of electric dipole moments in an induced electric field. The dielectric loss tangent is a product of complex permittivity and electrical conductivity and represents the attenuation ability of the material (Thomas, 2018).

The dielectric polarization processes in GAIN/α-Al$_2$O$_3$ can originate from three different characteristics of the structures. First, the heterogeneous composite nature of the structure which consists of conductive graphene augmented fillers and dielectric alumina matrix, promote multiple internal reflection. Second, the presence of various interfaces such as those in core-shell structured GAIN fibers and the boundary between the GAIN and alumina matrix can provide charge accumulation centers. The supporting argument for this assumption is the p-doping effect of the matrix alumina on the graphene and the observed influence of the substrate alumina in GAIN fibers on the optical properties of the graphene, both discussed in **Section 3.1.1**. Third, at higher GAIN filler contents (>5 wt.%), the introduced porosity can provide additional polarization centers (Sebastian, 2017). Specifically, at low GAIN contents, interfacial polarization and its relaxation phenomenon (described by the Maxwell–Wagner–Sillars theory) acting as the primary factors influencing the bulk ε'', can significantly contribute to energy dissipation (Qing, Zhou, Jia, Luo, & Zhu, 2010).

Both permittivity and loss tangent increase with an increase in GAIN content, however, the values of reflection loss (RL) calculated using **Equation 4, 6** for all composites and almost at all frequencies is higher than -3 dB (**Figure *3.8***b). This indicates that more than 50 % of the total power was not transferred into the structure and reflected back to the source. The artefact of the strong surface reflection is the EMI SE values above 25 dB for samples of 3–25 wt.% GAIN (**Figure *3.8***c).
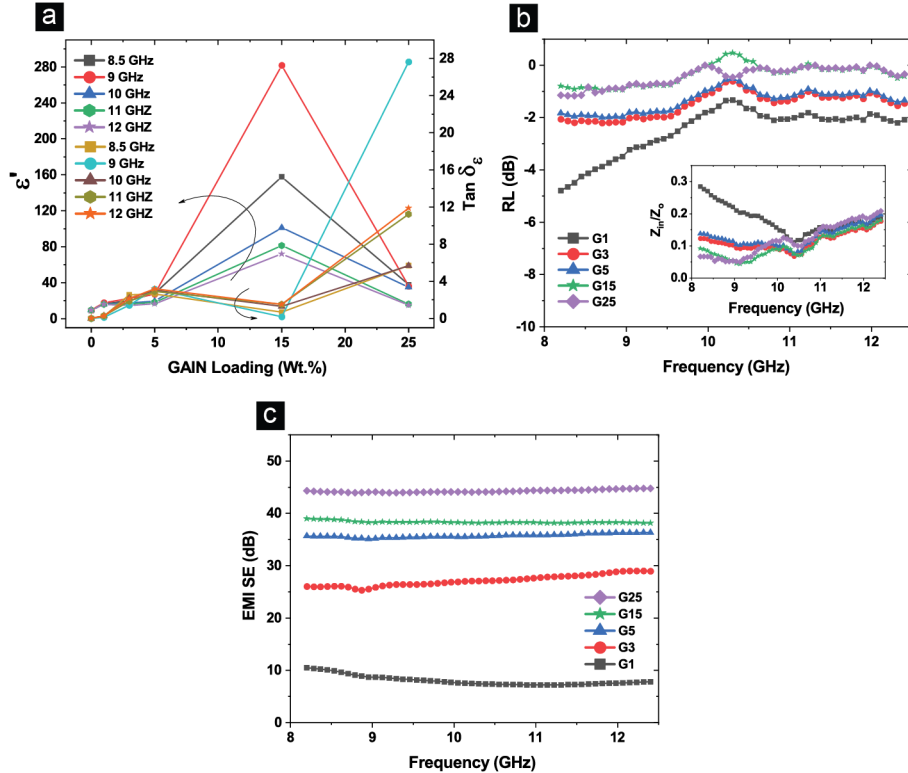
Figure 3.8 (a) real part of permittivity and dielectric loss tangent as a function of GAIN content for sample frequencies 8.5, 9, 10, 11, and 12 GHz in GAIN/α-Al$_2$O$_3$ composites; (b) reflection loss (RL) values of the composites at X-band – inset: normalized input impedance; (c) Total EMI Shielding Effectiveness (EMI-SE) of GAIN/α-Al$_2$O$_3$ composites at X-band.

3.3 Functional multilayer structures of GAIN/α-Al$_2$O$_3$

The multilayer structures were developed for improving the microwave absorption efficiency of the GAIN/α-Al$_2$O$_3$ composites discussed in the previous section. This part consists of two phases: (I) fabrication of sandwich structures (one and two GAIN/α-Al$_2$O$_3$ composite interlayers sandwiched between two layers of α-Al$_2$O$_3$ to establish the fabrication methodology and characterize the properties of the interfaces detailed in **Paper I**; (2) design and fabrication of functionally gradient multilayer structures consisting of several layers of GAIN/α-Al$_2$O$_3$ to improve microwave absorption efficiency detailed in **Paper III**.

3.3.1 Phase and Microstructure

The SEM images in **Figure 3.9**a show the cross section of a sample with one GAIN/α-Al$_2$O$_3$ interlayer and two alumina outerlayers in an AGA configuration; and a sample with two interlayers (AGAGA) both sintered at 1450 °C under 50 MPa pressure (high temperature approach – HT). Evidently, grains of the monolithic alumina layers are significantly larger than those in the interlayer where the presence of GAIN fibers resulted in grain refinement. As a result, sharp interfaces between the layers have formed.
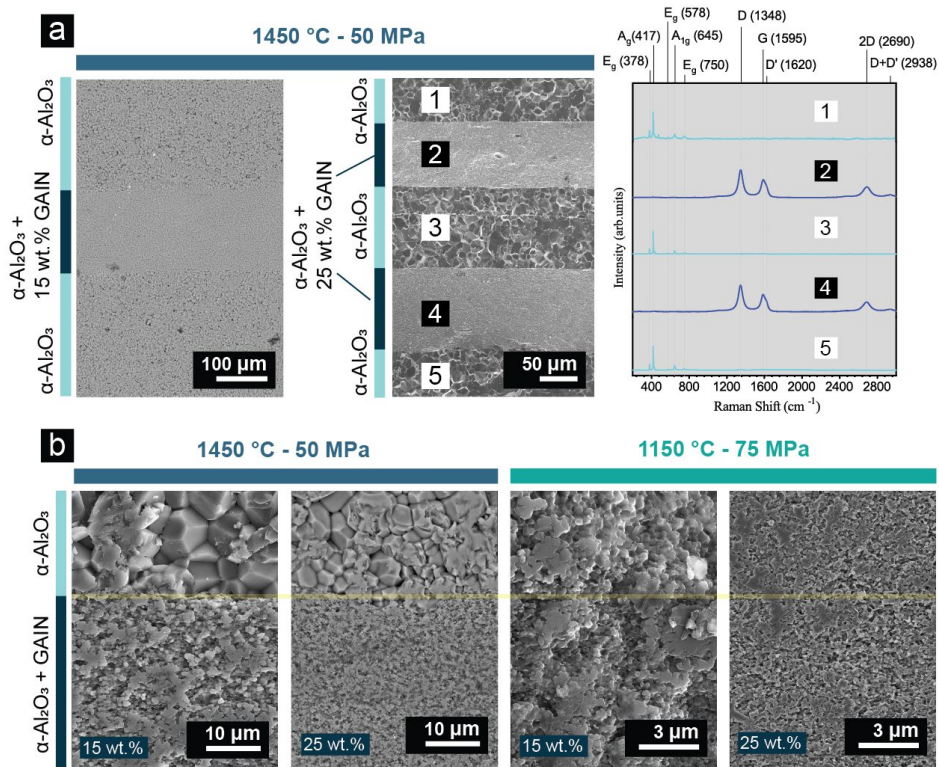
45

Figure 3.9 *(a) Microstructure of multilayers with AGA and AGAGA sequence and Raman spectra of each layer averaged from 10 readings; (b) SEM images of the interface between the interlayers (GAIN/α-Al₂O₃) and alumina layers for samples sintered at high and low temperature.*

As discussed in **Section 3.2.1** the grain refinement is due to the presence of GAIN fibers which hinders the migration of GBs (Drozdova et al., 2016). Moreover, the joule heating phenomenon which evidently manifests at elevated temperature (>1000 °C) in the form of local high temperature fields further affects the microstructural evolution and limits grain growth. In **Figure 3.9**b, the α-Al₂O₃-GAIN/α-Al₂O₃ interfaces of samples with 15 and 25 wt.% GAIN sintered at high temperature are compared to samples with 15 and 25 wt.% GAIN sintered at 1150 °C (low temperature approach – LT). For the discussion regarding the SPS at high and low temperature, refer to **Section 2.2.3**. Both lower sintering temperature and a higher GAIN content result in grain refinement not only in the GAIN/α-Al₂O₃ interlayers but also in the monolithic alumina layers. **Figure 3.9**b shows the grain of ~5 μm in the monolithic alumina layer of the sample with 15wt% GAIN sintered at 1450 °C are slightly refined (~2 μm) when the filler content in the interlayer was increased to 25 wt%. The grain size analysis is detailed in **Paper I**. Nonetheless, the grain sizes in the samples sintered at high temperature are significantly larger than those in the samples sintered at low temperature. In fact, both 15 and 25 wt.% GAIN in the interlayers of the samples sintered at 1150 °C generate microstructures that are somewhat identical in the interlayers and the monolithic layers; moreover, a higher level of densification reflected in the higher relative density of those samples is achieved. The average grain sizes in the interlayers of the samples sintered at low temperature are 400 and 300 nm for samples with 15 wt % GAIN and 25 wt % GAIN,

respectively. Raman spectroscopy shows the main features of discontinuous few-layer graphene with 2D, G, and D+D' peaks present after sintering under both SPS approaches. In **Figure *3.10*a**, the Raman spectra obtained from the interlayers of the samples with 15 and 25 wt.% GAIN sintered at 1450 °C and 1150 °C, are compared; to study the influence of the sintering procedure on the graphene quality and structure. The ~1.18 and ~2.62 I_D/I_G ratios and the ~0.45 and 0.83 $I_{D'}/I_G$ ratios for the samples 25%-HT and 25%-LT, respectively. The I_D/I_G and $I_{D'}/I_G$ ratios for GAIN fibers are 1.82 and 0.71, respectively (refer to **Section 3.1.1**). An increase in G band intensity in sample 25%-HT and the reduction in the D' shoulder at the G band can be possible indicators of purification of C–H bondings (dehydrogenation). Other indicators of this assumption are the lower D+D' intensity and the existing florescence slope (the slope is normalized in the graphs). The D+D' peak at ~2930 cm^{-1} is in response to functionalization of graphene and sp^3 hybridization. Meanwhile, the 2D band in all samples is blue shifted as compared to GAIN fibers, and this blue shift is 20 cm^{-1} more in HT samples in respect to LT samples. In contrast, the G band in the HT samples is not shifted as compared to GAIN while in LT samples it is 11 cm^{-1} blue shifted. In theory, for graphene structures, the blue shift of the 2D band is in connection with compressive stresses and p-doping while the blue shift of the G band is a response to compressive stresses and both n- and/or p-doping. Since the p-doping was evidentially proven to exist irrespective of the sintering temperature, one can only assume that the higher 2D shift in the HT samples and the shift in the G band of the LT samples are in connection to residual stresses formed during the sintering procedure which is consistent with the significant grain size difference between the HT and LT samples. Raman mapping of the interface of a multilayer sample is presented in **Figure *3.10*b**. The location of the G, 2D, and D+D' for the GAIN fillers before sintering are highlighted with dash lines in the histograms in Figure 2o. A more in-depth Raman characterization of the sintered structures is provided in **Paper I, III, and IV**.
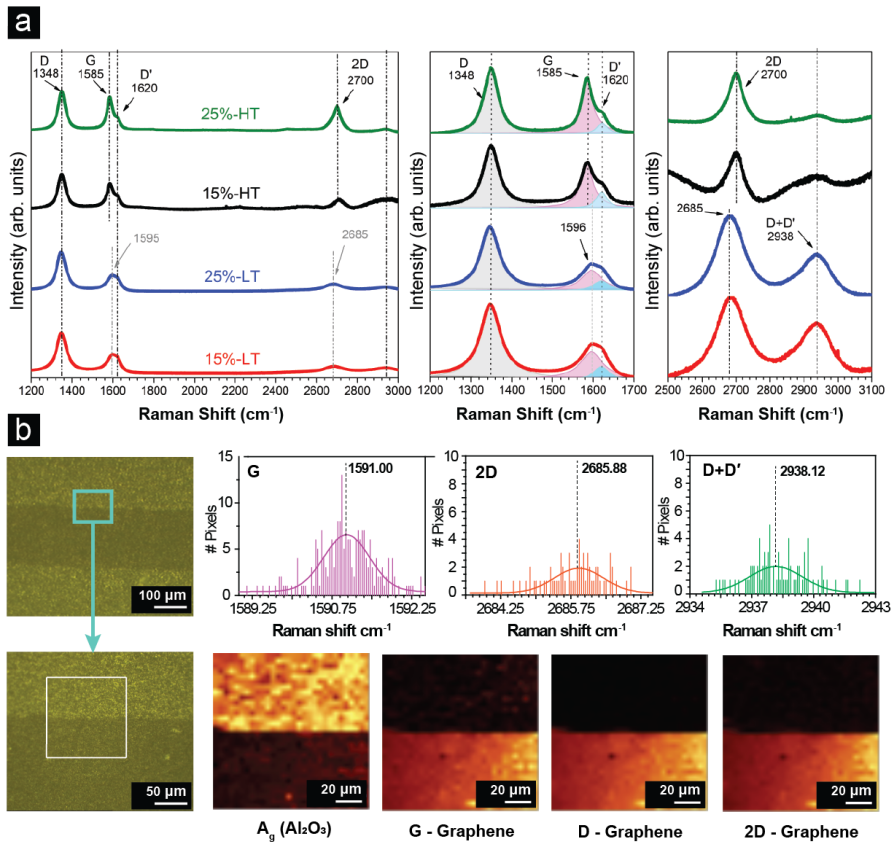
Figure 3.10 *(a) Raman spectra of the interlayer in samples with AGA design sintered at low temperature approach (LT) and high temperature approach (HT) (explained in 2.2.3) (the figure is adopted with permission from **Paper I** (Shamshirgar et al., 2020)); (b) Raman mapping of the interface between GAIN/α-Al₂O₃ interlayer and alumina outerlayer of a sample sintered at low temperature.*

3.3.2 Mechanical properties

Vickers microhardness (HV0.5) was measured on a multilayer with two alumina outerlayers and 5 interlayers of 1, 3, 5, 15, and 25 wt.% GAIN. The microhardness results are specified in **Figure 3.11**a, and a schematic representation of the multilayer structure is provided in **Figure 3.11**b. The hardness values are arithmetic mean of five readings from each layer. In both alumina layers presence of intragranular porosity is visible, however, in layer G1, were 1 wt.% of GAIN fillers are introduced, a refinement of the microstructure together with a lower level of porosity results in a slight increase in hardness reaching a value of ~21 GPa (**Figure 3.11**c). In the layers with GAIN fillers >3 wt.%, hardness decreases with increasing filler content, despite the grain refinement. In the pristine alumina layers, crack propagation trajectory is intragranular and in most cases stops at a porosity. In contrast, in the layers, were GAIN fibers are present, crack deflection and pinning effect is promoted which is more noticeable for G15 and G25 layers. The residual stresses formed during SPS are conducive to the dissipation of crack propagation energy, by deflecting and pinning their growth. On the other hand, the contribution of the fibers as the toughening agents may be stated due to presence of

fiber pullout shown in **Figure *3.11*d**. However, the fibers bridging mechanism was only observed in the samples sintered at 1150 °C. Absence of this mechanism in the samples sintered at 1450 °C can be attributed to the γ→α-Al$_2$O$_3$ phase transformation. A detailed analysis of mechanical properties is provided in **Paper I**.
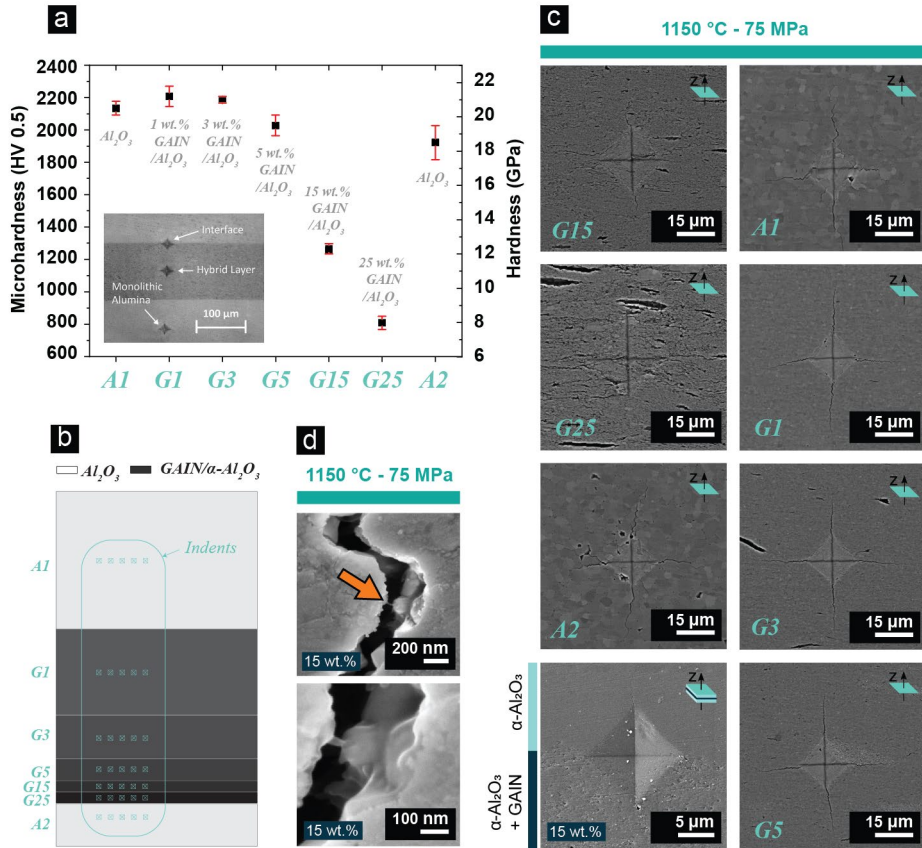

Figure 3.11 (a) Microhardness values for HV 0.5; (b) schematic representation of the test specimen; (c) microhardness indentations in various layers; (d) SEM images showing the presence of fiber pullout.

3.3.3 Electrical and thermal transport

A two-probe configuration was used to measure in-plane electrical conductivity of the multilayers with 15 and 25 wt.% GAIN in the interlayer, sintered at 1150 ° and 1450 °C (**Figure *3.12*a**). The thickness of the interlayers in all samples are 100 μm, except that for comparison, one sample is made with interlayer thickness of 500 μm (25%-HT-500). Electrical conductivity is generally higher for 25 wt.% GAIN, however, the samples sintered at low temperature (1150 °C) show much higher conductivity attributed to smaller grain size, preventing the γ→α-Al$_2$O$_3$ phase transition, and higher densification. The sample with 500 μm interlayer thickness shows a room temperature electrical conductivity of ~2000 S·m^{-1} which is about one-fold higher than the value for a similar sample with 100 μm interlayer thickness. For the same sample, a more prominent temperature dependence of electrical conductivity signals a more semiconducting behavior as compared to semi-metallic nature of the those with 100 μm. The isotropic

double-sided transient plane source measurement was performed on composites with one interlayer with varying thickness. In **Figure *3.12*b**, thermal conductivity and diffusivity are plotted as a function of interlayer thickness in sandwiched structures with 15 wt.% GAIN in the interlayer. Presence of an interlayer with only 50 μm thickness augments thermal conductivity by ~25 %. However, increasing thickness does not change the thermal transport of the bulk. A detailed analysis of the thermal transport in the multilayers is provided in **Paper II**.
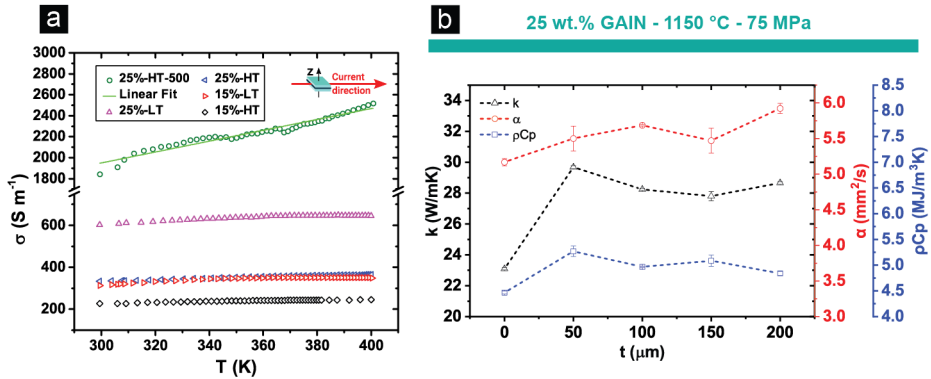

Figure 3.12 *(a) In-plane electrical conductivity vs. temperature in sandwiched structures (adopted with permission from **Paper I** (Shamshirgar et al., 2020); (b) thermal properties of sandwiched structures as a function of interlayer thickness (adopted with permission from **Paper II** (Hussainova et al., 2020).*

3.3.4 EMI shielding and microwave absorption efficiency

In the **Section 3.2.5** it was shown that homogeneous composites of GAIN/α-Al$_2$O$_3$ with GAIN contents higher than 3 wt.% offer EMI SE higher than 25 dB. However, it was also shown that poor microwave absorption performance of the homogeneous bulks is attributed to a significant impedance mismatch, resulting in RL values higher than -3 dB. In contrast, a suitable microwave absorber candidate must meet the prerequisite condition of RL <-10 dB (Zhao et al., 2016). Subsequently, the obtained dielectric properties of the bulks were employed in impedance matching technique based on **Equations 4–6**. The Monte Carlo simulation described in **Section 2.4** yielded various solutions for multilayer designs, some of which are presented in **Figure *3.13***. Design solutions of FSM-S1 and FSM-S3 are proposed to provide near-full X-band >95 % absorption due to a better impedance matching **Figure *3.13*b**. For the experimental verification of the findings, one of the findings with a gradient in GAIN content consisting of two alumina outerlayers and five interlayers of 1, 3, 5, 15, and 25 wt.% GAIN was chosen promising to have an absorption peak of -32 dB around 9.5 GHz with a bandwidth of 3 GHz mitigating the RL <-10 dB condition (FSM-89-1). Three additional variations of this sample were manufactured for comparison with simulated data (FSM-89-2, FSM-144-1, and FSM-144-2). A schematic representation of the specimens is provided in **Figure *3.14***.
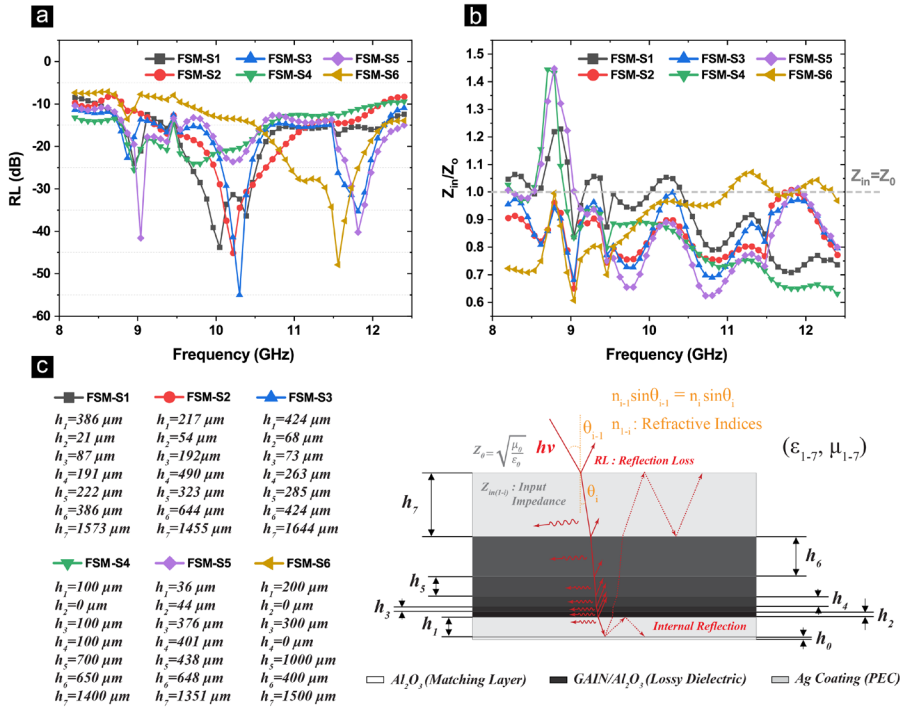
Figure 3.13 *(a) Reflection loss vs frequency for absorber design solutions obtained from Monte-Carlo approach to impedance matching; (b) normalized input impedance for the simulated solutions; and (c) the corresponding design parameters for the proposed solutions where h_1-h_7 are the thicknesses of the layers in micrometer and h_2-h_6 inversely correspond to G1-G25 composite structures. The figure is adopted with permission from* **Paper III** *(Shamshirgar et al., 2021).*

Reflection loss was obtained in a short-backed configuration in a rectangular waveguide with the fundamental TE10 mode and a one-port reflection-only setup (for nonmagnetic specimens, $\mu' = 1$ and $\mu'' = 0$). In this method, considering the samples are backed by PEC, the power of the incident wave (P_{in}) is composed of three parts: the reflected power (P_r), the absorbed power, and the transmitted power (P_t). Since the samples are backed by PEC, the transmitted power can be zero. Hence, the absorption power can be calculated using $P_a = P_{in}$-P_r. That is to say, by measuring the RL values in a one-port setup, the absorption efficiency can be calculated.

FSM-89-1

$$Z_0 = \sqrt{\frac{\mu_0}{\varepsilon_0}}$$

Incident Wave (E_0, H_0) Reflected Wave (E_r, H_r)

Z_{in}

ε_1, μ_1

ε_2, μ_2

ε_n, μ_n

Al$_2$O$_3$ [wt.%]	GAIN [wt.%]	Height [μm]
100		1597
99	1	610
97	3	377
95	5	233
85	15	144
75	25	89
100		610

Additional Multilayer Designs

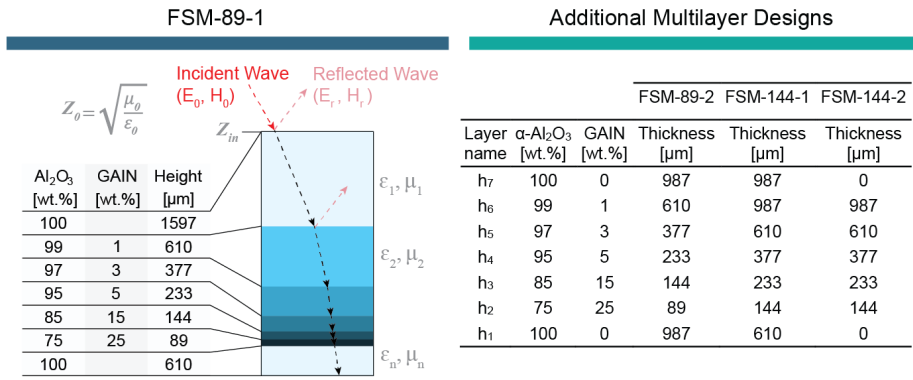| Layer name	α-Al$_2$O$_3$ [wt.%]	GAIN [wt.%]	FSM-89-2 Thickness [μm]	FSM-144-1 Thickness [μm]	FSM-144-2 Thickness [μm]
h$_7$	100	0	987	987	0
h$_6$	99	1	610	987	987
h$_5$	97	3	377	610	610
h$_4$	95	5	233	377	377
h$_3$	85	15	144	233	233
h$_2$	75	25	89	144	144
h$_1$	100	0	987	610	0

Figure 3.14 The thickness and compositions of the multilayer designs.

The experimental RL values are compared to the simulation data in **Figure 3.15**a, and the corresponding Z_{in} values of the multilayers are shown in **Figure 3.15**b. It is evident that FSM-89-1 with a total of 1.98 wt.% GAIN corresponding to ~0.24 wt.% carbon content offers a broadband 90 % absorption covering almost the entire X-band and a narrow 0.5 GHz bandwidth of 99 % absorption centered at 9.6 GHz. The sample FSM-144-1 with higher layer thicknesses satisfies full X-band 90 % absorption. The best impedance matching corresponds to FSM-89-1 with an optimal region satisfying the $|Z_{in}/Z_0|$ =1 condition between 9 and 10 GHz, which represents the same frequency region where the experimental data on the reflection loss reach a minimum at -40 dB. A detailed characterization is provided in **Paper III**.
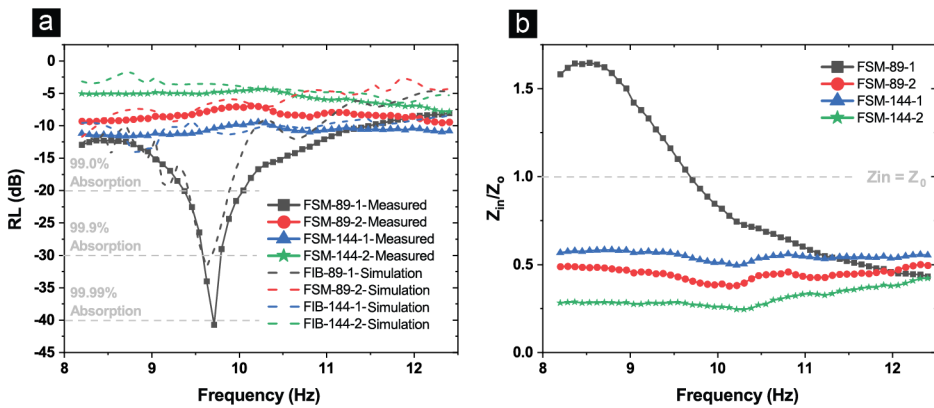
Figure 3.15 (a) Comparison of the simulated and measured reflection loss in multilayers; (b) input impedance ratio relative to free space.

Conclusions

In this work, a novel type of tunable functional multilayer composites consisting of alumina and graphene augmented inorganic nanofibers (GAIN) was introduced for application in efficient microwave absorption. Furthermore, the as-developed GAIN structures have shown a remarkable potential for thermoelectric applications. A bottom-up catalyst-free hot-wall CVD process was employed to obtain the GAIN fibers applied as conductive fillers in the composite structures. Comprehensive theoretical and experimental cross-verification was performed to characterize the homogeneous and multilayered composites of GAIN/α-Al$_2$O$_3$. As a result, the anisotropic hierarchically structured composites have been developed, optimized and evaluated to deliver an efficient multilayered architecture for providing a range of the required properties including but not limited to enhanced X-band absorption, high strength, and anisotropic thermal and electrical properties.

Based on the outcomes of the work, the following conclusions can be drawn:

(I)   Controllable and tunable graphene layers are deposited onto γ-Al$_2$O$_3$ nanofibrous substrate and thoroughly characterized revealing the presence of stretched polycrystalline few-layer graphene. A mixed carrier transport with a Hall coefficient crossover from n-type to p-type at ~270 K was observed.

(II)   The composite structures of GAIN/α-Al$_2$O$_3$ with various contents of GAIN have been fabricated by spark plasma sintering. In the matrix of alumina, GAIN fillers inhibit grain growth during SPS, resulting in fine-structured materials, while lowering sintering temperature to 1150 °C resulted in further grain refinement and prevents $\gamma \rightarrow \alpha$-Al$_2O_3$ transition.

(III)   Although increasing GAIN filler content above 5 wt.% in homogeneous composites results in a significant deterioration of hardness, the introduced porosity is shown to have practical implications in thermoelectric performance and attenuation of microwave radiations. Both thermal conductivity and diffusivity are anisotropic in the homogeneous bulks with a higher in-plane values corresponding to GAIN contents above 5 wt.%. The thermal conductivity decreases with an increase in GAIN content, which is attributed to various scattering phenomena. Reduced thermal conductivity at higher filler contents increases thermoelectric Figure of Merit of the structures as a function of GAIN.

(IV)   The sandwich and multilayer structures of GAIN/α-Al$_2$O$_3$ are successfully produced and the sintering routes are optimized to manufacture the materials of the designed architectures.

(V)   In-plane electrical conductivity is slightly higher than cross-plane values while the room temperature value of 1800 S·m^{-1} has been obtained for a

sandwiched structures with a 500 μm interlayer of 25 wt.% GAIN. Complex permittivity increases to the extremely high values of ~400 with an increase of the content of conductive GAIN additives, while permeability approaches zero due to diamagnetic response of the graphene-augmented fibers. The high permittivity of the structures ensures highly efficient EMI shielding effectiveness with the highest value of 45 dB obtained for 25 wt.% GAIN in α-Al_2O_3.

(VI)   A functional multilayer with a gradient in the GAIN content, designed on the basis of impedance matching technique, exhibits a full X-band absorption of >90 % and a narrowband -40 dB absorption peak centered at 9.6 GHz. The obtained absorption properties have shown to be a clear enhancement as compared to the homogeneous composites, attributed to maximized power transfer and efficient use of the entire absorber thickness.

(VII)   Various multilayer designs have indicated the tunability of the structures, rendering them excellent candidates for frequency specific and broadband microwave absorption.

References

Aghayan, M., Hussainova, I., Gasik, M., Kutuzov, M., & Friman, M. (2013). Coupled thermal analysis of novel alumina nanofibers with ultrahigh aspect ratio. *Thermochimica Acta*, *574*, 140–144. https://doi.org/10.1016/j.tca.2013.10.010

Amollo, T. A., Mola, G. T., Kirui, M. S. K., & Nyamori, V. O. (2018). Graphene for Thermoelectric Applications: Prospects and Challenges. *Critical Reviews in Solid State and Materials Sciences*, *43*(2), 133–157. https://doi.org/10.1080/10408436.2017.1300871

Balandin, A. A. (2011). Thermal properties of graphene and nanostructured carbon materials. *Nature Materials*, *10*(8), 569–581. https://doi.org/10.1038/nmat3064

Balandin, A. A., Ghosh, S., Bao, W., Calizo, I., Teweldebrhan, D., Miao, F., & Lau, C. N. (2008). Superior Thermal Conductivity of Single-Layer Graphene. *Nano Letters*, *8*(3), 902–907. https://doi.org/10.1021/nl0731872

Bansal, N. P., & Lamon, J. (2003). Ceramic-Matrix Composites. In *Handbook of Advanced Ceramics* (Vol. 2–2, pp. 417–443). https://doi.org/10.1016/B978-012654640-8/50042-0

Blackburn, J. L., Ferguson, A. J., Cho, C., & Grunlan, J. C. (2018). *Carbon-Nanotube-Based Thermoelectric Materials and Devices*. *1704386*, 1–35. https://doi.org/https://doi.org/10.1002/adma.201704386

Bradly, C. J., & Cracknell, A. P. (1972). *The Mathematical Theory of Symmetry in Solids*. Clarendon Press Oxford.

Çelik, Y., Çelik, A., Flahaut, E., & Suvaci, E. (2016). Anisotropic mechanical and functional properties of graphene-based alumina matrix nanocomposites. *Journal of the European Ceramic Society*, *36*(8), 2075–2086. https://doi.org/10.1016/j.jeurceramsoc.2016.02.032

Chase Jr., M. W. (1998). NIST-JANAF Themochemical Tables, 4th Edition. *J. Phys. Chem. Ref. Data*, (Monograph 9), 1–1951. https://doi.org/10.18434/T42S31

Chen, C., Pan, L., Jiang, S., Yin, S., Li, X., Zhang, J., … Yang, J. (2018). Electrical conductivity, dielectric and microwave absorption properties of graphene nanosheets/magnesia composites. *Journal of the European Ceramic Society*, *38*(4), 1639–1646. https://doi.org/10.1016/j.jeurceramsoc.2017.11.052

Chen, H., Ma, W., Huang, Z., Zhang, Y., Huang, Y., & Chen, Y. (2019). Graphene-Based Materials toward Microwave and Terahertz Absorbing Stealth Technologies. *Advanced Optical Materials*, *7*(8), 1801318. https://doi.org/10.1002/adom.201801318

Chen, M., Zhu, Y., Pan, Y., Kou, H., Xu, H., & Guo, J. (2011). Gradient multilayer structural design of CNTs/SiO2 composites for improving microwave absorbing properties. *Materials & Design*, *32*(5), 3013–3016. https://doi.org/10.1016/j.matdes.2010.12.043

Cole, M. T., Lindvall, N., & Yurgens, A. (2012). Noncatalytic chemical vapor deposition of graphene on high-temperature substrates for transparent electrodes. *Applied Physics Letters*, *100*(2), 022102. https://doi.org/10.1063/1.3675632

Das, A., Pisana, S., Chakraborty, B., Piscanec, S., Saha, S. K., Waghmare, U. V., … Sood, A. K. (2008). Monitoring dopants by Raman scattering in an electrochemically top-gated graphene transistor. *Nature Nanotechnology*, *3*(4), 210–215. https://doi.org/10.1038/nnano.2008.67

de Faoite, D., Browne, D. J., Chang-Díaz, F. R., & Stanton, K. T. (2012). A review of the processing, composition, and temperature-dependent mechanical and thermal properties of dielectric technical ceramics. *Journal of Materials Science*, *47*(10), 4211–4235. https://doi.org/10.1007/s10853-011-6140-1

Delfini, A., Albano, M., Vricella, A., Santoni, F., Rubini, G., Pastore, R., & Marchetti, M. (2018). Advanced Radar Absorbing Ceramic-Based Materials for Multifunctional Applications in Space Environment. *Materials*, *11*(9), 1730. https://doi.org/10.3390/ma11091730

Drozdova, M., Hussainova, I., Pérez-Coll, D., Aghayan, M., Ivanov, R., & Rodríguez, M. A. (2016). A novel approach to electroconductive ceramics filled by graphene covered nanofibers. *Materials & Design*, *90*, 291–298. https://doi.org/10.1016/j.matdes.2015.10.148

Fan, Y., Jiang, W., & Kawasaki, A. (2012). Highly Conductive Few-Layer Graphene/Al 2 O 3 Nanocomposites with Tunable Charge Carrier Type. *Advanced Functional Materials*, *22*(18), 3882–3889. https://doi.org/10.1002/adfm.201200632

Fan, Y., Wang, L., Li, J., Li, J., Sun, S., Chen, F., … Jiang, W. (2010). Preparation and electrical properties of graphene nanosheet/Al2O3 composites. *Carbon*, *48*(6), 1743–1749. https://doi.org/10.1016/j.carbon.2010.01.017

Ferrari, A C, & Robertson, J. (2001). Origin of the 1150-cm-1 Raman mode in nanocrystalline diamond. *Physical Review B*, *63*(12), 121405. https://doi.org/10.1103/PhysRevB.63.121405

Ferrari, Andrea C. (2007). Raman spectroscopy of graphene and graphite: Disorder, electron–phonon coupling, doping and nonadiabatic effects. *Solid State Communications*, *143*(1–2), 47–57. https://doi.org/10.1016/j.ssc.2007.03.052

Ferrari, Andrea C., & Basko, D. M. (2013). Raman spectroscopy as a versatile tool for studying the properties of graphene. *Nature Nanotechnology*, *8*(4), 235–246. https://doi.org/10.1038/nnano.2013.46

Foa Torres, L. E. F., Roche, S., & Charlier, J.-C. (2013). Introduction to Graphene-Based Nanomaterials. In *Introduction to Graphene-Based Nanomaterials*. https://doi.org/10.1017/CBO9781139344364

Geim, A. K., & Novoselov, K. S. (2007). The rise of graphene. *Nature Materials*, *6*(3), 183–191. https://doi.org/10.1038/nmat1849

Ghosh, S., Harish, S., Ohtaki, M., & Saha, B. B. (2020). Enhanced figure of merit of cement composites with graphene and ZnO nanoinclusions for efficient energy harvesting in buildings. *Energy*, *198*, 117396. https://doi.org/10.1016/j.energy.2020.117396

Green, M., & Chen, X. (2019). Recent progress of nanomaterials for microwave absorption. *Journal of Materiomics*, *5*(4), 503–541. https://doi.org/10.1016/j.jmat.2019.07.003

Guillon, O., Gonzalez-Julian, J., Dargatz, B., Kessel, T., Schierning, G., Räthel, J., & Herrmann, M. (2014). Field-Assisted Sintering Technology/Spark Plasma Sintering: Mechanisms, Materials, and Technology Developments. *Advanced Engineering Materials*, *16*(7), 830–849. https://doi.org/10.1002/adem.201300409

Hong, G., Han, Y., Schutzius, T. M., Wang, Y., Pan, Y., Hu, M., … Poulikakos, D. (2016). On the Mechanism of Hydrophilicity of Graphene. *Nano Letters*, *16*(7), 4447–4453. https://doi.org/10.1021/acs.nanolett.6b01594

Huang, Y., & Wan, C. (2020). Controllable fabrication and multifunctional applications of graphene/ceramic composites. *Journal of Advanced Ceramics*, *9*(3), 271–291. https://doi.org/10.1007/s40145-020-0376-7

Hussainova, I., Ivanov, R., Stamatin, S. N., Anoshkin, I. V., Skou, E. M., & Nasibulin, A. G. (2015). A few-layered graphene on alumina nanofibers for electrochemical energy conversion. *Carbon*, *88*(May 2016), 157–164. https://doi.org/10.1016/j.carbon.2015.03.004

Hussainova, I., Shamshirgar, A. S., Ivanov, R., Volobujeva, O., Romanov, A. E., & Gasik, M. (2020). Directional conductivity in layered alumina. *Current Applied Physics*, (October 2019). https://doi.org/10.1016/j.cap.2020.06.009

Ivanov, R., Hussainova, I., Aghayan, M., Drozdova, M., Pérez-Coll, D., Rodríguez, M. A., & Rubio-Marcos, F. (2015). Graphene-encapsulated aluminium oxide nanofibers as a novel type of nanofillers for electroconductive ceramics. *Journal of the European Ceramic Society*, *35*(14), 4017–4021. https://doi.org/10.1016/j.jeurceramsoc.2015.06.011

Ju, D., Kim, D., Yook, H., Han, J. W., & Cho, K. (2019). Controlling Electrostatic Interaction in PEDOT:PSS to Overcome Thermoelectric Tradeoff Relation. *Advanced Functional Materials*, *29*(46), 1905590. https://doi.org/10.1002/adfm.201905590

Koepke, J. C., Wood, J. D., Estrada, D., Ong, Z. Y., He, K. T., Pop, E., & Lyding, J. W. (2013). Atomic-scale evidence for potential barriers and strong carrier scattering at graphene grain boundaries: A scanning tunneling microscopy study. *ACS Nano*, *7*(1), 75–86. https://doi.org/10.1021/nn302064p

Krenkel, W., & Renz, R. (2008). CMCs for Friction Applications. In *Ceramic Matrix Composites: Fiber Reinforced Ceramics and their Applications*. https://doi.org/10.1002/9783527622412.ch16

Kumari, L., ZHANG, T., DU, G., LI, W., WANG, Q., DATYE, A., & WU, K. (2008). Thermal properties of CNT-Alumina nanocomposites. *Composites Science and Technology*, *68*(9), 2178–2183. https://doi.org/10.1016/j.compscitech.2008.04.001

Kutuzov, M. (2013). *Method And System For Alumina Nanofibers Synthesis From Molten Aluminum. Patent Application Publication. Pub. No.: US 2013/0192517 A1*. *1*(19).

L. Deyu, B.H. O'Connor, G.I.D Roach, J. .C. (1990). Structural models for η and γ alumina by x-ray Rietveld Refinement. *Acta Crystallographica Section A*, *46*(61).

Lamouri, S., Hamidouche, M., Bouaouadja, N., Belhouchet, H., Garnier, V., Fantozzi, G., & Trelkat, J. F. (2017). Control of the γ-alumina to α-alumina phase transformation for an optimized alumina densification. *Boletín de La Sociedad Española de Cerámica y Vidrio*, *56*(2), 47–54. https://doi.org/10.1016/j.bsecv.2016.10.001

Lee, M., Park, K., Park, J., Choi, D. K., & Song, Y. W. (2017). Oxygen-Dependent Synthesis of Graphene on γ-Alumina Catalyst. *Advanced Materials Interfaces*, *4*(17), 1–6. https://doi.org/10.1002/admi.201700603

Levin, I., & Brandon, D. (2005). Metastable Alumina Polymorphs: Crystal Structures and Transition Sequences. *Journal of the American Ceramic Society*, *81*(8), 1995–2012. https://doi.org/10.1111/j.1151-2916.1998.tb02581.x

Lewis, J., Schwarzenbach, D., & Flack, H. D. (1982). Electric field gradients and charge density in corundum, α-Al2O3. *Acta Crystallographica Section A*, *38*(5), 733–739. https://doi.org/10.1107/S0567739482001478

Li, W., Jin, H., Zeng, Z., Zhang, L., Zhang, H., & Zhang, Z. (2017). Flexible and easy-to-tune broadband electromagnetic wave absorber based on carbon resistive film sandwiched by silicon rubber/multi-walled carbon nanotube composites. *Carbon*, *121*, 544–551. https://doi.org/10.1016/j.carbon.2017.06.034

Li, X., Cai, W., Colombo, L., & Ruoff, R. S. (2009). Evolution of Graphene Growth on Ni and Cu by Carbon Isotope Labeling. *Nano Letters*, *9*(12), 4268–4272. https://doi.org/10.1021/nl902515k

Malekpour, H., & Balandin, A. A. (2018). Graphene Applications in Advanced Thermal Management. In *Nanopackaging* (pp. 823–865). https://doi.org/10.1007/978-3-319-90362-0_27

Mencarelli, D., Pierantoni, L., Stocchi, M., & Bellucci, S. (2016). Efficient and versatile graphene-based multilayers for EM field absorption. *Applied Physics Letters*, *109*(9), 093103. https://doi.org/10.1063/1.4962148

Meng, F., Wang, H., Huang, F., Guo, Y., Wang, Z., Hui, D., & Zhou, Z. (2018). Graphene-based microwave absorbing composites: A review and prospective. *Composites Part B: Engineering*, *137*(November 2017), 260–277. https://doi.org/10.1016/j.compositesb.2017.11.023

Micheli, D., Apollo, C., Pastore, R., Barbera, D., Morles, R. B., Marchetti, M., … Moglie, F. (2012). Optimization of Multilayer Shields Made of Composite Nanostructured Materials. *IEEE Transactions on Electromagnetic Compatibility*, *54*(1), 60–69. https://doi.org/10.1109/TEMC.2011.2171688

Micheli, D., Apollo, C., Pastore, R., & Marchetti, M. (2010). X-Band microwave characterization of carbon-based nanocomposite material, absorption capability comparison and RAS design simulation. *Composites Science and Technology*, *70*(2), 400–409. https://doi.org/10.1016/j.compscitech.2009.11.015

Miranzo, P., García, E., Ramírez, C., González-Julián, J., Belmonte, M., & Isabel Osendi, M. (2012). Anisotropic thermal conductivity of silicon nitride ceramics containing carbon nanostructures. *Journal of the European Ceramic Society*, *32*(8), 1847–1854. https://doi.org/10.1016/j.jeurceramsoc.2012.01.026

Okhay, O., Zlotnik, S., Xie, W., Orlinski, K., Hortiguela Gallo, M. J., Otero-Irurueta, G., … Tkach, A. (2019). Thermoelectric performance of Nb-doped SrTiO3 enhanced by reduced graphene oxide and Sr deficiency cooperation. *Carbon*, *143*, 215–222. https://doi.org/10.1016/j.carbon.2018.11.023

Panwar, R., & Lee, J. R. (2019). Recent advances in thin and broadband layered microwave absorbing and shielding structures for commercial and defense applications. *Functional Composites and Structures*, *1*(3), 032001. https://doi.org/10.1088/2631-6331/ab2863

Park, J., Lee, J., Choi, J. H., Hwang, D. K., & Song, Y. W. (2015). Growth, Quantitative Growth Analysis, and Applications of Graphene on γ-Al2O3 catalysts. *Scientific Reports*, *5*(June), 1–12. https://doi.org/10.1038/srep11839

Park, K., Lee, S., Kim, C., & Han, J. (2006). Fabrication and electromagnetic characteristics of electromagnetic wave absorbing sandwich structures. *Composites Science and Technology*, *66*(3–4), 576–584. https://doi.org/10.1016/j.compscitech.2005.05.034

Phelps, G. W., & Wachtman, J. B. (2000). Ceramics, General Survey. In *Ullmann's Encyclopedia of Industrial Chemistry*. https://doi.org/10.1002/14356007.a06_001

Pisana, S., Lazzeri, M., Casiraghi, C., Novoselov, K. S., Geim, A. K., Ferrari, A. C., & Mauri, F. (2007a). Breakdown of the adiabatic Born–Oppenheimer approximation in graphene. *Nature Materials*, *6*(3), 198–201. https://doi.org/10.1038/nmat1846

Pisana, S., Lazzeri, M., Casiraghi, C., Novoselov, K. S., Geim, A. K., Ferrari, A. C., & Mauri, F. (2007b). Breakdown of the adiabatic Born–Oppenheimer approximation in graphene. *Nature Materials*, *6*(3), 198–201. https://doi.org/10.1038/nmat1846

Qing, Y. C., Zhou, W. C., Jia, S., Luo, F., & Zhu, D. M. (2010). Electromagnetic and microwave absorption properties of carbonyl iron and carbon fiber filled epoxy/silicone resin coatings. *Applied Physics A: Materials Science and Processing*, *100*(4), 1177–1181. https://doi.org/10.1007/s00339-010-5738-5

Rahman, J. U., Du, N. Van, Nam, W. H., Shin, W. H., Lee, K. H., Seo, W.-S., … Lee, S. (2019). Grain Boundary Interfaces Controlled by Reduced Graphene Oxide in Nonstoichiometric SrTiO3-δ Thermoelectrics. *Scientific Reports*, *9*(1), 8624. https://doi.org/10.1038/s41598-019-45162-7

Ramírez, C., Belmonte, M., Miranzo, P., Osendi, M. I., Ramírez, C., Belmonte, M., … Osendi, M. I. (2021). Applications of Ceramic/Graphene Composites and Hybrids. *Materials*, *14*(8), 2071. https://doi.org/10.3390/ma14082071

Ramirez, C., Leborán, V., Rivadulla, F., Miranzo, P., & Osendi, M. I. (2016). Thermopower and hall effect in silicon nitride composites containing thermally reduced graphene and pure graphene nanosheets. *Ceramics International*, *42*(9), 11341–11347. https://doi.org/10.1016/j.ceramint.2016.04.056

Rohini, R., & Bose, S. (2019). Electrodeposited carbon fiber and epoxy based sandwich architectures suppress electromagnetic radiation by absorption. *Composites Part B: Engineering*, *161*, 578–585. https://doi.org/10.1016/j.compositesb.2018.12.123

Russ, B., Glaudell, A., Urban, J. J., Chabinyc, M. L., & Segalman, R. A. (2016). Organic thermoelectric materials for energy harvesting and temperature control. *Nature Reviews Materials*, *1*(10), 16050. https://doi.org/10.1038/natrevmats.2016.50

Saffar Shamshirgar, A., Belmonte, M., Tewari, G. C., Rojas Hernández, R. E., Seitsonen, J., Ivanov, R., … Hussainova, I. (2021). Thermal Transport and Thermoelectric Effect in Composites of Alumina and Graphene-Augmented Alumina Nanofibers. *Materials*, *14*(9), 2242. https://doi.org/10.3390/ma14092242

Saito, R., Hofmann, M., Dresselhaus, G., Jorio, A., & Dresselhaus, M. S. (2011). Raman spectroscopy of graphene and carbon nanotubes. *Advances in Physics*, *60*(3), 413–550. https://doi.org/10.1080/00018732.2011.582251

Sebastian, M. T. (2017). *Microwave Materials and Applications 2V Set* (M. T. Sebastian, H. Jantunen, & R. Ubic, eds.). https://doi.org/10.1002/9781119208549

Shamshirgar, A. S., Rojas Hernández, R. E., Tewari, G. C., Fernández, J. F., Ivanov, R., Karppinen, M., & Hussainova, I. (2021). Functionally Graded Tunable Microwave Absorber with Graphene-Augmented Alumina Nanofibers. *ACS Applied Materials & Interfaces*, *13*(18), 21613–21625. https://doi.org/10.1021/acsami.1c02899

Shamshirgar, A. S., Rojas Hernández, R. E., Tewari, G. C., Ivanov, R., Mikli, V., Karppinen, M., & Hussainova, I. (2020). Layered structure of alumina/graphene-augmented-inorganic-nanofibers with directional electrical conductivity. *Carbon*, *167*, 634–645. https://doi.org/10.1016/j.carbon.2020.06.038

Shi, S.-L., & Liang, J. (2008). The effect of multi-wall carbon nanotubes on electromagnetic interference shielding of ceramic composites. *Nanotechnology*, *19*(25), 255707. https://doi.org/10.1088/0957-4484/19/25/255707

Singh, V., Joung, D., Zhai, L., Das, S., Khondaker, S. I., & Seal, S. (2011). Graphene based materials: Past, present and future. *Progress in Materials Science*, *56*(8), 1178–1271. https://doi.org/10.1016/j.pmatsci.2011.03.003

Srivastava, D., Norman, C., Azough, F., Ekren, D., Chen, K., Reece, M. J., … Freer, R. (2019). Anisotropy and enhancement of thermoelectric performance of Sr 0.8 La 0.067 Ti 0.8 Nb 0.2 O 3−δ ceramics by graphene additions. *Journal of Materials Chemistry A*, *7*(42), 24602–24613. https://doi.org/10.1039/C9TA02883H

Stamatin, S. N., Hussainova, I., Ivanov, R., & Colavita, P. E. (2016). Quantifying Graphitic Edge Exposure in Graphene-Based Materials and Its Role in Oxygen Reduction Reactions. *ACS Catalysis*, *6*(8), 5215–5221. https://doi.org/10.1021/acscatal.6b00945

Stankovich, S., Dikin, D. A., Piner, R. D., Kohlhaas, K. A., Kleinhammes, A., Jia, Y., … Ruoff, R. S. (2007). Synthesis of graphene-based nanosheets via chemical reduction of exfoliated graphite oxide. *Carbon*, *45*(7), 1558–1565. https://doi.org/10.1016/j.carbon.2007.02.034

Tanner, C. M., Perng, Y.-C., Frewin, C., Saddow, S. E., & Chang, J. P. (2007). Electrical performance of Al2O3 gate dielectric films deposited by atomic layer deposition on 4H-SiC. *Applied Physics Letters*, *91*(20), 203510. https://doi.org/10.1063/1.2805742

Tapasztó, L., Nemes-Incze, P., Dobrik, G., Jae Yoo, K., Hwang, C., & Biró, L. P. (2012). Mapping the electronic properties of individual graphene grain boundaries. *Applied Physics Letters*, *100*(5). https://doi.org/10.1063/1.3681375

Thomas, S. (2018). Advanced Materials for Electromagnetic Shielding. In M. Jaroszewski, S. Thomas, & A. V. Rane (Eds.), *Advanced Materials for Electromagnetic Shielding*. https://doi.org/10.1002/9781119128625

Tsoukleri, G., Parthenios, J., Papagelis, K., Jalil, R., Ferrari, A. C., Geim, A. K., … Galiotis, C. (2009). Subjecting a Graphene Monolayer to Tension and Compression. *Small*, *5*(21), 2397–2402. https://doi.org/10.1002/smll.200900802

Vázquez, E., & Prato, M. (2009). Carbon Nanotubes and Microwaves: Interactions, Responses, and Applications. *ACS Nano*, *3*(12), 3819–3824. https://doi.org/10.1021/nn901604j

Venezuela, P., Lazzeri, M., & Mauri, F. (2011). Theory of double-resonant Raman spectra in graphene: Intensity and line shape of defect-induced and two-phonon bands. *Physical Review B*, *84*(3), 035433. https://doi.org/10.1103/PhysRevB.84.035433

Wang, G., Gao, Z., Tang, S., Chen, C., Duan, F., Zhao, S., … Qin, Y. (2012). Microwave Absorption Properties of Carbon Nanocoils Coated with Highly Controlled Magnetic Materials by Atomic Layer Deposition. *ACS Nano*, *6*(12), 11009–11017. https://doi.org/10.1021/nn304630h

Wei, J., Yang, L., Ma, Z., Song, P., Zhang, M., Ma, J., … Wang, X. (2020). Review of current high-ZT thermoelectric materials. *Journal of Materials Science*, *55*(27), 12642–12704. https://doi.org/10.1007/s10853-020-04949-0

Wu, Y., Chou, H., Ji, H., Wu, Q., Chen, S., Jiang, W., … Ruoff, R. S. (2012). Growth Mechanism and Controlled Synthesis of AB-Stacked Bilayer Graphene on Cu–Ni Alloy Foils. *ACS Nano*, *6*(9), 7731–7738. https://doi.org/10.1021/nn301689m

Xu, X., Pereira, L. F. C., Wang, Y., Wu, J., Zhang, K., Zhao, X., … Özyilmaz, B. (2014). Length-dependent thermal conductivity in suspended single-layer graphene. *Nature Communications*, *5*(1), 3689. https://doi.org/10.1038/ncomms4689

Yalamaç, E., Trapani, A., & Akkurt, S. (2014). Sintering and microstructural investigation of gamma–alpha alumina powders. *Engineering Science and Technology, an International Journal*, *17*(1), 2–7. https://doi.org/10.1016/j.jestch.2014.02.001

Yazyev, O. V., & Chen, Y. P. (2014). Polycrystalline graphene and other two-dimensional materials. *Nature Nanotechnology*, *9*(10), 755–767. https://doi.org/10.1038/nnano.2014.166

Ye, F., Song, C., Zhou, Q., Yin, X., Han, M., Li, X., … Cheng, L. (2018). Broadband Microwave Absorbing Composites with a Multi-Scale Layered Structure Based on Reduced Graphene Oxide Film as the Frequency Selective Surface. *Materials*, *11*(9), 1771. https://doi.org/10.3390/ma11091771

Yuchang, Q., Qinlong, W., Fa, L., & Wancheng, Z. (2016). Temperature dependence of the electromagnetic properties of graphene nanosheet reinforced alumina ceramics in the X-band. *Journal of Materials Chemistry C*, *4*(22), 4853–4862. https://doi.org/10.1039/C6TC01163B

Zhan, G.-D., & Mukherjee, A. K. (2005). Carbon Nanotube Reinforced Alumina-Based Ceramics with Novel Mechanical, Electrical, and Thermal Properties. *International Journal of Applied Ceramic Technology*, *1*(2), 161–171. https://doi.org/10.1111/j.1744-7402.2004.tb00166.x

Zhang, Q., Lin, D., Deng, B., Xu, X., Nian, Q., Jin, S., … Cheng, G. J. (2017). Flyweight, Superelastic, Electrically Conductive, and Flame-Retardant 3D Multi-Nanolayer Graphene/Ceramic Metamaterial. *Advanced Materials*, *29*(28), 1605506. https://doi.org/10.1002/adma.201605506

Zhao, B., Guo, X., Zhao, W., Deng, J., Shao, G., Fan, B., … Zhang, R. (2016). Yolk–Shell Ni@SnO 2 Composites with a Designable Interspace To Improve the Electromagnetic Wave Absorption Properties. *ACS Applied Materials & Interfaces*, *8*(42), 28917–28925. https://doi.org/10.1021/acsami.6b10886

Zhou, M., Lin, T., Huang, F., Zhong, Y., Wang, Z., Tang, Y., … Lin, J. (2013). Highly Conductive Porous Graphene/Ceramic Composites for Heat Transfer and Thermal Energy Storage. *Advanced Functional Materials*, *23*(18), 2263–2269. https://doi.org/10.1002/adfm.201202638

Acknowledgements

Abstract
Hierarchically Structured Functional Ceramic Composites with Graphene Augmented Nanofibers

Graphene has shown remarkable potential for various applications such as EMI shielding and thermoelectric applications due to its tunable nature and unique properties. This work, motivated by the pressing need for development of multifunctional materials for microwave absorption for advanced applications such as 5G development, focuses on the design and characterization of alumina based functional multilayers using graphene augmented inorganic nanofibers (GAIN). The GAIN fibers were obtained using a hot-wall CVD process that greatly simplifies the graphene deposition without the need for catalysts. The as-developed graphene on alumina nanofibers shows a polycrystalline nature that stems from several sp^2 nucleation centers originated from the surface defects of the substrate γ-Al_2O_3 nanofibers. Homogeneous composites of GAIN/α-Al_2O_3 with filler contents of 1, 3, 5, 15, and 25 wt.% were successfully processed using ultrasonication in ethanol and sintered using spark plasma sintering (SPS). The characterization of the obtained homogeneous composite structures shows that the addition of the fillers up to 3 wt.% increases hardness of polycrystalline α-Al_2O_3 and that the presence of the fibers in the microstructure offer crack bridging and deflection. Electrical conductivity increases by increasing GAIN fibers while the electrical percolation threshold was achieved at 1 wt.% GAIN corresponding to remarkably low ~0.21 vol.% carbon content. Electrical conductivity reaches ~1500 S·m^{-1} at highest filler content (25 wt.%) at room temperature while the semi-metallic nature of the transport results in conductivity of ~850 S·m^{-1} at 4 K in the same sample. Raman spectroscopy, Hall measurement, and Seebeck coefficient, all confirm the p-doping of the graphene in the presence of electron accepting Al interstitials and O vacancies in the matrix α-Al_2O_3. The p-doping was shown to contribute to the decrease in phonon mean free path (1–3 nm) enforced by defect and impurity scatterings. As a result, thermal conductivity decreases as a function of GAIN fibers from 35 W·m^{-1}·K^{-1} in polycrystalline α-Al_2O_3 to ~10 W·m^{-1}·K^{-1} for 25 wt.% GAIN/α-Al_2O_3 composite. The decrease in thermal conductivity together with increasing Seebeck coefficient and electrical conductivity, all as a function of GAIN content have granted the highest thermoelectric Figure of Merit to composites with 15 and 25 wt.% GAIN. The thermoelectric characterization has shown the remarkable potential of the GAIN filler materials for enhancing thermoelectric device efficiency. Furthermore, integration of a thin hybrid interlayer of GAIN/α-Al_2O_3 into the assembly of alumina sandwiched structures was shown to slightly improve the thermal conductivity of the sintered bulk alumina.

Presence of various defects and scattering points, the conductive-dielectric core-shell structure of GAIN, and their integration into the α-Al_2O_3 matrix ensured a significant increase in the complex permittivity as a function of GAIN tested in the X-band. The outcome of this increased permittivity was remarkable electromagnetic shielding effectiveness of the structures, which was correlated to high surface scattering. In order to decrease the surface scattering phenomenon and enhance microwave absorption, a multilayer structure with a gradient in GAIN content and layer thickness was fabricated and tested using transmission line method in a rectangular waveguide under the fundamental TE10 mode. The result has shown a significant enhancement of the absorption (>90 %) in X-band with a narrowband peak of -40 dB corresponding to 99.99 % absorption centered at 9.6 GHz. The fabricated functional multilayer structures

and several simulated solutions indicate the exceptional potential of the GAIN fibers and the developed methodology for development of high efficiency broadband or frequency specific microwave absorbers offering tunability of the absorption spectrum.

Lühikokkuvõte
Hierarhiliselt struktureeritud funktsionaalsed keraamilised komposiidid grafeenlisandiga nanokiududega

Grafeen, tingituna oma ainulaadsetest ja suunatavatest omadustest omab arvestatavat potentsiaali, leidmaks kasutust erinevates tehnilistes rakendustes, näiteks elektromagnetiliste häiringute varjestamisel ning termoelektrilistes rakendustes. See töö lähtub vajadusest välja arendada mikrolaine absorbermaterjale 5G süsteemide jaoks ning keskendub alumiiniumoksiidil põhinevate funktsionaalsete mitmekihiliste materjalisüsteemide, täpsemalt grafeenlisandiga anorgaaniliste nanokiudude (GAIN) saamisele ja kirjeldamisele. GAIN-kiud saadi keemilise aurusadestuse (CVD) protsessiga, mis võimaldab grafeeni sadestamist substraadile suhteliselt lihtsalt, ilma katalüsaatori abita. Alumiiniumoksiidi nanokiududele sadestatud grafeen on polükristallilise struktuuriga, mis tuleneb paljude sp^2 kristallisatsioonikeskmete olemasolust. Kristallisatsioonikeskmeteks on substraadi γ-Al_2O_3 nanokiudude pinnadefektid. Homogeense koostisega GAIN/α-Al_2O_3 komposiidid, täiteaine sisaldusega 1, 3, 5, 15 ja 25 massiprotsenti töödeldi ultraheliga etanoolis ja paagutati seejärel edukalt sädeplasmapaagutuse (SPS) abil. Saadud homogeensete komposiitstruktuuride uurimisel leiti, et täiteainete lisamine kuni 3 massiprotsenti suurendab polükristallilise α-Al_2O_3 kõvadust ning et kiud takistavad pragude levikut maatriksis eeskätt sildamismehhanismi kaudu ning muutes nende kulgemise suunda (deflektsioonimehhanism).

Elektrijuhtivus suureneb GAIN-kiudude sisalduse suurendamisel, samal ajal kui elektriline perkolatsioonilävi saavutati 1 massiprotsendi GAIN-ga, mis vastab märkimisväärselt madalale ~0,21 mahu% süsinikusisaldusele. Parim elektrijuhtivus ~1500 $S \cdot m^{-1}$ mõõdeti toatemperatuuril suurima täiteaine sisalduse (25 massi%) juures, samas kui juhi poolmetalliliste omaduste tõttu on juhtivus samas proovis 4 K juures ~850 $S \cdot m^{-1}$. Raman spektroskoopia, Halli efekti mõõtmine ja Seebecki koefitsiendi mõõtmine kinnitavad grafeeni p-dopeeringu olemasolu α-Al_2O_3 maatriksis, mis sisaldab elektronide liikuvuseks vajalikke Al-aatomeid ja O vakantse. Näidati, et p-dopeering aitab kaasa foononi keskmise vaba tee (1–3 nm) vähenemisele, mis on tingitud materjalis hajutatud defektidest ja lisanditest. Selle tulemusena väheneb soojusjuhtivus sõltuvalt GAIN-kiudude sisaldusest: polükristallilises α-Al_2O_3 on see 35 $W \cdot m^{-1} \cdot K^{-1}$ alanedes kiudude lisamisel tasemele ~10 $W \cdot m^{-1} \cdot K^{-1}$ (25 massi% GAIN/α-Al_2O_3 komposiidis). Soojusjuhtivuse vähenemine koos Seebecki koefitsiendi ja elektrijuhtivuse suurenemisega on GAIN-sisalduse funktsioonina andnud kõrgeima termoelektrilise omaduste kompleksnäitaja komposiitidele, mille GAIN-i sisaldus on 15 ja 25 massiprotsenti. Termoelektriliste omaduste mõõtmisega tõendati GAIN-i täitematerjalide märkimisväärset potentsiaali termoelektrilise seadme efektiivsuse suurendamiseks. Lisaks näidati, et GAIN/α-Al_2O_3 õhukese hübriidse vahekihi lisamine alumiiniumoksiidiga ühendatud struktuuride koostisesse parandab veidi paagutatud alumiiniumoksiidi soojusjuhtivust.

Erinevate defektide ja hajumispunktide olemasolu, GAIN-i iseloomustav juhtiv-dielektriline südamiku-kesta struktuur ja GAIN kiudude sisseviimine α-Al_2O_3 maatriksisse tagas X-sagedusribal testitud materjali kompakspermitiivsuse olulise kasvu. Suurenenud permitiivsuse tulemusel paranesid loodud struktuuridel märkimisväärselt elektromagnetilised varjustus-omadused, mis on seotud elektromagnetkiirguse suurenenud hajumisega pinnalt. Pinnalt hajumise nähtuse vähendamiseks ja

mikrolainete absorbtsiooni parandamiseks valmistati GAIN-i sisalduse ja kihi paksuse gradiendiga mitmekihiline struktuur, mida testiti ülekandeliini meetodil ristkülikukujulises lainejuhis põhirežiimis TE10. Loodud materjalisüsteemil täheldati neeldumise olulist suurenemist (>90 %) X-ribas kitsa ribapiigiga -40 dB, mis vastab 99,99% neeldumisele, mille keskpunkt on 9,6 GHz. Valmistatud funktsionaalsed mitmekihilised struktuurid ja mitmed töös kasutatud simulatsioonide abil saadud lahendused iseloomustavad GAIN-kiudude suurt potentsiaali ja välja töötatud meetodite põhimõttelist toimivust lairiba-või sagedusspetsiifiliste ja neeldumisspektri häälestatavust võimaldavate mikrolaineabsorberite väljaarendamisel.

Appendix

Paper I

Saffar Shamshirgar, A., Rojas Hernández, R. E., Tewari, G. C., Ivanov, R., Mikli, V., Karppinen, M., & Hussainova, I. (2020). Layered structure of alumina/graphene-augmented-inorganic-nanofibers with directional electrical conductivity. Carbon, 167, 634–645. https://doi.org/10.1016/j.carbon.2020.06.038
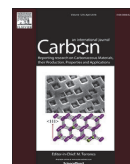Reproduced with the permission of Elsevier.

Layered structure of alumina/graphene-augmented-inorganic-nanofibers with directional electrical conductivity

Ali Saffar Shamshirgar [a], Rocio Estefania Rojas Hernández [a], Girish C. Tewari [b], Roman Ivanov [a], Valdek Mikli [c], Maarit Karppinen [b], Irina Hussainova [a, *]

[a] Department of Mechanical and Industrial Engineering, Tallinn University of Technology, Ehitajate tee 5, 19086, Estonia
[b] Department of Chemistry and Materials Science, Aalto University, P.O. Box 16100, FI-00076, Aalto, Finland
[c] Laboratory of Optoelectronic Materials Physics, Department of Material and Environmental Technology, Tallinn University of Technology, Ehitajate tee 5, 19086, Estonia

ARTICLE INFO

ABSTRACT

Implementation of layered structures with strong nanoscale optimized interfaces, enables engineering of materials with functional properties. In this work, anisotropic functional multi-layered structures are produced by integration of a thin hybrid inter-layer of graphene-augmented-nanofibers/alumina into α-alumina through an ex-situ strategy of precipitating the tailored hybrid from a solution. Spark plasma sintering was used to consolidate the layered structures at 1150 and 1450 °C under 75 and 50 MPa pressure. Raman spectroscopy suggests presence of C−H bonds and sp^3 hybridization for the samples sintered at 1150 °C, while graphene structure is purified at the sintering temperature of 1450 °C. The multilayer structures demonstrate a high in-plane electrical conductivity which can be modulated, ranging from 300 to 1800 S m^{-1} as a function of the interlayer thickness and the carbon content. A p-type conduction at room temperature and n-type down to 4 K in graphene-augmented nano-fillers was observed in Hall measurement. However, the multilayered systems display a p-type conduction in the entire temperature range. Hardness was preserved despite the high concentration of the graphene-augmented nano-fillers in the hybrid interlayer leaving a highest value of ~22 GPa. The results have the potential to fuel the development of functional electronic enclosures with additional functionalities such as electromagnetic interference shielding.

© 2020 Elsevier Ltd. All rights reserved.

1. Introduction

The technological development continuously imposes strong requirements for engineering materials with improved mechanical reliability and additional functionalities. To address this challenge, even widely used materials should demonstrate unprecedented combination of several, and sometimes mutually exclusive, properties. Ceramic materials, such as alumina (Al_2O_3), boron carbide (B_4C) and silicon carbide (SiC), are some of the most widely used ceramics for many industrial applications due to lightweight, high compressive strength, thermal stability and oxidation/corrosion resistance. However, brittle fracture behavior often limits reliability of these ceramics. A rational solution to this problem can be found in the Nature, which provides a rich source of inspiration by

locating specific compositions and architectures in assigned regions, generating multiple advantages within a bulk material. One of the examples is the layered structures that mimic the micro-structure of nacre and abalone shell, which are widely employed to improve toughness of otherwise brittle materials [1,2].

Biological materials can exhibit remarkable combinations of stiffness, strength, toughness, and low density, which are in some cases unmatched by synthetic materials [3]. However, through the incorporation of architected structures (i.e. multilayer, core-shell, etc.), some of these nature-developed structures can be techno-logically designed to meet versatile requirements and enhance functional performance. For instance, to increase mechanical efficiency, general design principle is the combination of stiff and relatively strong exterior with a weaker interior; for synthetic materials, layered architecture enables increase in fracture toughness through introduction of numerous interfaces. Many natural materials have evolved even some steps further to envisage addi-tion of non-mechanical functions such as the structure of skin

* Corresponding author.
E-mail addresses: irina.hussainova@taltech.ee, irhus@staff.ttu.ee (I. Hussainova).

which contains perspiration glands, sensory receptors, hair follicles, and blood vessels, together with basic functionality as a protecting layer. Similarly, in synthetic materials, addition of new functionalities such as an electro-conductive layer may allow for a directional materials response, i.e. high anisotropy in thermal and electrical conduction which opens venues for diverse applications including heat management [4], electro calorific effect [5], electromagnetic interference (EMI) shielding [6], multilayer ceramic capacitors, etc. Correspondingly, a wide variety of reinforcing and/or toughening additives such as fibers, carbon nanotubes and, recently, graphene nano-platelets, have been incorporated into ceramic matrices to increase damage tolerance of the final product [7,8]. These fillers can influence not only toughness but also give specific functionality to the material. Recently, graphene reinforced ceramics have attracted an unprecedented attention because of the extraordinary properties of graphene [9] combined with the inhibition of grain growth during sintering and subsequent enhancement in mechanical properties [10—12]. It should be noted that the term "graphene" refers exclusively to the pure monolayer of carbon atoms arranged in a honeycomb type structure [9]; nonetheless, different types of graphene-like structures (graphene nanoplatelets, graphene nano-sheets, graphene oxide sheets, reduced graphene oxide, etc.) are common for composites' reinforcement. Experimentally, it has been demonstrated that addition of graphene nanoplatelets to ceramic matrix also can enhance electrical conductivity by orders of magnitudes depending on the concentration of the fillers [12,13]. Similarly, enhanced conductivity of an insulating material such as alumina, by incorporation of nanorods, is shown to be dependent on the concentration and the aspect ratio of the conductive fillers [12,14], which affects the tunneling length and subsequently electrical percolation threshold [13—15]. On the other hand, a vast number of studies have proven that graphene fillers are suitable candidates for a variety of applications such as electromagnetic interference (EMI) shielding. Ru et al. in Ref. [16] achieved EMI shielding effectiveness >32 dB in the K band with less than 1 vol% rGO in a mullite matrix composite. Luo et al. doubled the dielectric constant of $BaTiO_3$ with 3 wt% addition of graphene nanosheets [17]. Subsequently, as far as additional functionality is concerned, alternating layers of copper/nickel and graphene with ultrahigh strength of 1.5—4 GPa has been reported by Kim et al. [15]. Directional electrical conductivity of 10^3 S m^{-1} in alternating layers of Si_2N_3 and graphene sheets has been demonstrated in Refs. [18]. Remarkable increase in in-plane conductivity as compared to the conductivity measured for the through-thickness direction is reported for Si_3N_4/graphene nanoplates [19], and composites of Al_2O_3/graphene nanoplates [20].

Nevertheless, high anisotropic electrical conductivity achieved in straightforward assemblies has merits for improvement. In this work, a bottom-up method of hot-wall chemical vapor deposition (CVD) has been used for production of the conductive nano-reinforcements. In this method, thermal decomposition of CH_4 at 1000 °C with hydrogen etching, assembles carbon atoms into polycrystalline graphene layers on the surface of γ-Al_2O_3 nanofibers that were used as substrate for growing graphene. The developed graphene-augmented alumina nanofibers (GAIN) described in detail elsewhere [8,21] employed in this work, meet electrical percolation threshold in an α-alumina composite at <3 wt % of the fillers loading (~0.39 wt% of calculated carbon content), and tunneling length of 2.23 nm [8,12,22]. To address the challenge of integrating new functionalities to ceramics together with maintaining or enhancement of their mechanical properties, this work employs the above-mentioned GAIN fillers and focuses on engineering of novel hierarchical ceramic hybrids with alternating layers owning high anisotropy in electrical properties. In this straightforward and cost-effective approach, alternating layers of α-alumina and alumina/graphene hybrids are constructed directly in the spark plasma sintering (SPS) die through a filtration method, which greatly simplifies the process. Ultimately, the sintered structures represent the integration of multiple gradients, namely, microstructural gradient in terms of grain size, porosity, and subsequently, mechanical properties; and anisotropic electrical properties. The developed structures could be potentially used for the fabrication of impact resistance structures, electrostatic charge dissipators, EMI shielding, or thermoelectric devices.

2. Experimental

2.1. Materials processing

The commercially available α-Al_2O_3 nano-powder with an average particle size of 100 nm (TM-DAR, Taimei, Japan) was used as the matrix material. Graphene augmented inorganic nanofibers (GAIN) were exploited as fillers in the hybrid interlayers. The graphene layers were grown on a surface of highly aligned alumina (γ-Al_2O_3) nanofibers [23] along the longitudinal axis by the means of a single step catalyst-free hot-wall CVD technique in a tube furnace kept at 1000 °C for 20 min. Aligned γ-alumina bundles of 4 cm long and 0.7 × 0.7 cm in cross section were prepared having ~0.15 g dry weight as substrate for CVD graphene. (see Supplementary Information, S1).

The ratios of 15 and 25 wt% loading of GAIN and 85—75 wt% α-Al_2O_3 nano-powder was weighted corresponding to a consolidated thickness of 100 μm for the interlayer of the samples with 20 mm diameter. A separate sample with 500 μm interlayer thickness was considered to investigate the contribution of thickness to electrical conductivity. The prepared compositions were dispersed in chloroform by a sonication rod (Hielscher UP400S) for 20 min at 30W using alternative regime 4 s ON - 1 s OFF. Two green pellets of α-Al_2O_3 nano-powder corresponding to a sintered thickness of 2 mm were produced under 5 MPa of pressure to insert as the top and bottom layers of the structures in the SPS die. The layered structure was implemented exploiting a pseudo-colloidal method, directly in a SPS graphite mold with diameter of 20 mm. A schematic of the sample preparation process is illustrated in Fig. 1a and detailed in Supplementary information, S2. The stacked materials were spark plasma sintered (Dr. Sinter SPS-510CE, Japan) in N_2 atmosphere at two different regimes: (i) 1450 °C with simultaneous 50 MPa uniaxial pressure for a dwell time of 10 min (hereafter abbreviated as high temperature (HT) approach); and (ii) 1150 °C with simultaneous 75 MPa uniaxial pressure for a dwell time of 10 min (hereafter abbreviated as low temperature (LT) approach). The two different regimes were used to understand how the phase evolution and subsequently microstructural features can be influenced by sintering temperature. With a focus on full densification, the HT sintering approach was used guided by a pervious study on spark plasma sintering of alumina [24] and following the procedure explained in detail elsewhere [25]. While, to avoid gamma to alpha phase transition in GAIN fibers, the experimental parameters of LT sintering approach where chosen guided by a pervious report on sintering of transparent alumina [26]. Table 1 provides full datasheet of the samples' compositions and sintering conditions. The heating rate was set to 200 °C/min between 600 and 1000 °C and then 100 °C/min. Moreover, to portrait versatility of the proposed pseudo-colloidal approach for implementing layered structures, a sample with three interlayers is manufactured in A-B-A-B-A fashion in which A stands for alumina layer and B stands for 25 wt% GAIN composite layers. All interlayers have similar thickness of 100 ± 10 μm μm (see Supplementary information, S3).
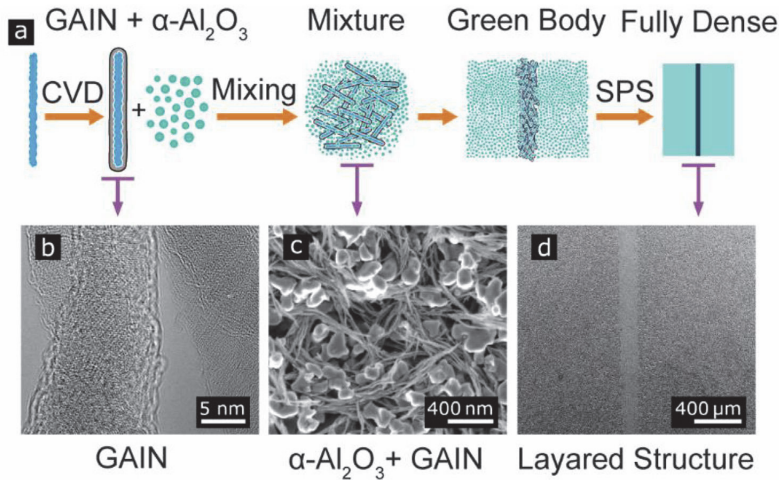
Fig. 1. (a) Schematic of the manufacturing steps to produce the layered structures, (b) TEM micrograph of the graphene-augmented γ-Al₂O₃ nanofibers, (c) SEM micrograph of the GAIN/α-Al₂O₃ dried suspension, (d) SEM of the hybrid interlayer sandwiched between layers of Al₂O₃ after SPS (sample 15%-HT). (A colour version of this figure can be viewed online.)

Table 1
Index of the samples and process parameters.

Designation	Sintering temperature(°C)	Pressure[MPa]	Hybrid layer thickness[μm]	Calculated GAIN[a][Wt.%]	Calculated Carbon[Wt.%]
15%-HT	1450	50	100	15	~1.95
15%-LT	1150	75	100	15	~1.95
25%-HT	1450	50	100	25	~3.25
25%-LT	1150	75	100	25	~3.25
25%-HT-500	1450	50	500	25	~3.25

[a] Graphene-augmented Inorganic Nanofibers.

2.2. Characterization

Carbon content of the CVD graphene augmented alumina nanofibers was determined using a LECO CS 200 carbon-Sulphur analyzer. Three measurements were made, and the arithmetic mean was used to calculate the corresponding carbon content of the composites. Resulting size of the fibers after mixing was determined by laser scattering method using Mastersizer 3000, Malvern Panalytical, equipped with a λ = 632.8 nm He−Ne laser.

The samples with final sintered thickness of 4 ± 0.1 mm were polished to 0.5 μm surface roughness using diamond disc and diamond suspension. Raman spectra of the as-synthesized multi-layered material were recorded using a Horiba's LabRAM 800 high-resolution spectrometer equipped with a 532 nm laser excitation wavelength at room temperature (RT) and a 50X objective lens (NA = 0.95). The incident laser power was 7 mW. Raman spectral resolution of the system was 1.5 cm⁻¹. For microstructural char-acterization of the fillers and bulks, a field emission scanning electron microscope (FEG-SEM Zeiss ULTRA-55, Germany) equipped with EDS (energy dispersive X-ray spectrometer, BRUKER, Esprit 1.82 system, USA) with voltage of up to 20 kV and magnifi-cations up to 50 kX was used. The grain size analysis was performed by imaging analysis method on SEM images considering at least 500 readings using Image Pro Plus 7.0 package by Media Cyber-netics. All the SEM images for this analysis were recorded at the same magnification (5000x) and at least three micrographs of each sample were analyzed to get statistics that are more reliable.

In plane DC electrical resistivity measurements were performed on the multilayered bars from room temperature to 400 K using a two-probe array. Prior to the measurement in order to prepare electrical probing areas, first, 80 nm Pt was deposited on the sides of the samples using a Cressington 308R coating system. Second, 0.5 mm Ag conductive paste was applied on top of the Pt coatings, and last, samples were thermal treated at 100 °C for 12 h in a muffle furnace in air. The low temperature transport properties (electrical resistivity and Hall coefficient) of the GAIN fillers and composites with 15 and 25 wt% of GAIN in alumina matrix were measured using a physical property measurement system (PPMS; Quantum design; equipped with 9 T magnetic field) with Hall bar configu-ration from 4K to 300K.

Vickers microhardness tests were carried out under 4.9 N load (HV0.5) using BUEHLER MICROMET 2001 equipped with a square-based orthogonal pyramidal diamond indenter on the cross section of the samples in 3 different regions: hybrid interlayer, monolithic alumina layer, and interface between the layers. The load was kept for 10 S for each indent. HV values were estimated from the average values of 10 indents in each region and converted to SI unit using Equation (1) according to Annex F, ISO 14577−1:2015.

$$HV = (H_{IT} \times A_p)/(g \times A_s) = 0.0945 \, H_{IT} \ (GPa) \tag{1}$$

In this equation, HV is the Vicker's hardness, H_{IT} indentation hardness, A_p projected area of the indenter, A_s contact surface area, and g is the gravitational acceleration. NanoTest Vantage (Micro-Materials ltd, UK) nanoindenter equipped with a diamond Berko-vich tip was used to perform the nanoindentation tests on well grinded and polished samples following the procedure outlined in

Ref. [27]. The tests were load-controlled and conducted at room temperature. Prior to the test, a calibration was performed on the Berkovich diamond indenter with hardness of 1140 GPa and Poisson's ratio of 0.07 using a standard fused silica specimen. Loading was performed at 10 mN/s with dwell time of 5s and unloading rate of 10 mN/s. The drift rate was preset to <0.05 nm/s before the beginning of each indentation test.

3. Results and discussion

3.1. Microstructure

After Processing, the resulting length of the graphenated fibers is measured to be ~700 ± 100 nm. From the FE-SEM micrograph of the alumina/GAIN mixture Fig. 1c homogeneous distribution of the fibers of 30:1 to 40:1 aspect ratio (fibers diameter is ~20 ± 5 nm) is recognizable. A cross section of the layered structure (15%-HT) with the hybrid interlayer sandwiched between two layers of monolithic alumina is shown in Fig. 1d. The presence of conductive fillers enables the local joule heating at elevated temperatures, providing a homogenous thermal distribution and hindering the migration of grain boundaries (GB) during SPS; therefore, a grain refinement in the interlayer, affected by the presence of the fillers is expectedly obtained [12,25]. Although highly resistive alumina powder (top and bottom layers of the multilayer) would prohibit the local joule heating in the early stages of the SPS, as the temperature increases, the resistivity of alumina sharply decreases (~10^4 Ω m at 1000 °C) [28,29] providing an electrical discharge path parallel to the SPS axis through the sample. Subsequently, the joule heating phenomenon manifests as local high temperature fields which impact the microstructural evolution [30]. Fig. 2 shows the microstructure and grain size distribution of different layers in the case of 15 wt % GAIN in (a,b,c), and 25 wt % GAIN in (d,e,f) for the samples sintered at 1450 °C under 50 MPa of pressure. Note that the microstructure of the 25%-HT and 25%-HT-500 are identical; therefore, only the micrographs of 25%-HT are chosen for comparison. It was previously mentioned that presence of GAIN impedes grain growth in

the interlayer. However, apart from that, the γ-alumina nature of the substrate nanofibers used for growing graphene grains can be the secondary attributing factor to the grain refinement. In fact, presence of few percentages of γ-alumina in an α matrix on its own is not an influencing factor, rather the contribution of the γ phase to densification by nucleation and grain growth through the transitional process of $\gamma \rightarrow \delta \rightarrow \theta \rightarrow \alpha$-Al$_2O_3$ is governing the sintering mechanism. In other words, presence of γ phase reduces the densification temperature to 1450 °C while this process starts in the temperature range of 1050−1200 °C depending on the particle size of the initial powder. The transition of $\theta \rightarrow \alpha$ can produce vermicular microstructure that forms a network of wide pores. The resulted porous structure requires temperatures higher than 1600 °C for high densification [31,32]. Presence of the vermicular microstructure is visible in Fig. 2e where the sample was sintered at 1450 °C with heating rate of 100 °C/min. Controlling the rearrangement of grains during $\theta \rightarrow \alpha$-Al$_2O_3$ transition by employing a significantly lower heating rate is one possible way to eliminate this structure [32]. However, as an alternative mechanism, the sintering temperature of 1150 °C was chosen in this work to avoid the phase transition of γ-Al$_2$O$_3$ used as CVD substrate to produce GAIN fibers. Supplementary information, S4, provides information on phase transformation of the GAIN at different temperatures. The temperature was chosen based on a previous thermal analysis done by the authors in Ref. [23]. On the other hand, the interlayer also contributes to the grain structure of the monolithic alumina layers. It is visible from Fig. 2a,d that average grain size in monolithic alumina is ~5 μm in the case of samples with 15 wt % GAIN interlayer. This is while, in the case of the sample with 25 wt % GAIN comparatively a slight grain refinement in the monolithic alumina layer is achieved with average grain size of ~2 μm. Additional SEM micrographs are presented in Fig. S5 for comparison of grain size of the monolithic alumina layers (see Supplementary information, S5). This can be attributed to a better heat distribution in the SPS die during the sintering, benefiting from a larger fibrous conductive filler content present in the interlayer. Nevertheless, the grain structure in the monolithic alumina is greatly larger as compared to
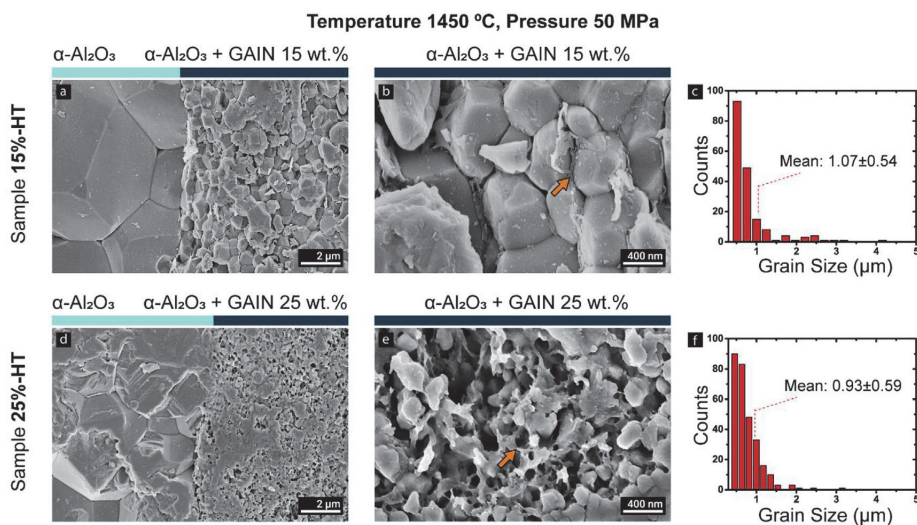
Fig. 2. SEM micrograph of SPS samples sintered at 1450 °C under 50 MPa; (a,d) interface between the hybrid layer and monolithic α-Al$_2$O$_3$, (b,e) interlayer in the sample with 15 and 25 wt % GAIN respectively - arrows pointing at GAIN fibers in the microstructure, (c,f) interlayer grain size distribution in samples with 15 and 25 wt % GAIN, respectively. (A colour version of this figure can be viewed online.)

the grains of hybrid interlayers. As a result, a sharp interface between the Al_2O_3 and interlayer has formed Fig. 2a,d. Fig. 3 displays the microstructure and grain size distribution of the layers in the case of 15 wt % GAIN in (a,b,c), and 25 wt % GAIN in (d,e,f) for the samples sintered at 1150 °C under 75 MPa of pressure. As demonstrated in Fig. 2b,e and Fig. 3b,e presence of 25 wt % GAIN which roughly is equal to a calculated 3.25 wt% of carbon content, results in a refined structure interlayer by hindering the migration of GB during sintering, independent of the sintering temperature. The arithmetic mean of carbon content in the GAIN fibers shows a value of 13 wt % which was used to determine the weight percentage of carbon in the hybrid interlayer of the layered structures. Although grains in the 25 wt % GAIN hybrid interlayer are much smaller than those in 15 wt % GAIN, the level of residual porosity seems to be much higher due to the presence of larger carbon content and its corresponding negative effect on the densification [33,34]. The Al_2O_3 grain refinement at low sintering temperature (1150 °C) generates a less coarse grain structure with much smaller grains in the monolithic layers. Subsequently, no interface is visible between the interlayer and the monolithic Al_2O_3 in the samples sintered at low temperature.

The yellow vertical lines in Fig. 3a,d shows the location of the interface that is visible only at low magnifications. Additional SEM images together with Raman spectroscopy graphs are presented in Supplementary information, S6, for further visualization of the locations of the interlayers and their corresponding compositions. The grains of the monolithic alumina in the case of 1150 °C sintering temperature have average sizes of 400 and 300 nm for samples with 15 wt % GAIN and 25 wt % GAIN hybrid interlayers respectively estimated from 10 readings in FE-SEM micrographs.

The pre-processing of the FE-SEM micrographs for determination of the grain size distribution includes usual steps of median filter and thresholding. However, unlike the monolithic grain structure, the grains in the interlayer could not be separated only by thresholding due to the presence of fibrous nano fillers, which form flaky layers at the GB areas. To overcome the issue, an additional watershed filter was applied. The filter successfully separated the

grains; however, the process uncertainty consists of occasional fragmented detection of the grains by the software. Hence, the absolute values of the results should not be taken as the actual grain size. Nonetheless, as all the images were processed and analyzed under the same steps, the results represent relatively realistic determinations for comparing the interlayers in the samples. As shown in Fig. 2c,f and Fig. 3c,f the grain size distribution is significantly narrower in the case of the low temperature sintering. The lower fraction of GAIN in 15%-LT results in a flatter distribution graph as compared to 25%-LT. Moreover, a larger population of finer grains are present in the samples with 15 wt% GAIN.

3.2. Mechanical properties

Three different regions were chosen to study the effect of the sintering conditions and the GAIN fraction on the mechanical properties of the multilayer structures. Micro-hardness indentations were introduced into the monolithic alumina, hybrid layer, and the interface between the layers. An optical image of the intended areas is shown in Fig. 4a; and Vicker's hardness (HV) values and nanoindentation data are summarized in Table 2. The values obtained for monolithic alumina are in a good agreement with the results obtained for fully dense alumina prepared by high pressure hot press, hot isostatic press or SPS techniques [35]. Nearly similar values were obtained for the samples 15%-HT, 15%-LT, and 25%-HT in three sections. However, in the case of the sample 25%-LT, the HV decreases down to 11.3 GPa as a result of high porosity at the interface and the hybrid layer. Amongst the samples, 15%-LT reveals the highest hardness values, in which the hybrid layer hardness of 22.2 GPa is comparable to hardness of monolithic alumina. This fact is conditioned by the combined effect of grain refinement and low level of porosity. A slight distortion in the indent shape seen in Fig. 4b can be explained by structural anisotropy. This anisotropy is developed due to two factors: (i) pressure-induced preferential grain growth during the SPS; and (ii) interaction of the DC field with the electrostatic charges of the GBs. In the vicinity of interlayer, the preferred orientation induced by

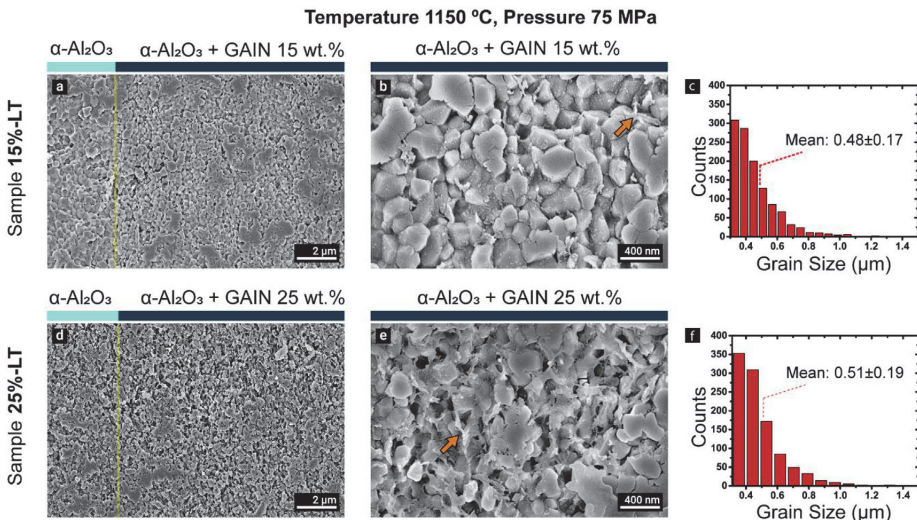**Fig. 3.** SEM micrograph of SPS samples sintered at 1150 °C under 70 MPa; (a,d) interface between the hybrid layer and monolithic α-Al_2O_3, (b,e) interlayer in the sample with 15 and 25 wt % GAIN respectively-arrows pointing at GAIN fibers in the microstructure, (c,f) interlayer grain size distribution in samples with 15 and 25 wt % GAIN, respectively. (A colour version of this figure can be viewed online.)
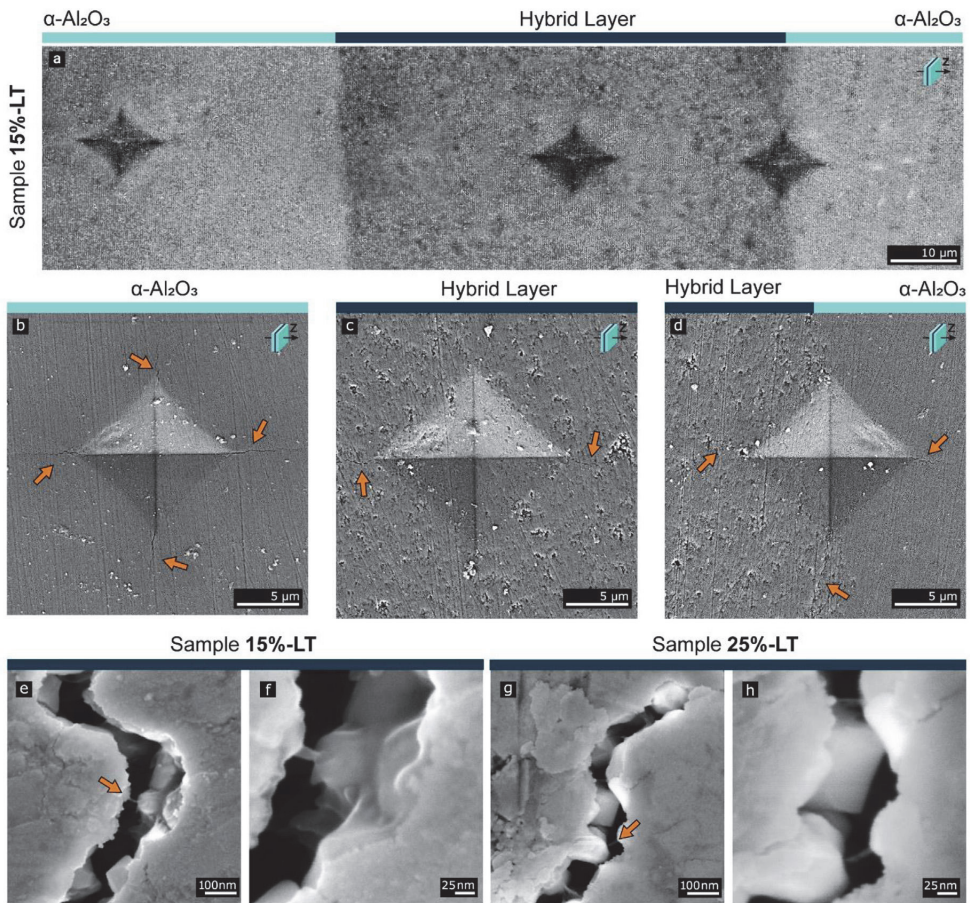
Fig. 4. (a) OM image of the Vicker's microhardness imprints, and SEM images of crack propagation from the sites of the indentations in the (b) monolithic Al_2O_3, (c) hybrid interlayer, (d) interface between the monolithic Al_2O_3 and the hybrid layer — arrows pointing at the propagated cracks, Fiber bridging in the interlayer of LT samples with (e,f) 15 and (g,h) 25 wt % GAIN, respectively. (A colour version of this figure can be viewed online.)

Table 2
Mechanical properties of the hybrid interlayer, monolithic α-Al_2O_3, and the interface between the two layers.

Sample Name	Relative Density	Monolithic Alumina			Hybrid layer			Interface
		H [GPa][a]	E [GPa][b]	W_e [%][c]	H [GPa][a]	E [GPa][b]	W_e [%][c]	H [GPa][a]
25%-LT	>99%	24.5 ± 0.7	475.1 ± 28.2	0.38 ± 0.03	11.3 ± 0.8	343.3 ± 29.7	0.29 ± 0.04	17.7 ± 0.5
25%-HT	99%	23.3 ± 0.5	451.2 ± 4.3	0.32 ± 0.06	17.7 ± 0.9	306.1 ± 63.1	0.26 ± 0.07	22.2 ± 0.9
15%-LT	>99%	24.5 ± 0.6	481.1 ± 14.1	0.36 ± 0.02	22.2 ± 0.5	356.1 ± 16.9	0.24 ± 0.05	24.5 ± 0.8
15%-HT	99%	22.2 ± 0.5	426.5 ± 34.8	0.37 ± 0.02	21.2 ± 0.8	326.7 ± 33.6	0.23 ± 0.05	22.2 ± 0.7

[a] Hardness (HV0.5 Microhardness).
[b] Modulus of Elasticity.
[c] Elastic Recovery.

SPS together with the opposite behavior of the coefficient of thermal expansion (CTE) of graphene and alumina, which result in CTE mismatch during the cooling process, promotes crack deflection and pinning. Fig. 4c demonstrates the cracks in the hybrid layer (15%-LT), which propagate in perpendicular direction to the interlayer plane (parallel to SPS pressure axis) indicating a weak c-axis intergranular interface. No developed crack system is observed parallel to the plane pointing at an increased toughness in the area

added by the fibers. Fig. 4d demonstrates the cracks evolved parallel to the hybrid layer plane at the interface. In Fig. 4 e-h, the fibers pull-out combined with crack' bridging can be considered as one of the toughening mechanisms.

The load-unload curves, fitted with the standard Oliver-Pharr procedure [36], are presented in Fig. 5a and b for the alumina and hybrid layers. Modulus of elasticity E was calculated using Equation (2), and reduced modulus E' (effective contact stiffness)
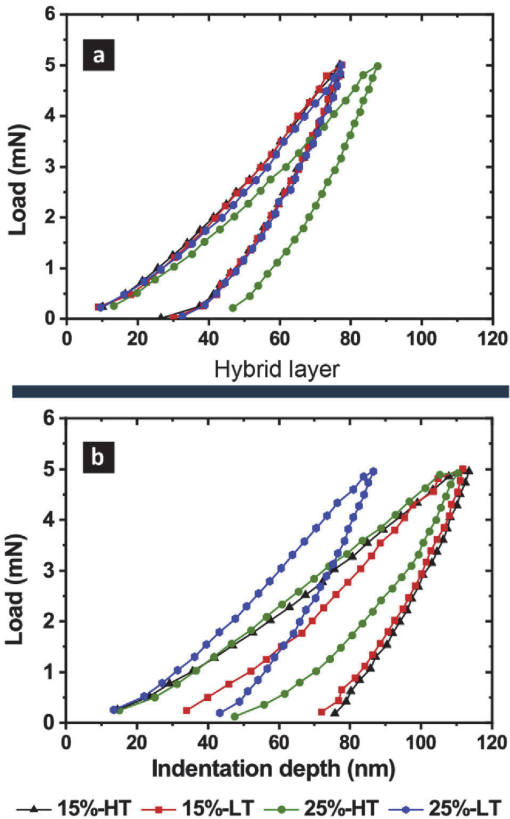
Fig. 5. Loading-Unloading nanoindentation curves for; (a) Al_2O_3 layers and (b) hybrid interlayers. (A colour version of this figure can be viewed online.)

was obtained from the nanoindentation test data. Fig. 5a displays an identical behavior of all samples except the sample 25%-HT with a slightly wider area under the curve and, correspondingly, a lower hardness of 21 GPa. The samples with 25 wt% GAIN reveal a higher elastic recovery in the interlayer area as compared to the samples with 15 wt% GAIN, which can be attributed to the increased level of porosity in the former case. While the modulus of elasticity of the monolithic alumina matches the reference data, the sample sintered at 1150 °C with 15 wt%. GAIN shows an enhancement in both hardness and modulus.

$$E^{'} = \left\{ \left(1 - \nu_s^2 \right) \middle/ E_s + \left(1 - \nu_i^2 \right) \middle/ E_i \right\}^{-1} \qquad (2)$$

3.3. Raman spectroscopy

Fig. 6 displays Raman spectra of the interlayers of the samples recorded using a 532 nm laser. Raman spectra of the GAIN fibers is presented in Fig. S1b (see Supplementary information, S1). All samples have demonstrated the main features of both graphene and bulk graphite, represented by G and 2D peaks. The G peak is driven by the high frequency E_{2g} phonons at Γ point of the Brillouin zone and is due to the stretching of the C–C bond in sp^2 atoms causing in-plane vibrations [37]. The disorder-induced D peak at 1348 cm^{-1} corresponds to breathing modes of sp^2 atoms in the

rings and can be used to monitor disorder in sp^2-hybridized carbon systems [37,38]. The D' shoulder at the G peak at ~1620 cm^{-1} is denoted to be in connection with the double resonance condition, when energy is conserved in multiple transitions (electron/hole pair, electron-phonon scattering, and defect scattering) producing phonons with small wave vector, which is characteristic of defected graphite [39].

In Fig. 6b, Pseudo-Voigt fitting has been carried out to show only the peak position of each component, whereas areas under the spectra have not been considered for any discussion. Granted that the I(D)/I(G) ratio is slightly higher for LT samples, it presumably is a result of a higher population of nanoscale defects present under the laser spot [40] attributed to the different grain size distribution in the interlayer. The double resonant Raman scattering theory suggests that the I(D)/I(D') is associated with the following defect types: (i) sp^3 defects (~13), (ii) hopping defects (~10.5), (iii) vacancy-like defects (~3.5), and iv) on-site defects (~1.3) [41,42]. The I(D)/I(D') ratio for all samples is between ~2.7 and ~3.2 with no observable impact of the sintering conditions which suggests a combined vacancy-like and on-site defected structure. The position of the G peak is shifted in the LT samples, which can be attributed to unintentional electron, and hole doping levels of the GAIN fibers, both resulting in a red-shift of the G mode [43,44]. This assumption is consistent with the p-type conduction of the hybrid interlayer at room temperature and a sign inversion of the Hall mobility in the GAIN fillers below room temperature discussed in section 3.4.1. On the other hand, the I(G) is proportional to the amount of sp^2 rings and its decrease can correspond to sp^3 formation [45]. Moreover, an increase in I(D)/I(G) and I(D')/I(G) ratios occurs by sp^3 formation [42]. The proposed concept is valid when comparing samples sintered at 1450 °C to those sintered at 1150 °C. For example, the I(D)/I(G) ratios for the samples 25%-HT and 25%-LT are ~1.18 and ~2.62 respectively. An increase is also observed for I(D')/I(G) ratios for the same samples having the values of ~0.04 and 0.83, respectively. Correlating the increased ratios in LT samples with decrease observed in E_{2g} band, a transition from nanocrystalline graphite to low sp^3 hybridization can be justified.

The second order of the D peak in bulk graphite consists of two components; whereas in all four samples, a single 2D peak is detected, which may correspond to either monolayer or few layer graphene. The 2D band in graphene at ~2670 cm^{-1} is caused by double resonance scattering of TO phonons at the k-point of the zone edge [46]. For multi-layered graphene, the 2D peak is about four times stronger than the G peak at ~1585 (the wider the peak gets at 2D region, the more layers of graphene are expected) [39]. For the tested structures, the I(2D)/I(G) ratio (visible in Fig. 6a) is roughly ½ with smallest FWHM of ~49 in HT samples, suggesting a more ordered graphene structure with the higher temperature of sintering. The normalized 2D peaks in samples sintered at 1450 °C show a 20 cm^{-1} red-shift marked with vertical dash lines in Fig. 6c. The red-shift agrees with results for turbostratic graphite [37], however, in the GAIN samples it is more likely to be a result of strain caused by interaction with substrate. The position of the 2D peak and the corresponding shift agrees with the results for graphene on sapphire in Ref. [47]. Functionalization of graphene with hydrogen and sp^3 hybridization introduce a peak at ~2930 cm^{-1}. For the HT samples a lower D + D' intensity, a 20 cm^{-1} red-shift of the 2D band, and the existing florescence slope (the slope is normalized in the graphs) may serve as possible indicators of purification of C–H bonding (dehydrogenation) which are sp^3 hybridized in LT samples. In other words, the hydrogen functionalized GAIN fibers are better purified in HT samples showing a higher I(2D)/I(G) ratio, narrower FWHM of the 2D, and flatter D + D' peak. In the LT samples the decreased I(G) and increased I(D')/I(G) and I(D)/I(G) ratios indicate possible sp^3 hybridization while the red-shifted G peak suggests
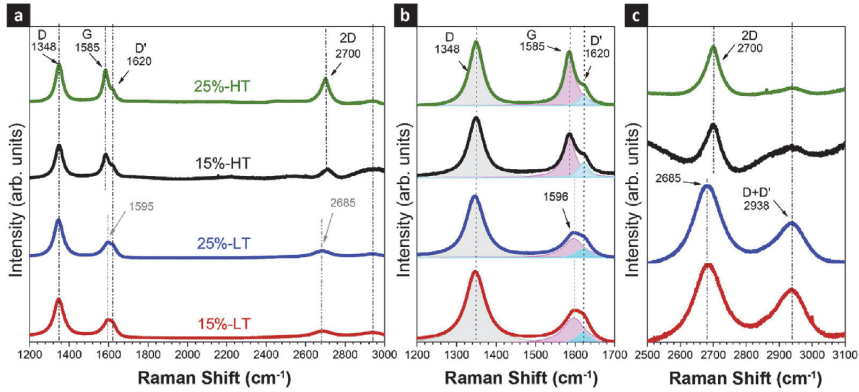
Fig. 6. Raman spectra of the interlayer in the samples with 15 and 25 wt% loading of GAIN. (a) Average Raman spectra of the interlayers in LT (1150 °C) with 15 (red-line) and 25 (bue-line) wt.% loading of GAIN and at HT (1450 °C) with 15 (black-line) and 25 (green-line) wt.% GAIN. Comparison of the Raman spectra of interlayer of the samples: (b) Detail of the Raman spectra in the wavenumber ranging from 1200 to 1700 cm^{-1} comparing the 2D and D + D′ peaks. (c) Raman spectra in the Raman shift wavenumber range from 2500 to 3100 cm^{-1}. (A colour version of this figure can be viewed online.)

higher doping level possibly corresponding to higher concentration of hydrogen bonding.

3.4. Electrical transport properties

3.4.1. Hall measurement

A GAIN fibrous specimen was manually pressed and mounted onto the probe of PPMS. Resistance and Hall measurement data are shown in Fig. 7a and b. Due to a low linear density perpendicular to the rods, resistivity values do not represent the inherent properties of the GAIN fibers. Therefore, in Fig. 7a, the temperature dependence of the absolute values (resistance) is demonstrated. A well pronounced semiconducting behavior is apparent from Fig. 7a, reflecting the intrinsic contribution of a bulk-graphite-like
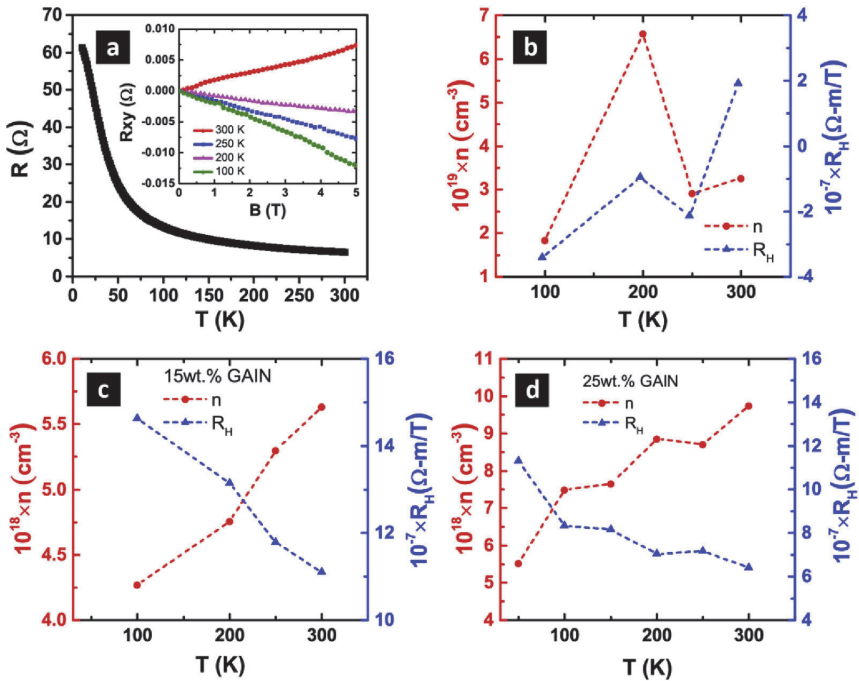

Fig. 7. Electrical transport and Hall measurement: (a) temperature dependency of DC resistance of GAIN fibers; Inset: Hall resistance as a function of magnetic field, Temperature dependency of Hall coefficient and carriers' density in (b) GAIN fibers, (c) alumina composite with 15 wt% GAIN, (d) alumina composite with 25 wt% GAIN. (A colour version of this figure can be viewed online.)

conduction [48] with a narrow band gap of 5.6 meV, which was calculated from the slope of the line of Arrhenius plot. In practice, polycrystalline graphene samples contain various types of disorder, such as point defects, contaminations and impurities that degrade the mobility in comparison to single-crystalline graphene. In section 3.3, the presence of such impurities was discussed. In fact, GBs in polycrystalline graphene largely impede carriers' transport, while they are often n-doped as compared to the nearby p-type graphene grains (due to contribution of surface adsorbates and contaminants). As a result, between the GB and graphene grains at small scales p-n junctions are formed that modulate the bandgap [49–51]. The power-law dependent semiconducting behavior and the absence of a temperature crossover indicates no transition in transport mechanism (e.g. semiconducting to metallic) and, therefore, no direct contribution of the Dirac point can be stated. This behavior is often correlated to the presence of structural impurities such as H bonding and substrate effect on the transport of CVD graphene. In the Hall resistance vs field plot (Fig. 7a, inset), no plateau is observed up to 5 T which indicates absence of Quantum Hall Effect (QHE) attributed to the three dimensional characteristics of the system under study, as well as the multilayer polycrystalline graphene. In fact, in three dimensions, the QHE is forbidden since the absence of quantum confinement spreads Landau levels into overlapping bands, which results in diminished quantization [52].

In Fig. 7b, the Hall coefficient visibly undergoes a sign inversion in the temperature interval of 250–280K and persists up to room temperature. The n-doping is this case is consistent with transport in hydrogenated graphene also reported for SiO_2 substrate [53]. The n-type behavior is a result of a decrease in the work function (WF) of hydrogenated graphene as compared to pristine graphene relative to the substrate's WF [53]. In contrast, p-doping is often correlated to physisorbed water on the surface of the graphene [53]. It was shown in Ref. [54] that wettability of CVD graphene is strongly dependent on the substrate while a decrease in water contact angle to $\leq 60°$, shifts the fermi level from n-to p-type. This phenomenon can describe the p-type transport at room temperature in GAIN fibers where liquid physisorbed water is present. On the other hand, the temperature interval of 250–280K where the Hall coefficient sign inversion occurs is around the freezing point of water. Granted that the physisorbed ice on graphene does not contribute to neither of short- or long-range scatterings and to charge donation [55], at temperatures lower than the freezing point, the intrinsic electron contribution to the transport is consistent with the theoretical and experimental models for hydrogenated/few layers of graphene (Fig. 7a and b) [53,56]. In addition, Song et al. demonstrated that the water between graphene layers at a distance of 4.5 Å n-dopes the graphene, while p-doping occurs when the distance is reduced to 4 Å [57].

The sign inversion observed for GAIN fillers is superseded by a constant p-type conduction across the temperature range in composites with 15 and 25 wt% GAIN in Al_2O_3 matrix, visible from the positive values of R_H in Fig. 7c, and d respectively. One plausible explanation could be the strong interaction of the α-alumina matrix with graphene, which induces p-doping in the presence of electron accepting impurities such as Fe^+ and point defects such as aluminum interstitials and oxygen vacancies. The phenomenon was reported for Few-Layer Graphene/Al_2O_3 [56] in which the mechanism of the strong interaction of the graphene with the matrix was justified by the opposite linear thermal expansion behavior of alumina and graphene during the cooling process of sintering causing residual stress acting upon them [56].

It is shown that optical phonons at the graphene/substrate interface of monolayer and bilayer graphene modulate the polarization of the transport. It is also shown that intervalley scattering (consistent with observed D peak in section 3.3, which require the
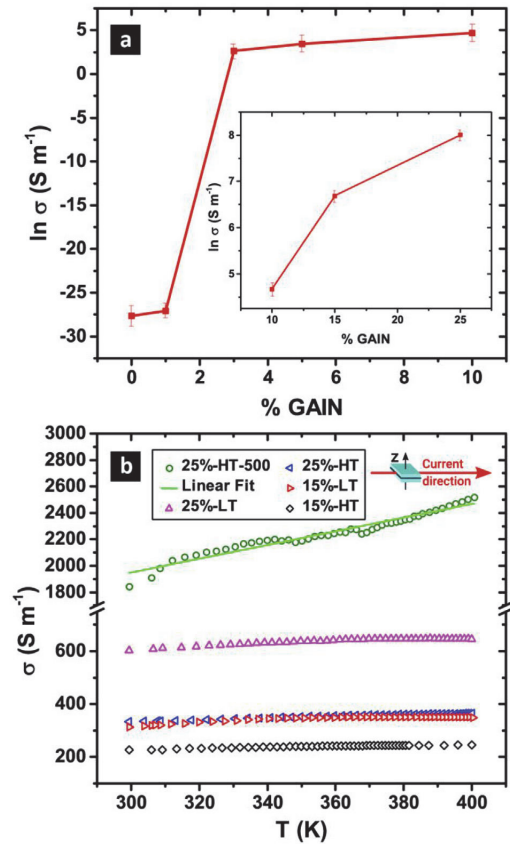

Fig. 8. (a) Electrical conductivity percolation threshold of composites of GAIN/Al_2O_3; inset: conductive fillers fraction effect on electrical conductivity, (b) DC in-plane electrical conductivity as a function of temperature. (A colour version of this figure can be viewed online.)

same scattering mechanism) and backscattering are the dominant transport mechanisms in polycrystalline graphene where GBs are present [51]. Having those in mind, increasing temperature enables surface phonon modes, which reduce mobility to a great extent. However, additional graphene layers in few layer polycrystalline graphene effectively screen the electric field of the substrate phonons. As a result, the mobility increases with temperature while the dominant mobility mechanism is Coulomb scattering [58–60]. Both optical and acoustic phonons can give rise to in-between states transitions in conduction band valleys. However, the energy scales of longitudinal acoustic phonons are too high to cause an effective scattering channel comparing to those posed by Coulomb and optical phonons. Therefore, their contribution can be neglected for multilayer graphene [61].

3.4.2. DC properties

Fig. 8 presents the dc electrical conductivity data of the layered structures obtained using two-probe in-plane measurement from room temperature to 400 K. As it is shown in Fig. 8a, estimated experimental percolation threshold for electrical conductivity is around 3 wt% of the fillers. This amount accounts for about 0.39 wt % of the total calculated carbon content detailed in Ref. [12]. In this

work, volume fraction dependence of the conductive fillers and their size effect on the percolation threshold is in agreement with the experimental and theoretical models [62]. Fig. 8a, inset, demonstrates that increasing the amount of the fillers drastically increases the electrical conductivity which at 25 wt% fillers' fraction (3.25 wt% carbon) the value reaches 3000 S m^{-1} in a bulk composite. This value is two folds of magnitude higher than the reported data for 3.7 vol% MWCNT/Al$_2$O$_3$ [63] but in-between the values reported for graphene nano pellets [64] and reduced graphene oxide [56]. It is also shown that electrical properties vary in the case of integrating thin graphene/alumina layers into monolithic alumina as compared to bulk composites, suggesting thickness dependency (Fig. 8b). Decrease in the layer thickness results in reduced conductivity. This effect can be explained by random orientation of the conductive fibers with slight preferred orientation perpendicular to the sintering pressure axis. Transport in the direction perpendicular to the pressure axis ($\sigma^\perp$) is considered to be through hopping mechanism. Whereas, in parallel direction ($\sigma^\parallel$), a more complex mechanism and significant contribution of grain boundaries (i.e. graphene grains discussed in section 3.4.1) is a more plausible interpretation [65]. Expectedly, multi layered graphene has a much higher in plane conductivity compared to c-axis transport perpendicular to the honeycomb basal planes. The $\sigma^\perp$:$\sigma^\parallel$ is also reported to be dependent on the fillers' content and increase by increasing their fraction [65,66]. This effect is more noticeable for the sample 25%-HT-500 with 500 μm interlayer thickness and 25 wt% GAIN. This anisotropy should not be confused with the macroscopic $\sigma^\parallel$:$\sigma^\perp$ of the layered structures, which is a measure of the in-plane conductivity of the samples vs. perpendicular conductivity of ~10^{-12} S m^{-1} corresponding to monolithic alumina. In the meantime, a more prominent increase in the conductivity of the same sample over temperature signals a better semiconducting behavior as compared to other samples with 100 μm interlayer thickness. That is to say, a more graphite like behavior of the thicker interlayer complies with increased 3rd dimensionality of the transport system due to accumulation of the stacked graphene coated fillers in the 500 μm hybrid interlayer. On the other hand, the sintering conditions influence the transport in the hybrid layer due to different grain growth rate. More specifically, as discussed in section 3.1, sintering at low temperature prohibits grain growth to a great extent and subsequently carrier transport is less disturbed based on two reasons; (I) samples sintered at higher temperature undergo significant grain growth which corresponds to large amounts of GBs defects. Thicker and defected GBs influence the carrier transport, which results in an increased resistivity. (II) Based on the theoretical evidence [31], a transition from γ to α phase in the Al$_2$O$_3$ fibers is presumed at sintering temperatures higher than 1200 °C. This transition results in linearly aligned granules of α-Al$_2$O$_3$ particles rather than fibrous structure, which greatly acts as a barrier for the carrier transport. The latter case, yet to be confirmed by the means of transfer electron microscopy in our structures. The modification of transport in LT samples is in spite of Raman spectroscopy results where for LT samples, increase in I(D)/I(G) and I(D')/I(G) together with observed D + D' peak was correlated to the sp^3 hybridization and C–H bonding.

4. Conclusions

In this work, a novel approach detailing the fabrication of the anisotropic functional multi-layered structures was implemented by ex-situ stacking alternative layers of α-alumina and hybrid interlayers, which consist of graphene-augmented γ-alumina nanofibers and α-alumina nanoparticles. A straight-forward bottom-up method based on catalyst-free hot-wall CVD process was employed to obtain the graphene-augmented nanofibers applied as

conductive fillers in the hybrid interlayer. The strategy to develop multilayered structures, introduces in-plane electrical conductivity in an otherwise insulating alumina preserving the mechanical properties of the bulk. Fully dense fine-grained materials were produced by SPS, employing both low (1150 °C) and high (1450 °C) temperature regimes. An excellent combination of high hardness (21−22 GPa) and modulus of elasticity (326−356 GPa) for a sample with 15 wt% of graphene augmented fillers in the hybrid layers obtained by means of the low and high temperature methods. However, in both sintering approaches, the presence of conductive fillers refines the microstructure by inhibition of grain growth not only in the hybrid interlayer but also with a slight influence on the monolithic alumina layers. Electrons were the dominant carriers in the graphene augmented nano-fillers, however in the composites, strong p-doping of alumina matrix resulted in p-type conduction. Transport in thinner interlayers shows a tendency towards semi-metallic behavior from RT to 400K. It was shown that increase in the fillers fraction results in increased conductivity from the percolation threshold at 0.39 wt% of the calculated carbon content in a full composite to in-plane ~600 and 1800 S m^{-1} in the 100 and 500 μm thick interlayers of the multilayered structures, respectively, employing a calculated 3.25 wt% of carbon content. In the same multilayered materials, a significant macroscopic anisotropy is achieved, where $\sigma^\perp$ (perpendicular to the hybrid interlayer and parallel to SPS pressure axis) equals to that of highly resistive monolithic alumina. A simple adjustment of the processing conditions, thickness and amount of graphene fillers, allows tuning the electrical response, which can help designing functional materials with potential application in areas such as EMI-shielding for electronics and aerospace.

CRediT authorship contribution statement

Ali Saffar Shamshirgar: Investigation, Methodology, Writing - original draft, Validation. **Rocio Estefania Rojas Hernández:** Investigation. **Girish C. Tewari:** Investigation. **Roman Ivanov:** Investigation, Validation. **Valdek Mikli:** Investigation. **Maarit Karppinen:** Data curation. **Irina Hussainova:** Conceptualization, Writing - review & editing, Supervision.

Declaration of competing interest

The authors declare that they have no known competing financial interests or personal relationships that could have appeared to influence the work reported in this paper.

Appendix A. Supplementary data

Supplementary data to this article can be found online at https://doi.org/10.1016/j.carbon.2020.06.038.

References

[1] U.G.K. Wegst, H. Bai, E. Saiz, A.P. Tomsia, R.O. Ritchie, Bioinspired structural materials, Nat. Mater. 14 (2015) 23–36, https://doi.org/10.1038/nmat4089.

[2] Z. Liu, M.A. Meyers, Z. Zhang, R.O. Ritchie, Functional gradients and heterogeneities in biological materials: design principles, functions, and bioinspired applications, Prog. Mater. Sci. 88 (2017) 467–498, https://doi.org/10.1016/j.pmatsci.2017.04.013.

[3] H.D. Espinosa, J.E. Rim, F. Barthelat, M.J. Buehler, Merger of structure and material in nacre and bone − perspectives on de novo biomimetic materials, Prog. Mater. Sci. 54 (2009) 1059–1100, https://doi.org/10.1016/j.pmatsci.2009.05.001.

[4] M. Zhou, H. Bi, T. Lin, X. Lü, F. Huang, J. Lin, Directional architecture of graphene/ceramic composites with improved thermal conduction for thermal applications, J. Mater. Chem. A. 2 (2014) 2187–2193, https://doi.org/10.1039/c3ta14325b.

[5] C. Molin, P. Neumeister, H. Neubert, S.E. Gebhardt, Multilayer Ceramics for Electrocaloric Cooling Applications, Energy Technol, 2018, pp. 1–11, https://doi.org/10.1002/ente.201800127.

[6] H. Luo, P. Xiao, W. Hong, Dielectric behavior of laminate-structure C_f/Si_3N_4 composites in X-band, Appl. Phys. Lett. 105 (2014) 172903, https://doi.org/10.1063/1.4900932.

[7] H. Porwal, P. Tatarko, S. Grasso, J. Khaliq, I. Dlouhý, M.J. Reece, Graphene reinforced alumina nano-composites, Carbon N. Y. 64 (2013) 359–369, https://doi.org/10.1016/j.carbon.2013.07.086.

[8] R. Ivanov, I. Hussainova, M. Aghayan, M. Drozdova, D. Pérez-Coll, M.A. Rodríguez, F. Rubio-Marcos, Graphene-encapsulated aluminium oxide nanofibers as a novel type of nanofillers for electroconductive ceramics, J. Eur. Ceram. Soc. 35 (2015) 4017–4021, https://doi.org/10.1016/j.jeurceramsoc.2015.06.011.

[9] A.K. Geim, K.S. Novoselov, The rise of graphene, Nat. Mater. 6 (2007) 183–191, https://doi.org/10.1038/nmat1849.

[10] A. Nieto, L. Huang, Y.H. Han, J.M. Schoenung, Sintering behavior of spark plasma sintered alumina with graphene nanoplatelet reinforcement, Ceram. Int. 41 (2015) 5926–5936, https://doi.org/10.1016/j.ceramint.2015.01.027.

[11] C. Ramírez, S.M. Vega-Diaz, A. Morelos-Gómez, F.M. Figueiredo, M. Terrones, M.I. Osendi, M. Belmonte, P. Miranzo, Synthesis of conducting graphene/Si3N4 composites by spark plasma sintering, Carbon N. Y. 57 (2013) 425–432, https://doi.org/10.1016/j.carbon.2013.02.015.

[12] M. Drozdova, I. Hussainova, D. Pérez-Coll, M. Aghayan, R. Ivanov, M.A.A. Rodríguez, A novel approach to electroconductive ceramics filled by graphene covered nanofibers, Mater. Des. 90 (2016) 291–298, https://doi.org/10.1016/j.matdes.2015.10.148.

[13] A. Centeno, V.G. Rocha, B. Alonso, A. Fernández, C.F. Gutierrez-Gonzalez, R. Torrecillas, A. Zurutuza, Graphene for tough and electroconductive alumina ceramics, J. Eur. Ceram. Soc. 33 (2013) 3201–3210, https://doi.org/10.1016/j.jeurceramsoc.2013.07.007.

[14] I. Hussainova, M. Drozdova, D. Pérez-Coll, F. Rubio-Marcos, I. Jasiuk, J.A.N.T. Soares, M.A. Rodríguez, Electroconductive composite of zirconia and hybrid graphene/alumina nanofibers, J. Eur. Ceram. Soc. 37 (2017) 3713–3719, https://doi.org/10.1016/j.jeurceramsoc.2016.12.033.

[15] Y. Kim, J. Lee, M.S. Yeom, J.W. Shin, H. Kim, Y. Cui, J.W. Kysar, J. Hone, Y. Jung, S. Jeon, S.M. Han, Strengthening effect of single-atomic-layer graphene in metal−graphene nanolayered composites, Nat. Commun. 4 (2013) 2114, https://doi.org/10.1038/ncomms3114.

[16] J. Ru, Y. Fan, W. Zhou, Z. Zhou, T. Wang, R. Liu, J. Yang, X. Lu, J. Wang, C. Ji, L. Wang, W. Jiang, Electrically conductive and mechanically strong graphene/mullite ceramic composites for high-performance electromagnetic interference shielding, ACS Appl. Mater. Interfaces 10 (2018) 39245–39256, https://doi.org/10.1021/acsami.8b12933.

[17] B. Luo, X. Wang, E. Tian, H. Gong, Q. Zhao, Z. Shen, Y. Xu, X. Xiao, L. Li, Dielectric enhancement in graphene/barium titanate nanocomposites, ACS Appl. Mater. Interfaces 8 (2016) 3340–3348, https://doi.org/10.1021/acsami.5b11231.

[18] M. Belmonte, A. Nistal, R. Cruz-Silva, A. Morelos-Gómez, M. Terrones, P. Miranzo, M.I. Osendi, Directional electrical transport in tough multifunctional layered ceramic/graphene composites, Adv. Electron. Mater. 1 (2015) 1500132, https://doi.org/10.1002/aelm.201500132.

[19] P. Miranzo, E. García, C. Ramírez, J. González-Julián, M. Belmonte, M. Isabel Osendi, Anisotropic thermal conductivity of silicon nitride ceramics containing carbon nanostructures, J. Eur. Ceram. Soc. 32 (2012) 1847–1854, https://doi.org/10.1016/j.jeurceramsoc.2012.01.026.

[20] P. Rutkowski, P. Klimczyk, L. Jaworska, L. Stobierski, A. Dubiel, Thermal properties of pressure sintered alumina−graphene composites, J. Therm. Anal. Calorim. 122 (2015) 105–114, https://doi.org/10.1007/s10973-015-4694-x.

[21] S.N. Stamatin, I. Hussainova, R. Ivanov, P.E. Colavita, Quantifying graphitic edge exposure in graphene-based materials and its role in oxygen reduction reactions, ACS Catal. 6 (2016) 5215–5221, https://doi.org/10.1021/acscatal.6b00945.

[22] I. Hussainova, R. Ivanov, S.S. Kale, I. Jasiuk, Tunneling—Percolation Behavior of Graphene-Encapsulated Whiskers as Electroconductive Fillers for Ceramics, Springer International Publishing, Cham, 2019, https://doi.org/10.1007/978-3-030-00868-0.

[23] M. Aghayan, I. Hussainova, M. Gasik, M. Kutuzov, M. Friman, Coupled thermal

[24] analysis of novel alumina nanofibers with ultrahigh aspect ratio, Thermochim. Acta 574 (2013) 140–144, https://doi.org/10.1016/j.tca.2013.10.010.

[24] Z. Shen, M. Johnsson, Z. Zhao, M. Nygren, Spark plasma sintering of alumina, J. Am. Ceram. Soc. 85 (2002) 1921–1927, https://doi.org/10.1111/j.1151-2916.2002.tb00381.x.

[25] A.S. Shamshirgar, R. Ivanov, I. Hussainova, Spark plasma sintering of layered γ-Al2O3/graphene reinforced nanocomposites, Proc. Est. Acad. Sci. 68 (2019) 140, https://doi.org/10.3176/proc.2019.2.04.

[26] M. Prakasam, D. Michau, O. Viraphong, M. Prakasam, D. Michau, O. Viraphong, A. Largeteau, Optimal Sintering Parameters for Al2O3 Optoceramics with High Transparency by Spark Plasma Sintering Optimal Sintering Parameters for Al2O3 Optoceramics with High Transparency by Spark Plasma Sintering, 2016, p. 6753, https://doi.org/10.17436753.2016.1149909.

[27] I. Hussainova, E. Hamed, I. Jasiuk, Nanoindentation testing and modeling of chromium-carbide-based composites, Mech. Compos. Mater. 46 (2011) 667–678, https://doi.org/10.1007/s11029-011-9180-3.

[28] H.P.R. Frederikse, W.R. Hosler, High temperature electrical conductivity of aluminum oxide. Mass Transp. Phenom. Ceram., Springer US, Boston, MA, 1975, pp. 233–252, https://doi.org/10.1007/978-1-4684-3150-6_16.

[29] J.F. Shackelford, Y.-H. Han, S. Kim, S.-H. Kwon, CRC Materials Science and Engineering Handbook, CRC Press, 2016, https://doi.org/10.1201/b18971.

[30] M. Tokita, Spark plasma sintering (SPS) method, systems, and applications, in: Handb. Adv. Ceram., Elsevier, 2013, pp. 1149–1177, https://doi.org/10.1016/B978-0-12-385469-8.00060-5.

[31] E. Yalamaç, A. Trapani, S. Akkurt, Sintering and microstructural investigation of gamma−alpha alumina powders, Eng. Sci. Technol. an Int. J. 17 (2014) 2–7, https://doi.org/10.1016/j.jestch.2014.02.001.

[32] S. Lamouri, M. Hamidouche, N. Bouaouadja, H. Belhouchet, V. Garnier, G. Fantozzi, J.F. Trelkat, Control of the γ-alumina to α-alumina phase transformation for an optimized alumina densification, Bol. La Soc. Esp. Ceram. y Vidr. 56 (2017) 47–54, https://doi.org/10.1016/j.bsecv.2016.10.001.

[33] M. Estili, Y. Sakka, Recent advances in understanding the reinforcing ability and mechanism of carbon nanotubes in ceramic matrix composites, Sci. Technol. Adv. Mater. 15 (2014), https://doi.org/10.1088/1468-6996/15/6/064902, 064902.

[34] J. Silvestre, N. Silvestre, J. de Brito, An overview on the improvement of mechanical properties of ceramics nanocomposites, J. Nanomater. 2015 (2015) 1–13, https://doi.org/10.1155/2015/106494.

[35] S. Ghanizadeh, S. Grasso, P. Ramanujam, B. Vaidhyanathan, J. Binner, P. Brown, J. Goldwasser, Improved transparency and hardness in α-alumina ceramics fabricated by high-pressure SPS of nanopowders, Ceram. Int. 43 (2017) 275–281, https://doi.org/10.1016/j.ceramint.2016.09.150.

[36] W.C. Oliver, G.M. Pharr, An improved technique for determining hardness and elastic modulus using load and displacement sensing indentation experiments, J. Mater. Res. 7 (1992) 1564–1583, https://doi.org/10.1557/JMR.1992.1564.

[37] A.C. Ferrari, D.M. Basko, Raman spectroscopy as a versatile tool for studying the properties of graphene, Nat. Nanotechnol. 8 (2013) 235–246, https://doi.org/10.1038/nnano.2013.46.

[38] A.A.K. King, B.R. Davies, N. Noorbehesht, P. Newman, T.L. Church, A.T. Harris, J.M. Razal, A.I. Minett, A new Raman method for the characterisation of graphene oxide and its derivatives, Sci. Rep. 6 (2016) 1–6, https://doi.org/10.1038/srep19491.

[39] A.C. Ferrari, Raman spectroscopy of graphene and graphite: disorder, electron-phonon coupling, doping and nonadiabatic effects, Solid State Commun. 143 (2007) 47–57, https://doi.org/10.1016/j.ssc.2007.03.052.

[40] S. Reich, C. Thomsen, Raman spectroscopy of graphite, Philos. Trans. R. Soc. London. Ser. A Math. Phys. Eng. Sci. 362 (2004) 2271–2288, https://doi.org/10.1098/rsta.2004.1454.

[41] P. Venezuela, M. Lazzeri, F. Mauri, Theory of double-resonant Raman spectra in graphene: intensity and line shape of defect-induced and two-phonon bands, Phys. Rev. B 84 (2011), https://doi.org/10.1103/PhysRevB.84.035433, 035433.

[42] A. Eckmann, A. Felten, A. Mishchenko, L. Britnell, R. Krupke, K.S. Novoselov, C. Casiraghi, Probing the nature of defects in graphene by Raman spectroscopy, Nano Lett. 12 (2012) 3925–3930, https://doi.org/10.1021/nl300901a.

[43] C. Casiraghi, S. Pisana, K.S. Novoselov, A.K. Geim, A.C. Ferrari, Raman fingerprint of charged impurities in graphene, Appl. Phys. Lett. 91 (2007) 12–14, https://doi.org/10.1063/1.2818692.

[44] S. Piscanec, M. Lazzeri, F. Mauri, A.C. Ferrari, Optical phonons of graphene and nanotubes, Eur. Phys. J. Spec. Top. 148 (2007) 159–170, https://doi.org/10.1140/epjst/e2007-00236-2.

[45] S. Ghosh, K. Ganesan, S.R. Polaki, T.R. Ravindran, N.G. Krishna, M. Kamruddin, A.K. Tyagi, Evolution and defect analysis of vertical graphene nanosheets, J. Raman Spectrosc. 45 (2014) 642–649, https://doi.org/10.1002/jrs.4530.

[46] G. Gao, D. Liu, S. Tang, C. Huang, M. He, Y. Guo, X. Sun, B. Gao, Heat-initiated chemical functionalization of graphene, Sci. Rep. 6 (2016) 20034, https://doi.org/10.1038/srep20034.

[47] J. Hwang, M. Kim, D. Campbell, H.A. Alsalman, J.Y. Kwak, S. Shivaraman, A.R. Woll, A.K. Singh, R.G. Hennig, S. Gorantla, M.H. Rümmeli, M.G. Spencer, van der Waals epitaxial growth of graphene on sapphire by chemical vapor deposition without a metal catalyst, ACS Nano 7 (2013) 385–395, https://doi.org/10.1021/nn305486x.

[48] P. Esquinazi, J. Krüger, J. Barzola-Quiquia, R. Schönemann, T. Herrmannsdörfer, N. García, On the low-field Hall coefficient of graphite,

AIP Adv. 4 (2014), https://doi.org/10.1063/1.4902099.

[49] O.V. Yazyev, Y.P. Chen, Polycrystalline graphene and other two-dimensional materials, Nat. Nanotechnol. 9 (2014) 755—767, https://doi.org/10.1038/nnano.2014.166.

[50] L. Tapasztó, P. Nemes-Incze, G. Dobrik, K. Jae Yoo, C. Hwang, L.P. Biró, Mapping the electronic properties of individual graphene grain boundaries, Appl. Phys. Lett. 100 (2012), https://doi.org/10.1063/1.3681375.

[51] J.C. Koepke, J.D. Wood, D. Estrada, Z.Y. Ong, K.T. He, E. Pop, J.W. Lyding, Atomic-scale evidence for potential barriers and strong carrier scattering at graphene grain boundaries: a scanning tunneling microscopy study, ACS Nano 7 (2013) 75—86, https://doi.org/10.1021/nn302064p.

[52] J. Yin, S. Slizovskiy, Y. Cao, S. Hu, Y. Yang, I. Lobanova, B.A. Piot, S.K. Son, S. Ozdemir, T. Taniguchi, K. Watanabe, K.S. Novoselov, F. Guinea, A.K. Geim, V. Fal'ko, A. Mishchenko, Dimensional reduction, quantum Hall effect and layer parity in graphite films, Nat. Phys. 15 (2019) 437—442, https://doi.org/10.1038/s41567-019-0427-6.

[53] B.R. Matis, J.S. Burgess, F.A. Bulat, A.L. Friedman, B.H. Houston, J.W. Baldwin, Surface doping and band gap tunability in hydrogenated graphene, ACS Nano 6 (2012) 17—22, https://doi.org/10.1021/nn2034555.

[54] G. Hong, Y. Han, T.M. Schutzius, Y. Wang, Y. Pan, M. Hu, J. Jie, C.S. Sharma, U. Müller, D. Poulikakos, On the mechanism of hydrophilicity of graphene, Nano Lett. 16 (2016) 4447—4453, https://doi.org/10.1021/acs.nanolett.6b01594.

[55] C. Jang, S. Adam, J.-H. Chen, E.D. Williams, S. Das Sarma, M.S. Fuhrer, Tuning the effective fine structure constant in graphene: opposing effects of dielectric screening on short- and long-range potential scattering, Phys. Rev. Lett. 101 (2008) 146805, https://doi.org/10.1103/PhysRevLett.101.146805.

[56] Y. Fan, W. Jiang, A. Kawasaki, Highly conductive few-layer graphene/Al 2O 3 nanocomposites with tunable charge carrier type, Adv. Funct. Mater. 22 (2012) 3882—3889, https://doi.org/10.1002/adfm.201200632.

[57] R. Song, W. Feng, C.A. Jimenez-Cruz, B. Wang, W. Jiang, Z. Wang, R. Zhou, Water film inside graphene nanosheets: electron transfer reversal between water and graphene via tight nano-confinement, RSC Adv. 5 (2015) 274—280, https://doi.org/10.1039/C4RA13736A.

[58] T. Ohta, A. Bostwick, J.L. McChesney, T. Seyller, K. Horn, E. Rotenberg, Inter-layer interaction and electronic screening in multilayer graphene investigated with angle-resolved photoemission spectroscopy, Phys. Rev. Lett. 98 (2007) 16—19, https://doi.org/10.1103/PhysRevLett.98.206802.

[59] W. Zhu, V. Perebeinos, M. Freitag, P. Avouris, Carrier scattering, mobilities, and electrostatic potential in monolayer, bilayer, and trilayer graphene, Phys. Rev. B 80 (2009) 235402, https://doi.org/10.1103/PhysRevB.80.235402.

[60] F. Guinea, Charge distribution and screening in layered graphene systems, Phys. Rev. B Condens. Matter 75 (2007) 1—7, https://doi.org/10.1103/PhysRevB.75.235433.

[61] E.H. Hwang, S. Das Sarma, Acoustic phonon scattering limited carrier mobility in two-dimensional extrinsic graphene, Phys. Rev. B Condens. Matter 77 (2008) 1—6, https://doi.org/10.1103/PhysRevB.77.115449.

[62] V.M. Samoilov, E.A. Danilov, A.V. Nikolaeva, D.V. Ponomareva, I.A. Porodzinskii, E.R. Razyapov, I.A. Sharonov, N.A. Yashtulov, Electrical conductivity of a carbon reinforced alumina resistive composite material based on synthetic graphite and graphene, Inorg. Mater. 54 (2018) 601—609, https://doi.org/10.1134/s0020168518060110.

[63] G. Yamamoto, M. Omori, T. Hashida, H. Kimura, A novel structure for carbon nanotube reinforced alumina composites with improved mechanical properties, Nanotechnology 19 (2008), https://doi.org/10.1088/0957-4484/19/31/315708.

[64] Q. Yuchang, W. Qinlong, L. Fa, Z. Wancheng, Temperature dependence of the electromagnetic properties of graphene nanosheet reinforced alumina ceramics in the X-band, J. Mater. Chem. C. 4 (2016) 4853—4862, https://doi.org/10.1039/C6TC01163B.

[65] C. Ramirez, F.M. Figueiredo, P. Miranzo, P. Poza, M.I. Osendi, Graphene nanoplatelet/silicon nitride composites with high electrical conductivity, Carbon N. Y. 50 (2012) 3607—3615, https://doi.org/10.1016/j.carbon.2012.03.031.

[66] S. Stankovich, D.A. Dikin, G.H.B. Dommett, K.M. Kohlhaas, E.J. Zimney, E.A. Stach, R.D. Piner, S.T. Nguyen, R.S. Ruoff, Graphene-based composite materials, Nature 442 (2006) 282—286, https://doi.org/10.1038/nature04969.
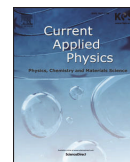
Paper II

Hussainova, I., **Saffar Shamshirgar, A.**, Ivanov, R., Volobujeva, O., Romanov, A. E., & Gasik, M. (2020). Directional conductivity in layered alumina. Current Applied Physics, (October 2019). https://doi.org/10.1016/j.cap.2020.06.009

ELSEVIER

Directional conductivity in layered alumina

Irina Hussainova[a],[*], Ali Saffar Shamshirgar[a], Roman Ivanov[a], Olga Volobujeva[b],
Alexey E. Romanov[c], Michael Gasik[d]

[a] Department of Mechanical and Industrial Engineering, Tallinn University of Technology, Tallinn, Estonia
[b] Tallinn University of Technology, Department of Materials and Environmental Technology, Tallinn, Estonia
[c] ITMO University, St. Petersburg, Russia
[d] Department of Materials Science and Engineering, School of Chemical Technology, Aalto University Foundation, Espoo, Finland

ARTICLE INFO

ABSTRACT

Here we report a novel strategy to consolidate layered alumina demonstrating the directional electrical and thermal conductivity. The material was produced via incorporation of alumina nanofibers (20 ± 2 nm in diameter) decorated by several layers of graphene wrapped around longitudinal axes of the fibers. The graphenated fibers, obtained with the help of one-step catalyst-free CVD process, offered inhibition of grain growth combined with electrical conductivity to the sandwiched composites, which were consolidated by spark plasma sintering. Impact of the concentration of the fillers together with thickness of the conductive graphene-containing layer on thermal properties was studied. A graphene-containing interlayer with 50 μm thickness, sandwiched between two monolithic 10 mm layers of alumina shows ~30% enhancement in isotropic thermal conductivity of monolithic alumina.

1. Introduction

Functional gradients and controlled anisotropy in structures enable engineering of mechanically reliable materials with a directional response. Directional functionalities are of increasing interest not only for aerospace and bio-medical applications [1,2] but also for military/defense and environmental purposes including but not limited to electrostatic charge dissipation, thermal and electromagnetic shielding/absorbing elements [3,4].

Among various choices of components, light-weight materials are of tremendous importance for automotive, aviation/space, robotics and many other applications. One of the materials of not weakening interest is alumina, which combines stability at elevated temperatures, high hardness and weight effectiveness. However, relatively low fracture toughness and insulating nature of this material significantly limits its usage for specific industrial needs.

In order to introduce new functionalities, powder metallurgy processing as a commonly used method helps to produce electroconductive alumina ceramics benefiting from the addition of graphene platelets or graphene oxide [5]. However, dispersion of the fillers is not a trivial task up to now. To ensure a homogeneous distribution of the additives, graphene augmented inorganic nanofibers (GAIN) were recently used to stipulate on combined benefits of conductivity, grain refinement and

reinforcement [6,7]. Owing to the extraordinary aspect ratio of the fibers, large surface area and low percolation threshold [6], GAIN offers a highly conductive ceramic with as low carbon content as 0.3 wt% without any deterioration of mechanical properties [8] but significant electrical properties. As for alumina, an increase in electroconductivity of 13 order of magnitude has been reported in Ref. [7]. The low percolation threshold can be attributed to a successfully performed distribution of the fillers in the matrix and a high aspect ratio of the fibers. Above the percolation, the conductivity of the composites of Al_2O_3/GAIN sharply increases with the fraction of the graphene covered nanofibers. Moreover, a carrier change from p-type in materials with a low graphene content to n-type when graphene content increases is demonstrated elsewhere [9] allowing, in principle, tailoring the properties of the final product.

The stacked basal plane structure of graphite gives rise to anisotropic properties. In fact, the hexagonal sp^2 hybridized rings of carbon in the basal planes contribute to an in-plane thermal conduction of ~2000 W/mK. The versatile carbon family offers a wide range of values from 0.01 W/mK in amorphous carbon to above 3000 W/mK in CNT and graphene [10]. In an attempt to employ these tremendous properties into the matrix of otherwise insulators such as alumina, several methods and strategies to improve thermal conductivity were recently reported. In fact, together with enhanced electrical conductivity, the

---

I. Hussainova, et al.

Table 1
Index of samples.

Sample name	α-Al$_2$O$_3$	GAIN	Interlayer thickness	Relative Density
	[wt.%]	[wt.%]	[μm]	
Alumina	–	–	–	99.72
G15-50	85	15	50	99.85
G15-100	85	15	100	99.77
G15-150	85	15	150	99.87
G15-200	85	15	200	99.95
G25-50	75	25	50	99.30
G25-100	75	25	100	99.92
G25-150	75	25	150	99.82
G25-200	75	25	200	99.90
G05	95	5	–	98.88
G15	85	15	–	93.23
G25	75	25	–	89.35

thermal properties are also influenced by graphene related additives. Additional functionality, i.e. directional conductivity and/or anisotropy, may considerably contribute into the field of ceramics with tunable properties. Layered structures of Si$_3$N$_4$/GNP (graphene nanoplatelets) have been developed by Mirzano et al. [11] with the help of cost-effective and scalable approach of usage of graphene oxide films as the graphene precursor. The widely used graphene nanoplatelets (GNP) added into alumina matrix conditioned an anisotropy in thermal diffusivity in composites with 16.5 vol% GNPs [12] and a reduction in thermal conductivity [13]. Addition of GPLs in the matrix of Al$_2$O$_3$ increased its in-plane thermal conduction by ~44% at 600 °C [14]. In general while employing CNTs some reports show slight improvement over a low fraction of the fillers [15,16], others report a decline in the thermal properties [13]. Supposing that the highly defective graphene sheets may act as thermal barriers [17], a reduced thermal conductivity can be expected. In addition to that, a large quantity of electrically conductive graphene additives can contribute to electronic thermal transport of ceramic matrix structure leading to a double mode excitation.

In the current work, highly innovative hybrid fillers, which represent the ceramic/carbon fibers produced by inexpensive and scalable procedure of one-step catalyst-free chemical vapor deposition (CVD) of carbon onto the surface of highly aligned metal oxide ceramic nanofibers are exploited to prepare multilayered alumina/graphene composites of high anisotropy and tunable conductivity. Furthermore, thermal response of the layered alumina/GAIN structures is studied to reveal the influence of graphene content and thickness of the conductive layer on the thermal properties of the bulk. Here we report a novel strategy to consolidate highly anisotropic multi-gradient alumina of excellent electrical conductivity in one direction and insulation in another. Functionally graded and/or layered architectures are known to benefit in strength and toughness also contributing to the added functionality in terms of anisotropic electrical and thermal conductivity. Our approach exploits the advantage of the remarkable conductivity of graphene as well as inhibition of the grains growth in the structures filled by carbon additives. In order to investigate the effect of graphene augmented alumina nanofibers on thermal properties of alpha alumina, both full nanocomposites and sandwiched structures comprised of composite interlayers (GAIN/Al$_2$O$_3$) and monolithic Al$_2$O$_3$ outer layers were exploited. To avoid carbon degradation, a short dwell time and a reduced sintering temperature are both of critical importance. One of the techniques available to solve the problem of a long process duration is using spark plasma sintering (SPS) approach, which was successfully applied in the current work.

2. Experimental

2.1. Preparation of the structures

Commercially available α-alumina nano-powder with an average particle size of 150 nm (TM-DAR, Taimei, Japan) was used as the matrix material and monolithic alumina layers in a sandwiched structure. Few layers of graphene encapsulated alumina nanofibers (GAIN) were produced with the help of chemical vapor deposition (CVD) method, described in detail elsewhere [6,18] and used as nanofillers. Two green 20 mm diameter cylindrical bodies were prepared using α-alumina
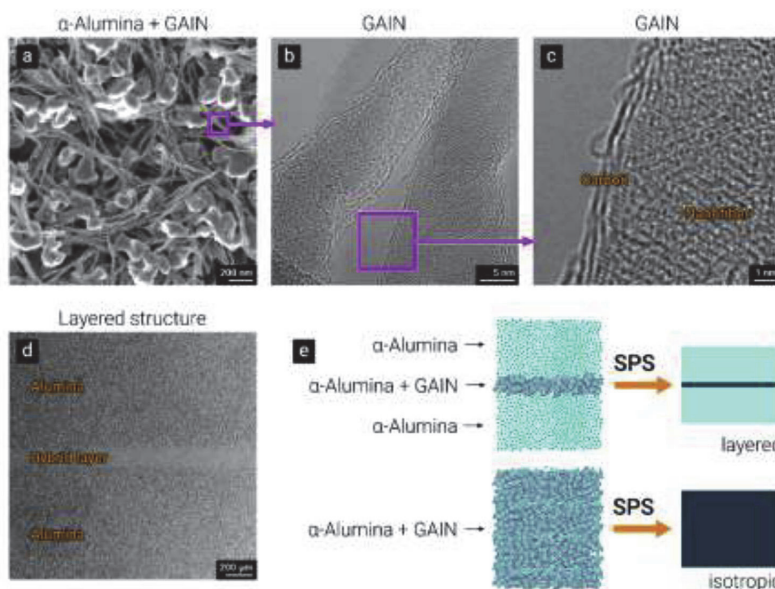

Fig. 1. (a) SEM micrograph of mixture of GAIN and alumina; (b, c) TEM micrographs of GAIN fibers; (d) SEM micrograph of layered structure; and (e) schematic of the test materials.
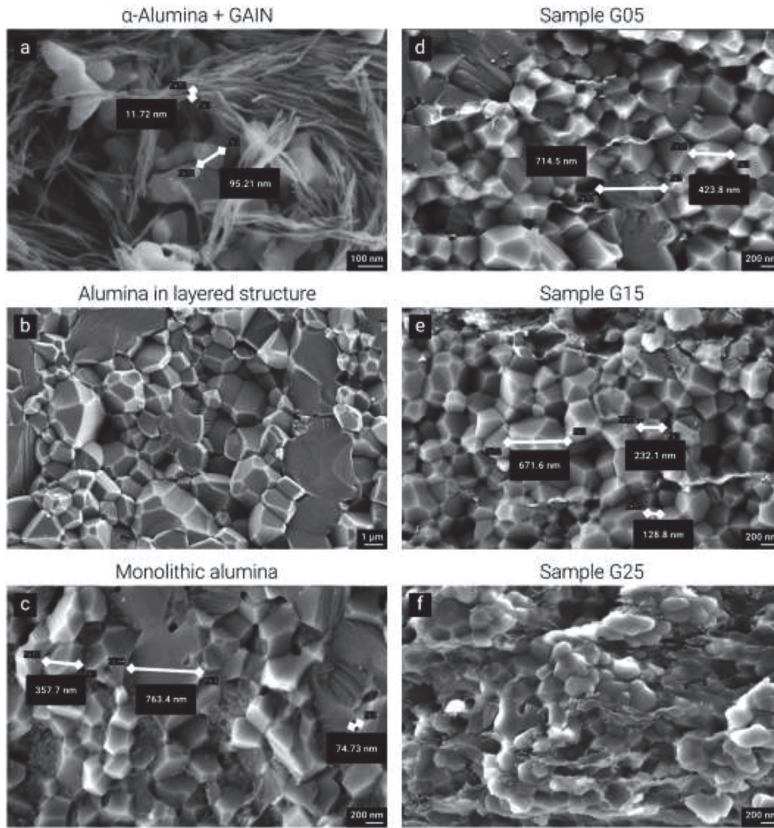
I. Hussainova, et al.

Fig. 2. SEM micrographs of (a) mixture of GAIN and alumina before sintering (dried); (b) grain structure of monolithic alumina part of layered structure after SPS; (c) monolithic alumina; and composites with (d) 5 wt% GAIN, (e) 15 wt% GAIN, and (f) 25 wt% GAIN.
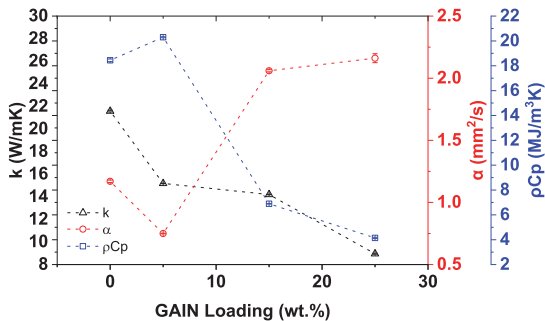

Fig. 3. Thermal conductivity (k), diffusivity (α), and volumetric heat capacity (ρCp) as a function of GAIN fillers' fraction.

nano-powder under 5 MPa of pressure to be used as the bottom and top punches of the sandwiched structure. Separately, for the interlayer, the fibers of about 40 mm in length and average single fiber diameter of about 20 nm were grinded in a mortar, weighted and mixed with α-alumina corresponding to 5, 15 and 25 wt% of GAIN in α-alumina. With addition of ethanol the mixture was ball milled using zirconia balls of 0.3 mm for 12 h. Later, the solution was filtered through the spark plasma sintering (SPS) mold. Two layers of monolithic alumina were added on the sides. The molds were closed by graphite papers for

sintering in FCT System GmbH SPS furnace at 1150 °C and a pressure of 75 MPa in a vacuum. Indexes of samples are listed in Table 1. A mixture of alumina nanoparticles and as-prepared GAIN fibers is shown in Fig. 1a. TEM micrographs display few-layered graphene augmented the alumina nanofibers, Fig. 1b and c. The produced structures are demonstrated in Fig. 1d and e. The Raman spectra of the GAINs have been thoroughly studied in Refs. [6,18] proving presence of several layers of defected graphene rolled around the core substrate.

2.2. Characterization

The morphological study of the obtained structures was performed by scanning electron microscope (HR-SEM Zeiss Merlin, Germany) equipped with an energy dispersive X-ray spectrometer (Bruker EDX-XFlash6/30 detector) with operating voltage of 5 kV. Density of the structures was measured using the Archimedes method with distilled water as an immersion media. The rule of mixtures using the manufacturers' density specification for alumina powder (3.96 g cm^{-3}), alumina fibers (3.65 g cm^{-3}) and published density value for graphene (2.2 g cm^{-3}) was used to calculate the relative densities. To characterize thermal conductivity, specific heat capacity, and diffusivity of the samples, transient plane source (TPS) method was employed by the means of HotDisk 2500S using 5465 Kapton sensor with 3.2 mm diameter in a double-sided arrangement to maximize the measurement accuracy. In this method, the sensor was placed in between two identical samples for isotropic heat dissipation. A four-probe dc electrical
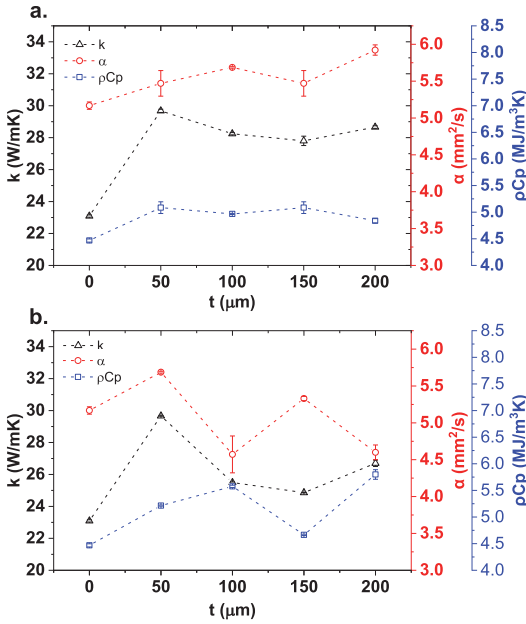
Fig. 4. Thermal conductivity (k), diffusivity (α), and volumetric heat capacity (ρCp) of sandwiched structures having interlayer thicknesses of 0–200 μm and GAIN fillers' fractions of (a) 15 wt%, and (b) 25 wt%.

conductivity method was used to measure electrical properties of the structures.

3. Results and discussion

3.1. Microstructure

Dispersion of the GAIN fibers in the matrix of alumina has led to a homogenous distribution despite some agglomeration of the nanofibers at high concentration, as seen in Fig. 2a for the mixture containing 25 wt% GAIN. The presence of conductive GAIN fillers leads to a microstructure refinement due to enhancement in grain boundary migration by pinning of matrix grains, which provides a more efficient sintering process [3,19], (see Fig. 2). Fig. 2d–f evidences that the presence of conductive fillers significantly impedes the grain growth and the effect is becoming more pronounced with an increase in the fraction of the fillers. In principle, the consequence of localized heating at the grain boundaries has been reported in Ref. [3]. Microstructure of the

composite layers (Al_2O_3/GAIN) reveals an anisotropic alignment of the fillers perpendicular to the pressure axis. Similar observation were reported for GPL/Al_2O_3 [14] and CNT/Si_3N_4 [11] composites sintered by SPS. Well-recognizable hexagonal alumina grains and the fillers positioned along the facets of the grains parallel to the pressure axis are demonstrated in Fig. 2. Moreover, a transition from inter-granular crack propagation in monolithic Al_2O_3 to a combination of intergranular and trans-granular fracture in the filled materials is observable in Fig. 2c–f and is in agreement with a previous report. In the monolithic alumina, the presence of both inter-granular and intra-granular porosity is notable as oppose to a preferably inter-granular porosity in the GAIN added materials, Fig. 2e and f. Comparing the micrographs of Fig. 2b and c, it is evident that presence of a thin interlayer of the GAIN/Alumina nanocomposite slightly refines the microstructure in the surrounding monolithic alumina layers. This phenomenon can be explained by the change in local joule heating in the SPS mold as a result of a parallel to the pressure axis conductive plane, which provides an additional conductive path for the electrical discharge during the SPS process.

3.2. Thermal properties

The isotropic double-sided thermal measurement data of the samples as a function of GAIN loading in the composites G05, G15, and G25 is presented in Fig. 3. A data point corresponding to the monolithic alumina is presented for comparison (GAIN loading = 0). An increase in the GAIN content results in a decrease in the thermal transport presumably by significant reduction in the $k^{\perp}$ and $\alpha^{\perp}$ up to 5 wt% GAIN as it is similarly reported for SPSed GNP/SiC [20]. Interestingly, increasing GAIN loading later augments the $\alpha^{\perp||}$ which can be explained by the opposite response of the ρC_p comparing to α to increasing carbon content. Thermal excitation is generally damped by phonons and free electrons. For 5 wt% addition of GAIN corresponding to ~0.45 wt% carbon content, the electrical percolation threshold is achieved, therefore correlation of a small increase in ρC_p due to a dual mode excitation is a plausible explanation. By increasing fillers loading, however, ρC_p sharply decreases. This behavior seems intuitive since for graphene and graphite, phonon scattering dominates the specific heat [12,21]. At room temperature, the specific heat of graphite is higher than that of diamond due to higher density of states provided by the weak couplings of the basal planes. Similarly, in graphene, acoustic modes: out of plane mode (ZA), in-plane transverse mode (TA), and in-plane longitudinal (LA), become thermally excited modulating the specific heat. However, the relative contribution of these modes to heat transport can vary depending on their dispersion. More specifically, once in contact with a substrate (i.e. graphene on Al_2O_3 in GAIN), the acoustic modes can undergo an altered dispersion and become partially suppressed; which would reduce the specific heat [12,22]. In fact, k in this case entirely follows the relationship k = $\rho C_p \alpha$. The phenomenon is suggested
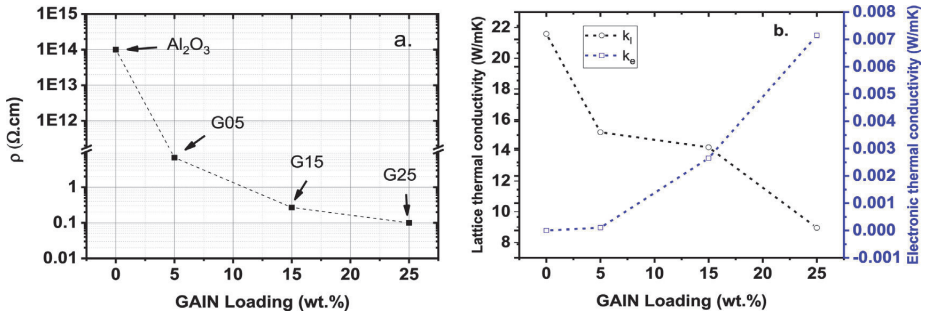

Fig. 5. Contribution of electrical properties as a function of GAIN loading to the thermal transport using (a) resistivity data, and (b) calculated electronic and lattice thermal conductivity at room temperature.

theoretically for graphene supported on SiO_2 in which substrate coupling is shown to cause damping of the flexural acoustic phonons reducing thermal conductivity [23]. Despite the different behavior of the specific heat, a decrease in k with an increase in the fillers content is in agreement with studies for MWCNT/Alumina [24] and GPL/Alumina [14]. In fact, it is well established that SPS of graphene/ceramics composites leads to anisotropic alignment of graphene component perpendicular to the pressure axis [14]. As a result, the sintered structures augment thermal conductivity perpendicular to the pressure axis. This is while parallel to the SPS axis, a significant deterioration of thermal conductivity occurs mostly due to weak thermal properties of graphene perpendicular to the basal plane. As a result, increasing the total graphene fraction increases this anisotropy, and expands the $k^\perp/k^{||}$. The effect is well pronounced for full composites where addition of GAIN deteriorates $k^{\perp||}$. Correspondingly, for 25 wt% GAIN a 60% decline in $k^{\perp||}$ occurs comparing to that of monolithic alumina. However, in the layered structures, the thin thickness of the conductive interlayers help to circumvent this effect, keeping the thermal properties of the bulk nearly unchanged.

The isotropic double-sided thermal measurement data of the samples as a function of interlayer thickness is presented in Fig. 4a and b for sandwiched structures having interlayers reinforced with 15 wt%, and 25 wt% GAIN respectively. In each case, one data point (at t = 0) corresponding to monolithic Al_2O_3 is presented for comparison. The presence of GAIN fillers slightly enhance the $k^{\perp||}$ independent of change in fillers' fraction. This enhancement is more prominent at 50 μm interlayer thickness. Otherwise, increase in the interlayer thickness does not significantly change the $k^{\perp||}$ of the bulk.

3.3. Electrical properties

A four-probe volumetric resistivity measurement was used to characterize the electrical properties of the composites as a function of GAIN loading (Fig. 5a). Having established in previous reports that the electrical percolation threshold is ~3 wt% for the fillers corresponding to 0.3 wt% of carbon, the resistivity drops significantly comparing the monolithic alumina sample to the composites with 5 wt% of GAIN. The resistivity decreases further by increasing the fillers fraction reaching a minimum value of 0.1 Ωcm at 25 wt% GAIN. In order to investigate the contribution of the electronic transport to thermal transport, the Wiedemann–Franz law was used to calculate lattice (k_l) and electronic thermal transports (k_e) contribution to the total transport (k). The k_e was calculated using the equation $k_e = L \times \sigma \times T$ in which L is the Lorenz constant equal to 2.44×10^{-8} V^2/K^2, σ is the electrical conductivity and T is the room temperature. The corresponding values to the composites with different fraction of GAIN were calculated and subtracted from the total transport to obtain lattice thermal conductivity values using equation $k = k_l + k_e$ and both are plotted in Fig. 5b. The k_e increases after the point of percolation, however, the contribution of k_e to the total transport remains very small by increasing the fillers fraction. The de-coupling of electrical/thermal transport indicates that the phonon scattering is the dominant thermal transport mechanism in the fabricated nanocomposites.

4. Conclusions

Composites of α-alumina matrix reinforced with different fractions of graphene augmented alumina nanofibers (GAIN) as well as a set of sandwich structures consisting of alternating layers of pure alumina and the GAIN/alumina composite of various thickness were produced using spark plasma sintering at 1150 °C under a pressure of 75 MPa in a vacuum. An introduction of the GAIN additives results in substantial decrease in grain size in the hybrid layer as compared to pure alumina. Thermal conductivity decreases by increasing the fillers fraction despite an increase in diffusivity due to simultaneous decline of specific heat denoted to graphene substrate interaction. In the layered structure, the

materials with 50 μm interlayer thickness demonstrate the most profound enhancement (~30%) in thermal conductivity as compared to the monolithic alumina. The fraction of the graphene augmented nanofibers does not reveal a significant contribution to the thermal properties. The electronic contribution of the thermal transport was defined to be negligible assuming that the main mechanism for thermal transport is phonon scattering. The developed layered structures enable engineering of lightweight electronics enclosures where anisotropic properties can enable multifunctionality such as electrostatic charge dissipation and electromagnetic interference shielding, while thermal conductivity is a critical concern.

Declaration of competing interest

The authors declare that they have no known competing financial interests or personal relationships that could have appeared to influence the work reported in this paper.

References

[1] A. Centeno, V.G. Rocha, B. Alonso, A. Fernández, C.F. Gutierrez-Gonzalez, R. Torrecillas, A. Zurutuza, Graphene for tough and electroconductive alumina ceramics, J. Eur. Ceram. Soc. 33 (2013) 3201–3210, https://doi.org/10.1016/j.jeurceramsoc.2013.07.007.

[2] J. Kazantseva, R. Ivanov, M. Gasik, T. Neuman, I. Hussainova, Graphene-augmented nanofiber scaffolds demonstrate new features in cells behaviour, Sci. Rep. 6 (2016) 30150, https://doi.org/10.1038/srep30150.

[3] I. Ahmad, B. Yazdani, Y. Zhu, Recent advances on carbon nanotubes and graphene reinforced ceramics nanocomposites, Nanomaterials 5 (2015) 90–114, https://doi.org/10.3390/nano5010090.

[4] V. Dhand, K.Y. Rhee, H. Ju Kim, D. Ho Jung, A comprehensive review of graphene nanocomposites: research status and trends, J. Nanomater. 2013 (2013) 1–14, https://doi.org/10.1155/2013/763953.

[5] X. Liu, Y.-C. Fan, J.-L. Li, L.-J. Wang, W. Jiang, Preparation and mechanical properties of graphene nanosheet reinforced alumina composites, Adv. Eng. Mater. 17 (2015) 28–35, https://doi.org/10.1002/adem.201400231.

[6] R. Ivanov, I. Hussainova, M. Aghayan, M. Drozdova, D. Pérez-Coll, M.A. Rodríguez, F. Rubio-Marcos, Graphene-encapsulated aluminium oxide nanofibers as a novel type of nanofillers for electroconductive ceramics, J. Eur. Ceram. Soc. 35 (2015) 4017–4021, https://doi.org/10.1016/j.jeurceramsoc.2015.06.011.

[7] M. Drozdova, I. Hussainova, D. Pérez-Coll, M. Aghayan, R. Ivanov, M.A.A. Rodríguez, A novel approach to electroconductive ceramics filled by graphene covered nanofibers, Mater. Des. 90 (2016) 291–298, https://doi.org/10.1016/j.matdes.2015.10.148.

[8] I. Hussainova, M. Drozdova, D. Pérez-Coll, F. Rubio-Marcos, I. Jasiuk, J.A.N.T. Soares, M.A. Rodríguez, Electroconductive composite of zirconia and hybrid graphene/alumina nanofibers, J. Eur. Ceram. Soc. 37 (2017) 3713–3719, https://doi.org/10.1016/j.jeurceramsoc.2016.12.033.

[9] Y. Fan, W. Jiang, A. Kawasaki, Highly conductive few-layer graphene/Al 2O 3 nanocomposites with tunable charge carrier type, Adv. Funct. Mater. 22 (2012) 3882–3889, https://doi.org/10.1002/adfm.201200632.

[10] A.A. Balandin, Thermal properties of graphene and nanostructured carbon materials, Nat. Mater. 10 (2011) 569–581, https://doi.org/10.1038/nmat3064.

[11] P. Miranzo, E. García, C. Ramírez, J. González-Julián, M. Belmonte, M. Isabel Osendi, Anisotropic thermal conductivity of silicon nitride ceramics containing carbon nanostructures, J. Eur. Ceram. Soc. 32 (2012) 1847–1854, https://doi.org/10.1016/j.jeurceramsoc.2012.01.026.

[12] E. Pop, V. Varshney, A.K. Roy, Thermal properties of graphene: fundamentals and applications, MRS Bull. 37 (2012) 1273–1281, https://doi.org/10.1557/mrs.2012.203.

[13] G.-D. Zhan, A.K. Mukherjee, Carbon nanotube reinforced alumina-based ceramics with novel mechanical, electrical, and thermal properties, Int. J. Appl. Ceram. Technol. 1 (2005) 161–171, https://doi.org/10.1111/j.1744-7402.2004.tb00166.x.

[14] Y. Çelik, A. Çelik, E. Flahaut, E. Suvacı, Y. Çelik, A. Çelik, E. Flahaut, E. Suvacı, C. Ali, Anisotropic Mechanical and Functional Properties of Graphene-Based Alumina Matrix Nanocomposites to Cite This Version : HAL Id : Hal-01451008 Anisotropic Mechanical and Functional Properties of Graphene-Based Alumina Matrix Nanocomposites Yasemin C HAL Id, (2017).

[15] S.R. Bakshi, K. Balani, A. Agarwal, Thermal conductivity of plasma-sprayed aluminum oxide—multiwalled carbon nanotube composites, J. Am. Ceram. Soc. 91 (2008) 942–947, https://doi.org/10.1111/j.1551-2916.2007.02081.x.

[16] L. Kumari, T. Zhang, G. Du, W. Li, Q. Wang, A. Datye, K. Wu, Thermal properties of CNT-Alumina nanocomposites, Compos. Sci. Technol. 68 (2008) 2178–2183,

https://doi.org/10.1016/j.compscitech.2008.04.001.

[17] M. Landmann, E. Rauls, W.G. Schmidt, The electronic structure and optical response of rutile, anatase and brookite TiO 2, J. Phys. Condens. Matter 24 (2012) 195503, https://doi.org/10.1088/0953-8984/24/19/195503.

[18] R. Ivanov, V. Mikli, J. Kübarsepp, I. Hussainova, Direct CVD growth of multi-layered graphene closed shells around alumina nanofibers, Key Eng. Mater. 674 (2016) 77–80 https://doi.org/10.4028/www.scientific.net/kem.674.77.

[19] A.S. Shamshirgar, R. Ivanov, I. Hussainova, Spark plasma sintering of layered γ -Al 2 O 3/graphene reinforced nanocomposites, Proc. Est. Acad. Sci. 68 (2019) 140, https://doi.org/10.3176/proc.2019.2.04.

[20] B. Román-Manso, Y. Chevillotte, M.I. Osendi, M. Belmonte, P. Miranzo, Thermal conductivity of silicon carbide composites with highly oriented graphene nano-platelets, J. Eur. Ceram. Soc. 36 (2016) 3987–3993, https://doi.org/10.1016/j.jeurceramsoc.2016.06.016.

[21] J. Hone, Phonons and thermal properties of carbon nanotubes, n.d. Carbon Nanotub, Springer Berlin Heidelberg, Berlin, Heidelberg, 2001, pp. 273–286, , https://doi.org/10.1007/3-540-39947-X_11.

[22] D.L. Nika, A.A. Balandin, Two-dimensional phonon transport in graphene, J. Phys. Condens. Matter 24 (2012) 233203, https://doi.org/10.1088/0953-8984/24/23/233203.

[23] Z.-Y. Ong, E. Pop, Effect of substrate modes on thermal transport in supported graphene, Phys. Rev. B 84 (2011) 075471, , https://doi.org/10.1103/PhysRevB.84.075471.

[24] K. Ahmad, P. Wei, C. Wan, Thermal conductivities of alumina-based multiwall carbon nanotube ceramic composites, J. Mater. Sci. 49 (2014) 6048–6055, https://doi.org/10.1007/s10853-014-8327-8.

Paper III

Functionally Graded Tunable Microwave Absorber with Graphene-Augmented Alumina Nanofibers

Ali Saffar Shamshirgar, Rocio E. Rojas Hernández, Girish C. Tewari, José Francisco Fernández, Roman Ivanov, Maarit Karppinen, and Irina Hussainova*

Read Online

ACCESS | Metrics & More | Article Recommendations | Supporting Information

ABSTRACT: Graphene is currently attracting attention for radiation absorption particularly at gigahertz and terahertz frequencies. In this work, composites formed by graphene-augmented γ-Al$_2$O$_3$ nanofibers embedded into the α-Al$_2$O$_3$ matrix are tested for X-band absorption efficiency. Composites with 15 and 25 wt % of graphene fillers with shielding effectiveness (SE) of 38 and 45 dB, respectively, show a high reflection coefficient, while around the electrical percolation threshold ($\sim$1 wt %), an SE of 10 dB was achieved. Furthermore, based on the dielectric data obtained for varying fractions of graphene-/γ-Al$_2$O$_3$-added fillers, a functionally graded multilayer is constructed to maximize the device efficiency. The fabricated multilayer offers the highest absorption efficiency of 99.99% at $\sim$9.6 GHz and a full X-band absorption of >90% employing five lossy layers of 1−3−5−15 and 25 wt % of graphene/γ-Al$_2$O$_3$ fillers. The results prove a remarkable potential of the fillers and various multilayer designs for broad-band and frequency-specific microwave absorbers.

KEYWORDS: hybrid nanofibers, graphene, alumina, microwave absorption, impedance matching, multilayer structure
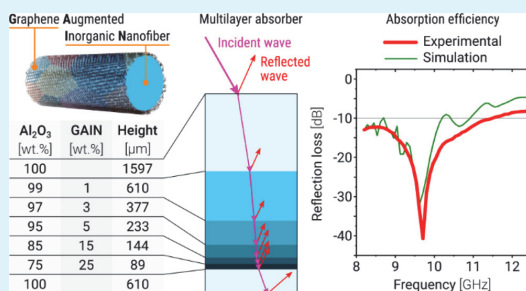
1. INTRODUCTION

Electromagnetic (EM) absorption is an important part of the design in stealth technology, telecommunication, and more widely in any application involving sensitive pieces of electronics operating within the range of a radiation source. As an example, in stealth technology, the radar-absorbing materials (RAMs) are employed for concealment of an object from the radar detection (lowering radar cross section) while used in electronic devices to shield sensitive precision components from interference. In addition, microwave absorbing materials (MAMs) are used for reducing the side lope radiation of antennas.[1] Therefore, with the technological advancements and progress in telecommunication networks such as 5G development, high-performance multifunctional materials with lightweight, low thickness, desirable thermal properties, suitable oxidation resistance, and wideband EM absorption are more needed than before.[2] Since electrical conductors such as metals undesirably reflect most of the radiations, alternatively, lossy dielectric composite materials are used to absorb the radiations by attenuating the incident waves through various mechanisms.[3] At microwave frequencies, due to short wavelengths, the tendency of the incident radiation to scattering makes the design of an ideal absorber more challenging. One of the established methods to attenuate microwave is to employ the phenomenon of multiple reflections through which a vast number of interfaces are

introduced into a dielectric host material such as polytetrafluoroethylene (PTFE) or ceramics in order to dissipate the EM incident by conversion to heat caused by internal electrical resistance (otherwise known as Joule heating).[3] Most polymer-based absorbers are lightweight and easy to manufacture. However, when thermomechanical properties and corrosion resistance are of concern, ceramic-based absorbers and various types of coatings are all better choices.[2,4] Among the choices for substrate and matrix, Al$_2$O$_3$ (alumina) is one of the most important materials in the microwave-integrated circuit industry and a well-known material for electronic packaging applications.[4,5] This is mainly due to its extremely high quality factor [QF $\sim$5 × 10^4 at 9 GHz for sintered polycrystalline alumina at room temperature (RT)], low permittivity ($\varepsilon_r \sim$ 10), relatively high thermal conductivity ($k \sim$ 30 W·m^{-1}·K^{-1}), fair chemical stability, and high melting point (2050 °C).[5] Correspondingly, as for the filler material, carbon fibers are excellent candidates due to their abundance and desirable corrosion resistance and their versatility as a doping substrate

A

Table 1. Index of the Samples

sample name	α-Al$_2$O$_3$ [wt %]	GAIN [wt %]	graphene[a] [wt %]	relative density	comments
Al$_2$O$_3$	100	0	0	99.99	reference
G01	99	1	0.12	99.16	homogeneous composite
G03	97	3	0.36	99.45	homogeneous composite
G05	95	5	0.6	98.98	homogeneous composite
G15	85	15	1.8	93.80	homogeneous composite
G25	75	25	3	89.50	homogeneous composite
FSM-89-1[b]	98.02	1.98	0.24	99.08	multilayer structure
FSM-89-2	97.75	2.25	0.27	99.02	multilayer structure
FSM-144-1[b]	96.95	3.04	0.36	98.92	multilayer structure
FSM-144-2	95.03	4.96	0.59	98.85	multilayer structure

[a]Calculated based on the measured 12 wt % carbon content of GAIN. [b]89 and 144 correspond to multilayer designs where the thickness of the first layer is 89 or 144 μm, respectively.

Table 2. Layer Arrangement in Multilayer Structures

layer name	α-Al$_2$O$_3$ [wt %]	GAIN [wt %]	FSM-89-1 thickness [μm]	FSM-89-2 thickness [μm]	FSM-144-1 thickness [μm]	FSM-144-2 thickness [μm]
h$_7$	100	0	1597	987	987	0
h$_6$	99	1	610	610	987	987
h$_5$	97	3	377	377	610	610
h$_4$	95	5	233	233	377	377
h$_3$	85	15	144	144	233	233
h$_2$	75	25	89	89	144	144
h$_1$	100	0	610	987	610	0

to host heavier atoms (such as bromine and iodine) for enhanced shielding of high-energy radiation and ferromagnetic particles for broad-band absorption and synergetic dielectric magnetic loss. On the other hand, shortly after the discovery of graphene, the prospect of designing high-performance radio frequency (RF) devices using graphene was subject to verification. Ever since, a significant amount of work has been done to enable the application of graphene-like materials, specifically for radar absorption at microwave and terahertz range.[1] Several studies have portrayed the applicability of graphene,[6] SWCNT,[7] and MWCNT.[8−10] Moreover, in various works, it has been shown that the absorption efficiency of graphene-added materials can be enhanced by designing hierarchical, sandwiched, and porous structures.[2] In these structures, the dissipation of the incoming radiation can be achieved through dielectric interactions such as electronic, ionic, orientational, and space-charge polarizations and magnetic interactions such as natural resonance and eddy current loss. The shielding performance of a microwave absorber is directly affected by the impedance difference between the free space and the surface of the absorber material and the attenuation ability of the absorber. One of the ways to achieve a low surface mismatch (to overcome the surface scattering) and an efficient penetration depth (to efficiently utilize the entire cross section of the absorber) is to design a geometric transition absorber, in which the effective absorber content gradually increases along the direction of the EM wave propagation in order to create an impedance-graded structure.[1]

In the present study, functionally graded multilayer structures are constructed using the ceramic matrix of α-Al$_2$O$_3$ filled by conductive graphene-augmented γ-Al$_2$O$_3$ nanofibers (GAIN). The thickness of the layers in the structure follows a gradient guided by Fibonacci numbers. The method of implementing the multilayers is established in the previous work of the authors.[11] Prior to assembling the

multilayer structures, a set of bulk composites with different fractions of the GAIN fillers are processed using spark plasma sintering (SPS). The X-band dielectric properties and shielding effectiveness (SE) of the bulks are determined using the transmission line method in a rectangular waveguide (WR-90). Reflection loss, dielectric properties, and EM interference shielding effectiveness (EMI SE) of the fabricated composites are measured and thoroughly discussed. The obtained data are employed in the impedance matching technique in order to design a structure with the surface impedance being closest to that of the free space. To achieve that, a multilayer structure consisting of six GAIN/α-Al$_2$O$_3$ lossy layers of specified thicknesses and filler contents are designed in order to create an impedance-graded structure for higher absorption performance. The absorption efficiency of the multilayer structure is characterized and discussed.

2. EXPERIMENTAL SECTION

2.1. Preparation of the Structures. Commercially available α-Al$_2$O$_3$ nanopowder with an average particle size of 100 nm (TM-DAR, Taimei, Japan) was used as the matrix material and the monolithic alumina layers in the multilayer structures. As the conductive nanofillers, few-layer polycrystalline graphene-encapsulating γ-Al$_2$O$_3$ nanofibers (GAIN), which were produced with the help of a catalyst-free one-step chemical vapor deposition (CVD) method—as described in detail elsewhere[12,13]—were used as a raw material. Prior to processing, GAIN fibers were ground in a mortar and sonicated in ethanol using a sonication rod (Hielscher UP400S) for 20 min with 20 W, 2 s on−1 s off, then dried at 70 °C for 12 h, and collected. The GAIN and α-Al$_2$O$_3$ nanopowder compositions corresponding to 1, 3, 5, 15, and 25 wt % of GAIN were mixed in ethanol and sonicated for 20 min at 20 W using an alternating regime of 2 s on−1 s off, followed by drying in a muffle furnace. The homogeneous powder compositions were collected, and compositions of 1, 3, 5, 15, and 25 wt % GAIN/α-Al$_2$O$_3$ corresponding to cylinders with 30 mm diameter and 5 mm thickness were sintered using the FCT System GmbH SPS furnace at 1150 °C under a pressure of 75
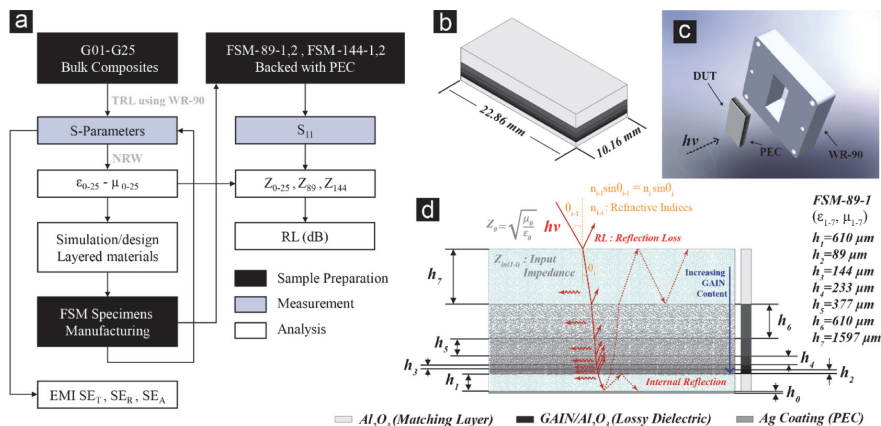
B

Figure 1. (a) Work logic diagram of the current study; (b) schematic of the multilayer specimen with WR-90 geometry consisting of FSM GAIN/Al_2O_3 dissipative layers, an Al_2O_3 matching layer, and a Ag backing plate (FSM-89-1); (c) illustration of the WR-90 sample holder for transmission line dielectric measurement; and (d) cross-sectional view of the multilayer structure with illustration of wave absorption, reflection, re-reflection, and transmission mechanisms guided by Snell's law and refractive indices.

MPa under vacuum. To prepare the multilayer structures, a solution-based process described in detail in ref 11 was employed. In brief, the mixture of GAIN/α-Al_2O_3 corresponding to 1−25 wt % GAIN and specified sintered thicknesses were weighed, mixed in chloroform separately, and sonicated for 20 min at 20 W using an alternating regime of 2 s on−1 s off. The Fibonacci sequenced multilayers (FSMs) were constructed layer by layer inside the SPS die using a vacuum filtration system. After drying for 12 h at 70 °C, the specimens were sintered at 1150 °C under a pressure of 75 MPa under vacuum. The consolidated specimens were ground to ∼3.2 mm thickness and were cut using an ATM BRILLANT 220 cutoff saw to rectangular waveguide 90 (WR-90) dimensions (22.86 × 10.16 mm). The final transverse geometries of all samples were in the ±100 μm range in accordance with ASTM D5568. The designations of the materials are listed in Table 1. The layer arrangement, thicknesses, and compositions of the multilayers are indexed in Table 2.

2.2. Characterization. Structure and chemical characterization of graphene-augmented nanofibers is detailed in ref 14. The carbon content of the CVD graphene-augmented alumina nanofibers was determined using a LECO CS 200 carbon−sulfur analyzer. The arithmetic mean of three measurements was used to calculate the corresponding carbon content of the composites. The ultimate size of the fibers after mixing was determined by the laser scattering method using a Mastersizer 3000, Malvern Panalytical, equipped with a λ = 632.8 nm He−Ne laser. Structural characterization was carried out by confocal Raman microscopy (Witec ALPHA 300RA) employing Nd:YAG laser excitation at 532 nm at RT and a 20× objective lens and a grating of 600 g/mm BLZ = 500 nm. The incident laser power was 0.17 mW. The optical diffraction resolution of the confocal microscope was limited to about 200 nm laterally. Raman spectral resolution of the system was down to 0.02 cm^{-1} under the best measurement conditions. A piezoelectric scanning table was used, which allowed three-dimensional displacements in steps of 3 nm, giving a very high spatial resolution for the confocal Raman microscopy. Each Raman image was taken for a 40 × 200 μm area consisting of ∼405 simple spectra of 1 s of integration time each. For the multilayer structure, eight Raman images were taken. The collected spectra were processed and analyzed using Witec Control Plus software 2.08. The Raman spectra were normalized by the maximum located at ∼1359 cm^{-1}. Lorentzian fitting has been carried out to determine the Raman peak position, intensity, area and full width at half-maximum (fwhm) and to decompose some of the peaks. For microstructural characterization of the fillers and bulks, a field emission scanning electron microscope (FEG-SEM Zeiss ULTRA-55,

Germany) equipped with an energy-dispersive X-ray spectrometer (BRUKER, Esprit 1.82 system, USA) with a voltage of up to 20 kV and magnifications up to 50 kX was used. Low-temperature transport properties (electrical resistivity and Hall coefficient) of the bulk composites were measured using a physical property measurement system (PPMS; Quantum design; equipped with 9 T magnetic field) with Hall bar configuration from 4 to 300 K. Prior to the measurement, in order to prepare the electrical probing areas, 50 nm Pt was deposited on the probe areas of the samples using a Cressington 308R coating system. Indium solder was utilized to place copper probes on the samples.

In accordance with ASTM D5568, the scattering parameters [$S_{11}(S_{22})$ and $S_{21}(S_{12})$] of the specimens were recorded at X-Band frequencies (8.2−12.4 GHz) using an N5222A PNA Microwave Network Analyzer from Keysight Technologies on the fundamental waveguide mode TE10 (transverse electric). The device was bundled with an N1500A Materials Measurement Suite from Keysight Technologies in which the complex permittivity and permeability are extracted using the Nicholson−Ross−Weir (NRW) method, and air gap correction is done using the frequency-dependent series capacitor algorithm. After extracting complex permittivity (ε) and permeability (μ) from NRW algorithm, the input impedance for each sample was calculated using eq 1, where Z_0 is the characteristic impedance of free space (377 Ω), Z_{in} is the input impedance of the absorber, f is the measured frequency, d is the thickness of the material, and c is the speed of light. Subsequently, reflection loss (RL) was calculated using eq 2. Employing the impedance matching technique, Fibonacci multilayers were designed, and simulated Z_{in} and RL values were compared to the experimental values. According to the transmission line theory, for multilayer structures with i number of layers, the incident impedance from the free space into the multilayer material is calculated using eq 3 where propagation constant is defined as $\gamma_i = j(2\pi f/c)\sqrt{\mu_{ri}\varepsilon_{ri}}$ and characteristic impedance of the ith layer is $\eta_i = \eta_0\sqrt{\mu_{ri}/\varepsilon_{ri}}$. To study the electric field (E-Field) distribution in the multilayers, Ansys HFSS is used to simulate the studied pattern, considering a partially filled rectangular waveguide with the TE10 mode incident. Skin depth (δ) of each composition is given by $\delta = \sqrt{2/\omega\mu\sigma}$ and refractive indices are calculated using $n = \sqrt{\mu_r\varepsilon_r}$ and presented in Figure S1. Since the modulus of permittivity obeys a logarithmic rule of mixture, the permittivity of GAIN fibers was calculated using eq 4. Similarly, although with a linear relation, dielectric loss tangent of GAIN was calculated using eq 5.[15,16]
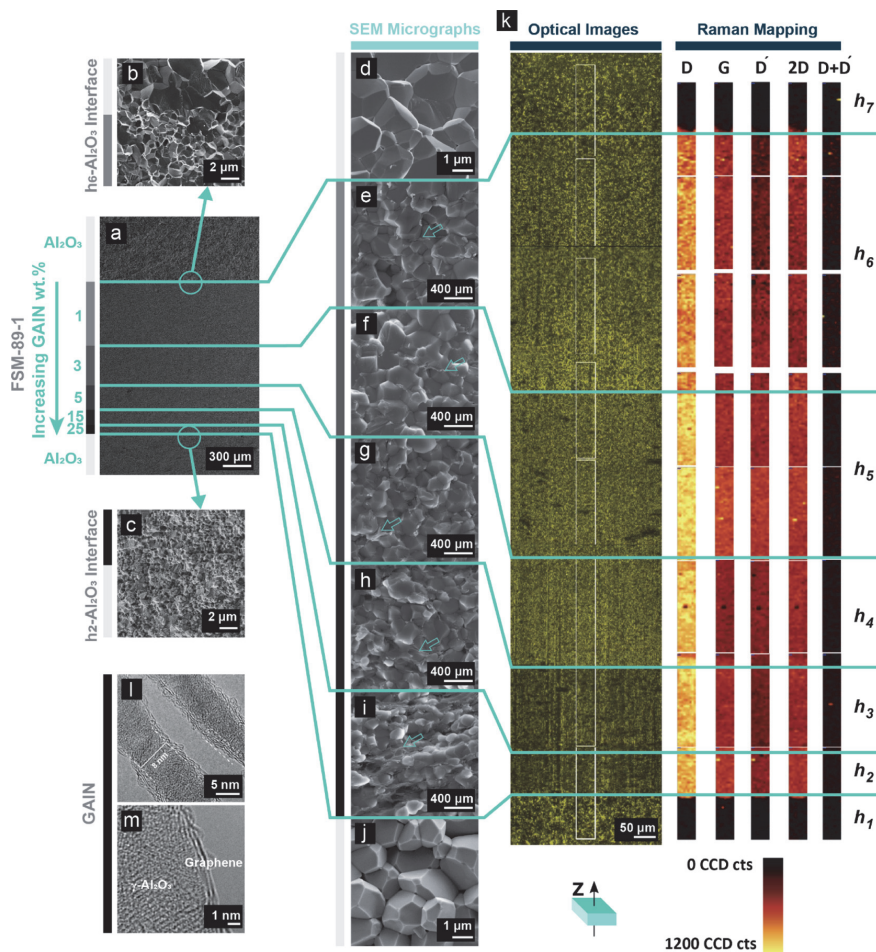
C

Figure 2. (a−j) SEM micrographs of the multilayer sample FSM-89-1; (k) Raman mapping of the multilayer FSM-89-1 demonstrating several graphene peak intensities; (l,m) TEM micrographs of GAIN hybrid used as nanofillers.

$$Z_{in} = Z_0 \sqrt{\frac{\mu_r}{\varepsilon_r}} \tanh\left[j\left(\frac{2\pi f d}{c} \sqrt{\mu_r \varepsilon_r} \right) \right] \tag{1}$$

$$RL(dB) = -20 \log \left| \frac{Z_{in} - Z_0}{Z_{in} + Z_0} \right| \tag{2}$$

$$Z_{in} = \eta_i \frac{[Z_{i-1} + \eta_i \tanh(\gamma_i d_i)]}{[\eta_i + Z_{i-1} \tanh(\gamma_i d_i)]} \tag{3}$$

$$|\varepsilon|_{GAIN} = \exp([\ln(|\varepsilon|_{Specimen}) - (1 - V)\ln(|\varepsilon|_{Alumina})]/V) \tag{4}$$

$$\tan \delta_{GAIN} = [\tan \delta_{Specimen} - (1 - V)\tan \delta_{Alumina}]/V \tag{5}$$

EMI SE was calculated using normalized transmitted power as a sum of contributions from shielding by reflection (SE_R), absorption (SE_A), and multiple reflections (SE_M), When SE_A is greater than 10 dB, SE_M can be neglected.[4] Therefore, the total shielding effectiveness (SET) is given by eq 6. For the samples with SE_A lower than 10 dB, a correction for multiple reflections was made using eq 7. The work logic diagram throughout the current work is depicted in Figure 1a. The geometry and dimensions of the samples under test are illustrated

in Figure 1b,c. A schematic of the FSM is shown in Figure 1d, in which the trajectory of the propagation of an example incident at angle θ is illustrated using Snell's law.

$$SE_T = SE_R + SE_A = 10 \log(1 - |S_{11}|^2) + 10 \log\left(\frac{|S_{21}|^2}{1 - |S_{11}|^2} \right) \tag{6}$$

$$SE_M = 20 \log|(1 - 10^{-SE_A/10})| \tag{7}$$

3. RESULTS AND DISCUSSION

3.1. Composition and Microstructure. In order to analyze the effect of GAIN fillers content and distribution throughout the multilayer structure, the multilayer designated as FSM-89-1 is selected and studied in this section by SEM and Raman spectroscopy. Moreover, since the microstructural features of the various layers in the multilayer (layers with 1− 25 wt % GAIN) are identical to the corresponding bulk composites (G01-G25), which have the same GAIN contents, the microstructural characterization findings can be considered
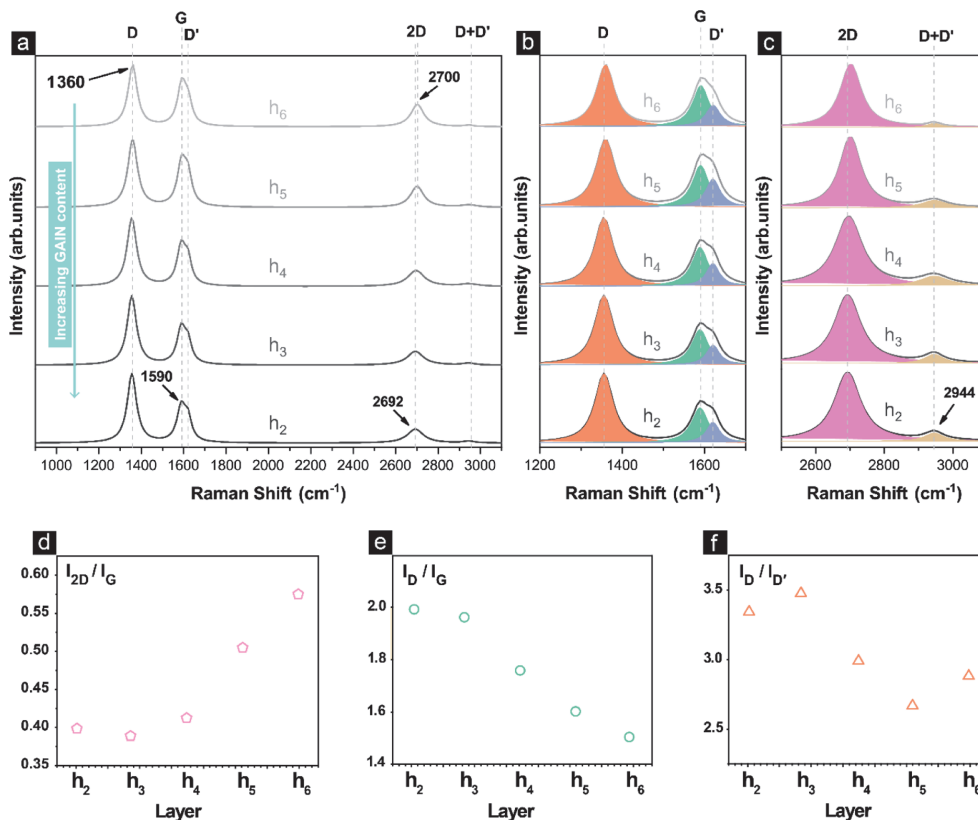
Figure 3. (a) Average Raman spectra of the interlayers in the sample FSM-89-1 with h_2 corresponding to the highest GAIN content (25 wt %) and h_6 to the lowest GAIN content (1 wt %). Deconvolution of the peaks providing detail on the (b) Raman spectra in the wavenumber ranging from 1200 to 1700 cm^{-1} and (c) Raman spectra in the Raman shift wavenumber range from 2500 to 3100 cm^{-1}. Comparison of the intensity ratios of (d) I_{2D}/I_G, (e) I_D/I_G, and (f) $I_D/I_{D'}$ in different regions of the sample FSM-89-1.

interchangeable for both bulk composites and the corresponding layers in the multilayer structure. The α-alumina nanopowder allows sintering at low temperature (1150 °C) with a notable grain growth (average grain size >3 μm). The addition of GAIN inhibited the grain growth and resulted in a fine microstructure in all bulk composites. The finest grains are determined in G25 with an average grain size of 100 nm, which is comparable to the powder precursor particle size (Figure 2a–j). However, at the selected sintering conditions, an increase in the fillers' content simultaneously hinders the sinterability, which explains the reduction in relative density as a function of GAIN, reaching ~89% of the theoretical density for 25 wt % GAIN/α-Al$_2$O$_3$ (Table 1). Figure 2a–j shows the microstructure of different regions of the sample FSM-89-1. The outer layers consisting of pristine α-alumina possess significantly larger grains well recognizable in Figure 2d for the top layer and in Figure 2j for the bottom layer. Microhardness test has revealed a slight increase in hardness of alumina by the addition of 1 wt % GAIN fillers reaching a value of 21 GPa in layer h_6 of sample FSM-89-1 (Figure S2). The microstructural features of the structures are in agreement with previous characterization performed by the authors.[11,17] Confocal Raman spectroscopy was used to investigate the distribution

of the GAIN fibers along the multilayer structure and to characterize the doping, strain, and defects in graphene by evaluating large areas. The Raman mappings corresponding to the selected areas visible in the optical images for the D, G, D', 2D, and D + D' Raman modes presented in Figure 2k show a homogeneous distribution of the fibers within the interlayers of the sample FSM-89-1. The D peak intensity increases as a function of GAIN content in each layer as expected, while the resonance due to graphene 2D and D + D' peaks does not change significantly (for a detailed characterization of GAIN, see Figure S4 and Table S1). However, a discussion in terms of intensity ratios can better elucidate the defects and doping in each layer. Therefore, Lorentzian fitting was carried out to determine the Raman peak position, intensity, and fwhm and to decompose the G and D' peaks. The average Raman spectra of each layer of the FSM-89-1 structure, designated as h_1, h_2, h_3, h_4, h_5, and h_6, are presented in Figure 3a for the 900−3100 cm^{-1} range. Figure 3b,c shows details of the Raman spectra in the range of 1200−1700 and 2500−3100 cm^{-1}, respectively. The I_{2D}/I_G ratio shown in Figure 3d decreases as a function of GAIN content, indicating sharpening of the G peak and broadening of the 2D peak enforced by the gradient in GAIN filler content throughout the cross section of the sample
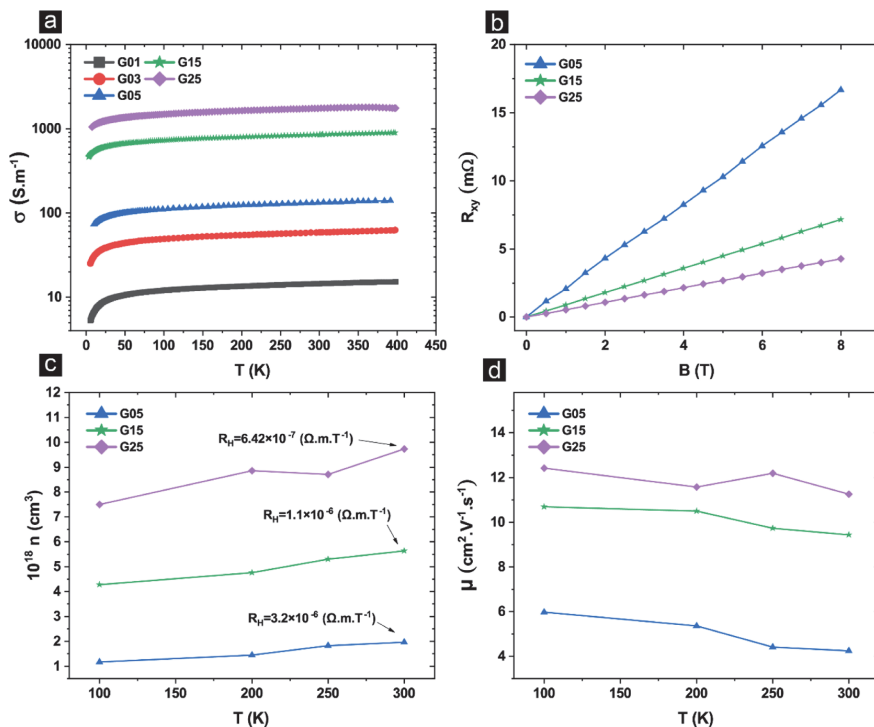
Figure 4. (a) Temperature dependency of volume resistivity of the bulk composites; (b) Hall resistance (R_{xy}) versus magnetic field; (c) carriers' density in the bulk composites and Hall coefficient inset values; and (d) carriers' mobility in bulk composites as a function of temperature.

(Table S2). No shift is observed for D′ peak located at 1620 cm^{-1} throughout the multilayer. By increasing the GAIN content in the multilayer structure, the G peak shifts from 1590 to 1588 cm^{-1}. The blue shift of the G peak from the reference 1585 cm^{-1} in GAIN fillers and the stiffening at lower GAIN contents can be attributed to both n- and p-doping, which is a result of the nonadiabatic removal of the Kohn anomaly at the Γ point.[18,19] The characteristic G peak for graphene at ∼1580 cm^{-1} is a response to the stretching of the C−C bond in sp^2-hybridized atoms, which cause in-plane high-frequency vibrations of E_{2g} phonons at Γ point of the Brillouin zone. Therefore, it is directly in connection with the amount of sp^2 rings. The D peak at ∼1350 cm^{-1} is induced by disorder and corresponds to the breathing modes of sp^2 rings and thus can be used to surveil the disorder in sp^2-hybridized carbon systems.[20] The gradual increase in I_D/I_G ratio (Figure 3e) by increasing GAIN content can also be in connection with the increase in the level of disorders attributed to the GAIN content gradient.[21] The $I_D/I_{D'}$ ratio shown in Figure 3f for all layers is between 2.5 and 3.5, suggesting a combined vacancy-like and on-site defected structure as described by the double-resonant Raman scattering theory for graphene structures.[22,23] A slight blue shift in the position of the 2D peak is visible in layers with lower GAIN content (Figure 3c). This blue shift agrees with the results reported for turbostratic carbon.[20] However, it can also be associated with the strain caused by the interaction of the top layer graphene on GAIN fibers, with the α-Al$_2$O$_3$ grains of the matrix.[24,25] A blue shift of the 2D peak can also be a result of p-doping[18] in the presence of electron-accepting aluminum interstitials, oxygen vacancies, and impurities in alumina[11] and is a response to the change of the equilibrium lattice parameter.[18] Another evidence on the p-doping in the GAIN-alumina structures is the p-type conduction in the composites, as will be discussed in Section 3.2. A consequence of the said interaction is the localization of electrons that is presumed to be one source for the interfacial polarization phenomenon that will be described in Section 3.3. The second order of the D peak in graphene structures consists of one peak at ∼2670 cm^{-1} and is caused by double-resonance scattering TO phonons at the k-point of the Brillouin zone. The wider this Raman peak gets, the more layers of graphene are expected.[26] For few-layer graphene, the I_{2D}/I_G ratio is about 4; however, in all layers, this ratio is between 0.4 and 0.6. This observation together with the slight blue shift (∼15−30 cm^{-1}) of the 2D band, once again, agrees with the results for turbostratic carbon[20] and/or graphene deposited onto the sapphire substrate.[24] The difference in the 2D blue shift between various layers is likely to be in connection with the p-doing level. In other words, change in the blue shift of the 2D peak from 2692 to 2700 cm^{-1} in h$_2$ layer to h$_6$ layer, respectively, is likely to be in connection with the higher p-doping level in h$_6$ with 1 wt % of the fillers. Regardless of the doping effect, the opposite thermal expansion and contraction of the carbon and alumina during the cooling stage of the sintering can deposit compressive stresses, which can increase the phonon frequency of various bands and virtually cause an upshift of the spectrum.[25]
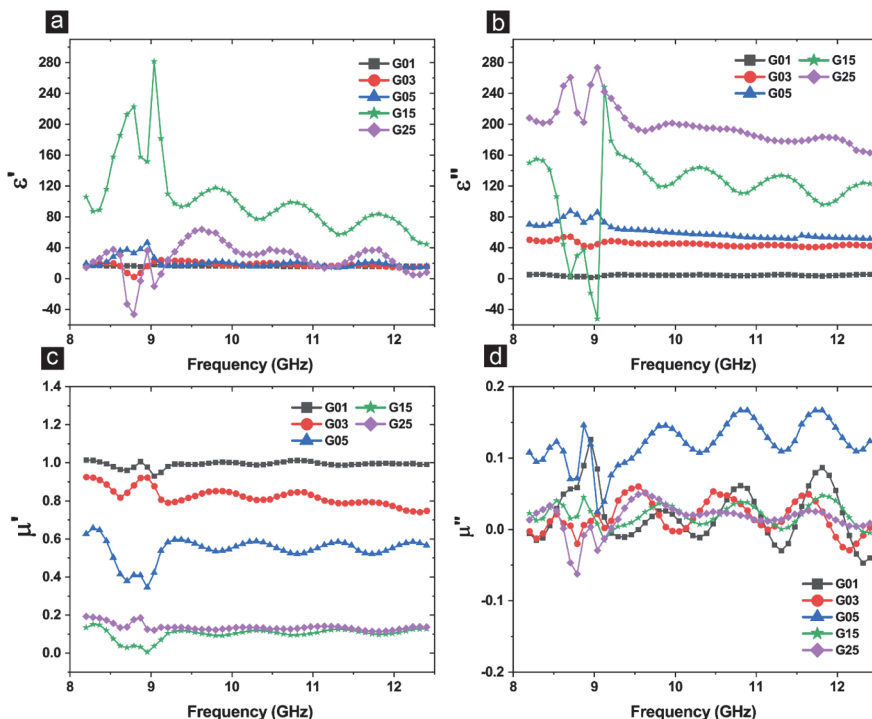
Figure 5. (a) Real part of permittivity; (b) imaginary part of permittivity; (c) real part of permeability; (d) and imaginary part of permeability of GAIN/α-Al$_2$O$_3$ bulk composites.

3.2. Electrical Transport.

In all bulk composites, the electrical conductivity decreases as a function of temperature from 400 to 4 k (Figure 4a), confirming a semiconducting behavior with a narrow band gap modulated by the presence of grain boundary interaction with graphene domains on the GAIN fibers. The activation energy calculated from the slope of the line of Arrhenius plot in all bulk composites is ~0.3−0.5 meV, which is one-fold smaller than 5.6 meV for the pristine GAIN fibers. The electrical percolation threshold previously achieved at 3 wt % of the fillers[11] in this study was attained at 1 wt % of GAIN, corresponding to ~0.12 wt % of carbon content, due to a homogeneous dispersion of the GAIN fillers. In the Hall resistance (R_{xy}) versus field plot (Figure 4b), the slope decreases as a function of GAIN content, decipherable by the increased carriers' density visible in Figure 4c. It was previously shown that GAIN fibers inherently possess n-type conduction attributed to multilayer graphene; and their RT p-type behavior was correlated with the physisorbed water.[11] When sintered in a matrix of α-Al$_2$O$_3$, a positive Hall coefficient in all samples (Figure 4c) provides an evidence on p-type conduction resulted from the p-doping effect of α-Al$_2$O$_3$ matrix also discussed in Section 3.1. It was shown that the effect of substrate on the electronic properties of graphene can be significant if there is a strong interaction between the two.[27] Given that the expansion coefficients of carbon on GAIN fibers and α-Al$_2$O$_3$ matrix follow an opposite trend, during the cooling stage of the sintering process, a large residual stress would cause great pressure, which leads to a firm contact between them. This interaction in the environment of

a low oxygen partial pressure and in the presence of electron accepting impurities and point defects (such as aluminum interstitials and oxygen vacancies) induces p-doping of graphene. Similar phenomena were reported in ref[28] for few-layer graphene/Al$_2$O$_3$ composites. The p-doping occurs in the outermost layer; however, the subsequent layers can be affected through charge transfer.[28] The result is the localization of charge, whose contribution to dielectric polarization will be discussed in Section 3.3. The R_H values decrease with increasing graphene content, which is a result of increasing carrier density following the $|R_H| \propto 1/ne$ relation (Figure 4c), implying a higher contribution of electrons to the transport. Despite the increase in carrier density and more chance for impurity scattering, mobility slightly increases with GAIN content (Figure 4d). This effect can be attributed to the lower effective mass of electrons and subsequently their contribution to higher mobility.

3.3. Dielectric Properties.

Complex permittivity and permeability obtained from NRW are presented in Figure 5a−d. The real (ε') and imaginary (ε'') parts of permittivity increase as a function of GAIN content. In fact, complex permittivity represents polarization of the charges induced by the applied field. The real part—ε' represents the energy storage or charge capacity while the imaginary part—ε'' is a measure of the ability of a material to dissipate energy in the form of heat (dielectric loss) due to rearrangement of electric dipole moments in an induced electric field[29] and is directly connected with AC conductivity via $\sigma_{AC=}\ \omega\varepsilon_0\varepsilon''$. AC conductivity is a complex number whose real part (σ') is

related to in-phase current that results in the absorption of energy via joule heating, and its imaginary component (σ'') quantifies the $\pi/2$ out-of-phase inductive current.[30] Given that, rather intuitively, the AC conductivity also follows an increasing trend as a function of GAIN content (Figure S1), a decline in ε' in the case of G25 with the highest concentration of GAIN fillers is an unusual observation. In fact, several measurements on the samples have shown that G25 is the only sample demonstrating large uncertainties in the ε' from purely negative values to values well above 300 (Figure S5). One reasonable assumption for this phenomenon maybe related to the microstructure of the G25, where a progressive increase in the porosity is observed. The porosity level in this sample is a result of increased carbon content which hinders compaction as discussed in the previous work of the authors.[11] Moreover, since the propagation mode utilized in the measurement was the TE mode, a significant anisotropy in the microstructure of the samples (parallel to the electric field lines) with high GAIN contents could be the second influencing factor. This anisotropy and its substantial contribution to the thermal properties of the structures were discussed in depth elsewhere.[31] Negative permittivity was also observed for a high concentration of graphene oxide in alumina matrix by others.[6] Nevertheless, G25 steadily showed a higher attenuation ability decipherable from the overall highest dielectric loss tangent shown in Figure 6a, also visible in
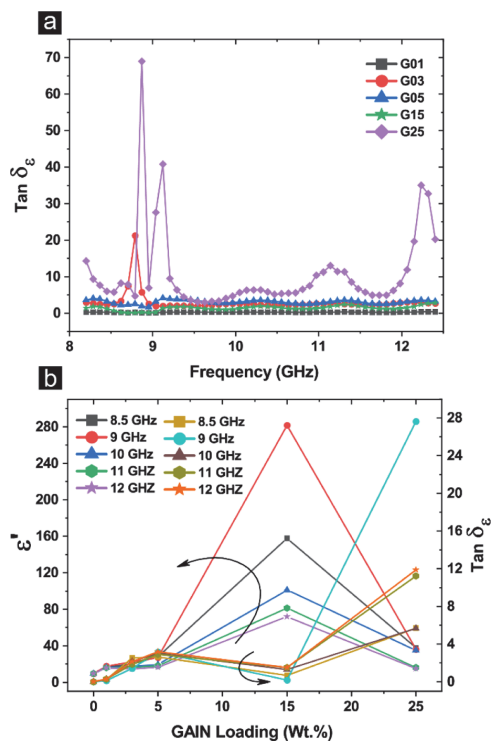

Figure 6. (a) Dielectric loss tangent of GAIN/α-Al$_2$O$_3$ bulk composites and (b) real part of permittivity and dielectric loss tangent as a function of GAIN content for sample frequencies 8.5, 9, 10, 11, and 12 GHz.

Figure 6b for the sample frequencies of 8.5, 9, 10, 11, and 12 GHz. Correspondingly, the power of dielectric loss of an absorber material is connected to the relation between complex permittivity and conductivity through $\tan \delta_\varepsilon = (\omega\varepsilon'' + \sigma)/(\omega\varepsilon')$. The higher the loss tangent is, the higher the attenuation ability of the material is.[3] Another distinctive observation is the resonant phenomena occurring at 8.5−9 GHz in all composite samples, which is amplified by an increase in the filler content. It is known that the NRW method is divergent at integer multiples of one-half wavelength in sample under test. This divergence leads to uncertainty at those frequencies in conversion of S-parameters to ε and μ.[32] However, for GAIN/alumina composites, this effect can be ruled out since the sample thickness is smaller than one-half wavelength (refer to Figure S1 for refractive indices). On the other hand, repeating the measurement using a one-port short-circuit (backed with PEC) method yielded resonance at a similar frequency region and overall similar ε for all samples (except for G25 due to increased porosity), confirming the accuracy of the measurement in both cases. In addition, in both cases, a reference pristine polycrystalline alumina specimen was measured, for which $\varepsilon' \sim 10$ and $\varepsilon'' \sim 0.01$ agree with the reported values (Figure S6).[33] Subsequently, the effect can be correlated with the dielectric resonance phenomenon that arises from polarization of charge at various interfaces (graphene-dielectric) in core−shell GAIN fillers. In fact, it is shown that metamaterial characteristics such as negative permittivity and resonance can be achieved in composites with high-permittivity rods arranged in a much lower permittivity matrix.[34] Artificial anisotropy of effective permittivity, and Mie-type resonance, measured in a rectangular waveguide and converted using NRW, was reported for composites of BaTiO$_3$ rods in the ABS matrix.[35] In fact, charge separation along the heterointerfaces leads to strong dielectric resonances.[36] Similarly, in G15 and G25 with a much higher content of GAIN fibers, a more pronounced resonant peak is observed. The S-parameters for G15-G25 are provided in Figure S7. Nonetheless, the complex shape of the resonance peaks can be attributed to the multiple discrete interfaces in GAIN and various boundaries with alumina matrix (regions of high and low permittivity). As mentioned above, complex permittivity represents polarization of the charges. In general, this polarization is in the forms of ionic, dipolar, atomic, electronic, and interfacial. At the microwave frequencies, the electronic and dipolar modes of polarizations are considered as the main contributors. However, in heterogeneous systems such as composites with nanofillers, a large interfacial area between the resistive matrix and the conductive fillers promotes the interfacial polarization mechanism, leading to high permittivity. As the filler content increases, the available interfacial area increases, which subsequently augments the loss tangent of the bulk.[4]

Theoretically, the polarization processes involved in the structures under study can arise from interfacial polarization at the boundary between fillers and the Al$_2$O$_3$ matrix, defect-dipole polarization from the disordered graphene structure, and the presence of functional groups in GAIN fillers (discussed in ref 11), providing further polarization/relaxation process. Additionally, increasing filler content introduces porosity, which acts as polarization centers.[37] Furthermore, additional interfacial polarizations can arise due to the hybrid core/shell structure of GAIN fibers. In other words, strong dispersion relation of the density of states between the
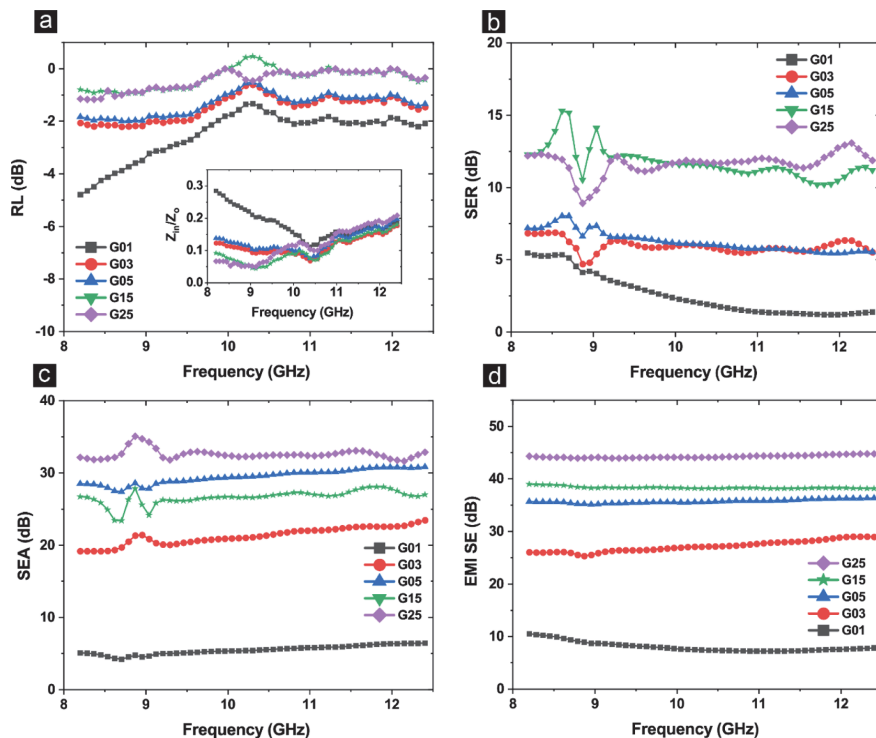
Figure 7. (a) Reflection loss—inset: normalized input impedance Z_{in}/Z_o; (b) SE due to reflection; (c) SE due to absorption; and (d) total SE of GAIN/α-Al$_2$O$_3$ bulk composites.

graphene coating and the γ-Al$_2$O$_3$ core and the outermost layer of the graphene and Al$_2$O$_3$ matrix can lead to the localization of electrons and accumulation of the space charge, forming nanosized capacitor-like structures, which translate EM into interfacial polarization.[38] Specifically, at low filler contents, the interfacial polarization and its relaxation phenomenon—described by the Maxwell–Wagner–Sillars theory—can influence the energy dissipation as the interfacial polarization becomes the primary factor influencing the bulk ε''.[39] These processes and their contribution to absorption are indeed frequency dependent and each has a unique cutoff frequency that is the intrinsic characteristic of a certain material.[40] A resonant process is associated with atomic and electronic polarization processes while a relaxation process is the evidence of orientation and ionic polarization.[37] The presence of various polarization processes is apparent from several semicircles in Cole–Cole diagrams (Figure S8).

The real part of permeability (μ') follows an opposite trend, namely, an overall decrease as a function of GAIN content. The anisotropic c-axis diamagnetic response of graphene material is well established and understood.[41] The same effect is valid for CNTs, while the diamagnetic response increases linearly by an increase in the diameter of CNT.[42] In the TE mode, the electric field lines propagate parallel to the xy-plane of the composites, with microstructural anisotropy (preferential orientation of grains and fillers alignment) being present in the same spatial plane, specifically at higher concentrations of GAIN fillers. Meanwhile, the magnetic field propagation is parallel to the z-axis (perpendicular to the xy-plane),

promoting velocity normalization, which manifests in the form of orbital diamagnetic response to the applied magnetic field.[41,43] On the other hand, probable emergence of spatial dispersion in composites as a result of their intrinsic granularity is shown to cause dipole-like interactions, which enhance the direction-sensitive local magnetic response of bulk composites.[44] These assumptions can provide explanation on the near-zero μ at 15–25 wt % GAIN and overall decline of μ as a function of GAIN. From Figure 5a,c, it is evident that the resonant peaks in ε' between 8.5 and 9 GHz coincide with the antiresonant peaks in μ', where the peaks in one align with the troughs in the other. A similar effect is present in the imaginary component of both properties (Figure 5b,d). In fact, through spatial dispersion that exists as an intrinsic property of composite structures, any contribution to ε can be alternatively represented by a contribution to μ.[45] That is to say, in GAIN/alumina composites, the resonances in μ are induced by the dielectric resonances observed for ε'.

The reflection loss (RL) data calculated using eqs 1 and 2 are shown in Figure 7a. Considering that the samples are backed by a perfect electric conductor (PEC), the power of the incident wave (P_{in}) can be divided into three parts: the power of the reflected wave (P_r), the power of the absorbed wave (P_a), and the power of the transmitted wave (Pt). Since the PEC backing is present, the power of the transmitted wave can be considered to be zero; hence, the absorption can be calculated as $P_a = P_{in} - P_r$. The lowest absorption and correspondingly the highest reflection loss values are found for G15 and G25 due to the high concentration of the conductive
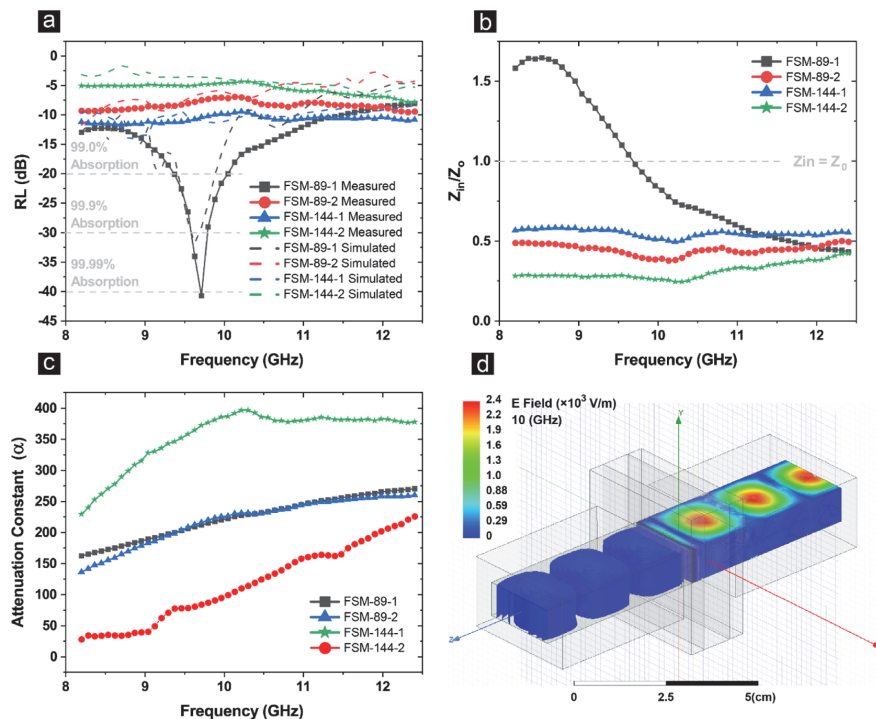
I

Figure 8. (a) Comparison of the simulated and measured reflection loss in multilayers; (b) input impedance ratio relative to free space; (c) attenuation constant in multilayers; and (d) simulation of the E-fields in the TE10 mode of a two-port transmission line, acting on FSM-89 in a partially filled WR-90 waveguide at 10 GHz.

fillers, resulting in a higher impedance mismatch (Figure 7a, inset) which limits the total power transfer to the structures. The SE due to reflection is shown in Figure 7b, and the SE due to absorption (SEA) of the transferred portion of the power is shown in Figure 7c. The total SE (EMI SE) is demonstrated in Figure 7d. It was previously mentioned that the attenuation ability of the structures increases as a function of GAIN content. Subsequently, their SEA and EMI SE increase, with the exception of SEA of the samples G05 and G15 (Figure 7c). In fact, a higher concentration of conductive fillers in G15 as compared to G05 leads to a more reflective surface in this sample (Figure 7a,b), while its attenuation ability is slightly subject to decay due to a decrease in μ'. The overall outcome is an almost similar EMI SE of G05 and G15, while G15 has a higher impedance mismatch, therefore a higher reflection loss. To summarize, all samples with the exception of G01 demonstrate strong shielding abilities with EMI SE higher than 25 dB. However, all samples have almost RL > −3 dB, suggesting that at least 50% of the input power loss was due to the surface reflection. In contrast, a suitable MAM candidate must meet the prerequisite condition of RL < −10 dB.[46]

Subsequently, focus was put toward designing a functionally graded multilayer structure using the impedance matching technique in order to reduce the surface impedance mismatch, which is the root cause of surface reflection and is dependent on both ε' and ε''.[47] When the EM radiation encounters the surface of a material, a mismatch between the intrinsic impedance of the surface and the area adjacent to it results in surface reflection loss, and consequently, less power transfer

to the structure is supposed. Similarly, in the multilayer structures, the internal mismatch between the adjacent layers is an artifact of refraction of light described by Snell's law. An optimal design for an absorber demands for minimization of the mismatch between Z_0 and Z_i, where Z_0 is the impedance of the free space and Z_i is the intrinsic impedance of the ith layer. Impedance matching (based on eqs 1−3 and measured values for complex ε and μ) can result in various solutions depending on the chosen boundary conditions. Several methods exist in order to qualify an optimized solution by rigorously defining the boundary conditions. In this work, an algorithm was developed based on the Monte Carlo method in order to generate various solutions to the multilayer problem with the condition of RL < −10 dB (Figure S9). Few of the findings of the Monte Carlo were with a gradient GAIN composition and thickness transition similar to the Fibonacci order (similar to FSM-89-1). Therefore, for experimental verification, FSM-89-1 was implemented, promising to have an absorption peak of around 9.5 GHz with a bandwidth of 3 GHz with RL < −10 dB condition (Figure 8a). Additionally, for comparison, three extra multilayer specimens with layer thickness modifications and layer count adjustments (FSM-89-2, FSM-144-1, and FSM-144-2) were produced and tested. Characterization of the samples was done based on the transmission line theory and in a rectangular waveguide in the TE10 mode with a one-port reflection-only setup (for nonmagnetic specimens, $\mu' = 1$ and $\mu'' = 0$). The value of the measured reflection loss for each structure is compared to the simulation data and is depicted in Figure 8a, while the corresponding simulated Z_{in} of four

multilayer designs are shown in Figure 8b. The characterization showed that the sample FSM-89-1 with a total of 1.98 wt % GAIN corresponding to ~0.24 wt % carbon content has a broad-band 90% absorption covering almost the entire X-band and a narrow 0.5 GHz bandwidth of 99% absorption centered at 9.6 GHz. A similar structure with larger layer thicknesses (FSM-144-1) satisfies full X-band 90% absorption. The normalized Z_{in} plots in Figure 8b confirm that FSM-89-1 has the best matching outcome among the samples; with an optimal region satisfying the $|Z_{in}/Z_0| = 1$ condition between 9 and 10 GHz, which represents the same frequency region where the experimental data on the reflection loss reach a minimum at −40 dB. The attenuation constant (Figure 8c) was highest in the sample without a matching layer (FSM-144-2); however, due to a poor impedance matching, it shows the weakest absorption. The simulation of the transferred power propagating down a partially filled waveguide and passing through the sample FSM-89-1 is shown in Figure 8d. The simulation demonstrates that the TE10 mode is the single propagation mode with field lines perpendicular to the direction of the propagation and a sinusoidal wave with two nods at the walls and a peak at the center of the sample. The simulated dissipated power for FSM-89-1 is in agreement with the measurement values.

4. CONCLUSIONS

In this study, novel conductive fillers, representing the graphene-augmented γ-alumina nanofibers (GAIN), were successfully used for the first time to fabricate a functionally graded tunable microwave absorber. The functionally graded multilayer structures were designed using an impedance matching technique. The homogeneous composites and the multilayer structures based on α-alumina and GAIN were consolidated using SPS at 1150 °C and 75 MPa of uniaxial pressure under vacuum. A set of homogeneous composites and multilayer structures of pure α-alumina and GAIN were fabricated using an ex situ strategy of precipitation of the compositions from suspensions. The multilayer materials were structured with various thicknesses and filler contents in the conductive layers. The addition of GAIN fillers resulted in a microstructural refinement and an increase in porosity as a function of fillers' content in the alumina matrix adjusted to 1, 3, 5, 15, and 25 wt % of GAIN. The RT electrical conductivity was found to range from 15 S·m^{-1} at the percolation threshold at 1 wt % GAIN up to 2000 S·m^{-1} for the sample filled by 25 wt % of GAIN. The majority of charge carriers in the homogeneous bulks were of p-type, having stemmed from the p-doping effect induced by the matrix α-Al$_2$O$_3$. Raman mapping confirmed a homogeneous distribution of the fillers throughout the layers and the presence of carbon in the form of turbostratic multilayer polycrystalline graphene. Dielectric measurement in a transmission line waveguide with TE10 revealed an increasing complex permittivity as a function of conductive fillers' content. The permeability decreases due to the diamagnetic response of graphene structures together with microstructural anisotropy. The homogeneous bulks exhibited EMI SE ranging from 10 to 45 dB; however, the contribution of the surface reflection was shown to limit the functionality of the homogeneous bulks for microwave absorption applications. The design of the functionally graded multilayer structures, based on impedance matching technique, ensured the efficient use of the entire cross section of the absorber, while the surface impedance mismatch was minimized, reducing the surface

scattering effect. A functionally graded multilayer structure with a total GAIN content of ~2 wt % corresponding to ~0.24 wt % of carbon content demonstrated a 90% absorption across the X-band. The same sample showed a high absorption peak of −40 dB at 9.6 GHz. Such multilayer structures with tunable properties (i.e., broad-band and frequency-specific absorbers) can trigger potential applications in the design of electronic enclosures and radar absorbing solutions in telecommunication and aerospace.

■ ASSOCIATED CONTENT

Ⓢ Supporting Information

The Supporting Information is available free of charge at https://pubs.acs.org/doi/10.1021/acsami.1c02899.

> Refractive indices, AC conductivity, skin depth, microhardness, TEM, Raman spectra and peak position table, additional permittivity measurement, Cole−Cole diagrams, and Monte Carlo simulations (PDF)

■ AUTHOR INFORMATION

Corresponding Author

Irina Hussainova − *Department of Mechanical and Industrial Engineering, Tallinn University of Technology, 19086 Tallinn, Estonia;* ⓞ orcid.org/0000-0003-3081-2491; Phone: +372 620 3371; Email: irina.hussainova@taltech.ee

Authors

Ali Saffar Shamshirgar − *Department of Mechanical and Industrial Engineering, Tallinn University of Technology, 19086 Tallinn, Estonia;* ⓞ orcid.org/0000-0002-0762-8058

Rocio E. Rojas Hernández − *Department of Mechanical and Industrial Engineering, Tallinn University of Technology, 19086 Tallinn, Estonia*

Girish C. Tewari − *Department of Chemistry and Materials Science, Aalto University, FI-00076 Aalto, Finland*

José Francisco Fernández − *Institute of Ceramics and Glass (ICV-CSIC), 28049 Madrid, Spain;* ⓞ orcid.org/0000-0001-5894-9866

Roman Ivanov − *Department of Mechanical and Industrial Engineering, Tallinn University of Technology, 19086 Tallinn, Estonia*

Maarit Karppinen − *Department of Chemistry and Materials Science, Aalto University, FI-00076 Aalto, Finland;* ⓞ orcid.org/0000-0003-1091-1169

Complete contact information is available at:
https://pubs.acs.org/10.1021/acsami.1c02899

Notes

The authors declare no competing financial interest.

transport measurements. The authors acknowledge the originality of all figures, including the TOC graphics.

■ REFERENCES

(1) Chen, H.; Ma, W.; Huang, Z.; Zhang, Y.; Huang, Y.; Chen, Y. Graphene-Based Materials toward Microwave and Terahertz Absorbing Stealth Technologies. *Adv. Opt. Mater.* **2019**, *7*, 1801318.

(2) Delfini, A.; Albano, M.; Vricella, A.; Santoni, F.; Rubini, G.; Pastore, R.; Marchetti, M. Advanced Radar Absorbing Ceramic-Based Materials for Multifunctional Applications in Space Environment. *Materials* **2018**, *11*, 1730.

(3) *Advanced Materials for Electromagnetic Shielding*; Jaroszewski, M., Thomas, S., Rane, A. V., Eds.; John Wiley & Sons, Inc.: Hoboken, NJ, USA, 2018.

(4) *Microwave Materials and Applications 2V Set*; Sebastian, M. T., Jantunen, H., Ubic, R., Eds.; John Wiley & Sons, Ltd: Chichester, U.K., 2017.

(5) Sebastian, M. T. Alumina, Titania, Ceria, Silicate, Tungstate and Other Materials. *Dielectric Materials for Wireless Communication*; Elsevier, 2008; pp 379−443.

(6) Yuchang, Q.; Qinlong, W.; Fa, L.; Wancheng, Z. Temperature Dependence of the Electromagnetic Properties of Graphene Nanosheet Reinforced Alumina Ceramics in the X-Band. *J. Mater. Chem. C* **2016**, *4*, 4853−4862.

(7) Li, N.; Huang, Y.; Du, F.; He, X.; Lin, X.; Gao, H.; Ma, Y.; Li, F.; Chen, Y.; Eklund, P. C. Electromagnetic Interference (EMI) Shielding of Single-Walled Carbon Nanotube Epoxy Composites. *Nano Lett.* **2006**, *6*, 1141−1145.

(8) Chaudhary, A.; Kumari, S.; Kumar, R.; Teotia, S.; Singh, B. P.; Singh, A. P.; Dhawan, S. K.; Dhakate, S. R. Lightweight and Easily Foldable MCMB-MWCNTs Composite Paper with Exceptional Electromagnetic Interference Shielding. *ACS Appl. Mater. Interfaces* **2016**, *8*, 10600−10608.

(9) Jia, L.-C.; Yan, D.-X.; Jiang, X.; Pang, H.; Gao, J.-F.; Ren, P.-G.; Li, Z.-M. Synergistic Effect of Graphite and Carbon Nanotubes on Improved Electromagnetic Interference Shielding Performance in Segregated Composites. *Ind. Eng. Chem. Res.* **2018**, *57*, 11929−11938.

(10) Wu, Z.; Pei, K.; Xing, L.; Yu, X.; You, W.; Che, R. Enhanced Microwave Absorption Performance from Magnetic Coupling of Magnetic Nanoparticles Suspended within Hierarchically Tubular Composite. *Adv. Funct. Mater.* **2019**, *29*, 1901448.

(11) Shamshirgar, A. S.; Rojas Hernández, R. E.; Tewari, G. C.; Ivanov, R.; Mikli, V.; Karppinen, M.; Hussainova, I. Layered Structure of Alumina/Graphene-Augmented-Inorganic-Nanofibers with Directional Electrical Conductivity. *Carbon* **2020**, *167*, 634−645.

(12) Ivanov, R.; Hussainova, I.; Aghayan, M.; Drozdova, M.; Pérez-Coll, D.; Rodríguez, M. A.; Rubio-Marcos, F. Graphene-Encapsulated Aluminium Oxide Nanofibers as a Novel Type of Nanofillers for Electroconductive Ceramics. *J. Eur. Ceram. Soc.* **2015**, *35*, 4017−4021.

(13) Drozdova, M.; Hussainova, I.; Pérez-Coll, D.; Aghayan, M.; Ivanov, R.; Rodríguez, M. A. A Novel Approach to Electroconductive Ceramics Filled by Graphene Covered Nanofibers. *Mater. Des.* **2016**, *90*, 291−298.

(14) Stamatin, S. N.; Hussainova, I.; Ivanov, R.; Colavita, P. E. Quantifying Graphitic Edge Exposure in Graphene-Based Materials and Its Role in Oxygen Reduction Reactions. *ACS Catal.* **2016**, *6*, 5215−5221.

(15) Hossain, M. E.; Liu, S. Y.; O'Brien, S.; Li, J. Modeling of High-k Dielectric Nanocomposites. *Acta Mech.* **2014**, *225*, 1197−1209.

(16) Simpkin, R. Derivation of Lichtenecker's Logarithmic Mixture Formula From Maxwell's Equations. *IEEE Trans. Microwave Theory Tech.* **2010**, *58*, 545−550.

(17) Shamshirgar, A. S.; Ivanov, R.; Hussainova, I. Spark plasma sintering of layered γ-Al2O3/graphene reinforced nanocomposites. *Proc. Est. Acad. Sci.* **2019**, *68*, 140−144.

(18) Das, A.; Pisana, S.; Chakraborty, B.; Piscanec, S.; Saha, S. K.; Waghmare, U. V.; Novoselov, K. S.; Krishnamurthy, H. R.; Geim, A. K.; Ferrari, A. C.; Sood, A. K. Monitoring Dopants by Raman

(19) Pisana, S.; Lazzeri, M.; Casiraghi, C.; Novoselov, K. S.; Geim, A. K.; Ferrari, A. C.; Mauri, F. Breakdown of the adiabatic Born-Oppenheimer approximation in graphene. *Nat. Mater.* **2007**, *6*, 198−201.

(20) Ferrari, A. C.; Basko, D. M. Raman Spectroscopy as a Versatile Tool for Studying the Properties of Graphene. *Nat. Nanotechnol.* **2013**, *8*, 235−246.

(21) Reich, S.; Thomsen, C. Raman Spectroscopy of Graphite. *Philos. Trans. R. Soc., A* **2004**, *362*, 2271−2288.

(22) Venezuela, P.; Lazzeri, M.; Mauri, F. Theory of Double-Resonant Raman Spectra in Graphene: Intensity and Line Shape of Defect-Induced and Two-Phonon Bands. *Phys. Rev. B: Condens. Matter Mater. Phys.* **2011**, *84*, 035433.

(23) Eckmann, A.; Felten, A.; Mishchenko, A.; Britnell, L.; Krupke, R.; Novoselov, K. S.; Casiraghi, C. Probing the Nature of Defects in Graphene by Raman Spectroscopy. *Nano Lett.* **2012**, *12*, 3925−3930.

(24) Hwang, J.; Kim, M.; Campbell, D.; Alsalman, H. A.; Kwak, J. Y.; Shivaraman, S.; Woll, A. R.; Singh, A. K.; Hennig, R. G.; Gorantla, S.; Rümmeli, M. H.; Spencer, M. G. Van Der Waals Epitaxial Growth of Graphene on Sapphire by Chemical Vapor Deposition without a Metal Catalyst. *ACS Nano* **2013**, *7*, 385−395.

(25) Tsoukleri, G.; Parthenios, J.; Papagelis, K.; Jalil, R.; Ferrari, A. C.; Geim, A. K.; Novoselov, K. S.; Galiotis, C. Subjecting a Graphene Monolayer to Tension and Compression. *Small* **2009**, *5*, 2397−2402.

(26) Gao, G.; Liu, D.; Tang, S.; Huang, C.; He, M.; Guo, Y.; Sun, X.; Gao, B. Heat-Initiated Chemical Functionalization of Graphene. *Sci. Rep.* **2016**, *6*, 20034.

(27) Wang, Y. y.; Ni, Z. H.; Yu, T.; Shen, Z. X.; Wang, H. M.; Wu, Y. H.; Chen, W.; Shen Wee, A. T. Raman Studies of Monolayer Graphene: The Substrate Effect. *J. Phys. Chem. C* **2008**, *112*, 10637−10640.

(28) Fan, Y.; Jiang, W.; Kawasaki, A. Highly Conductive Few-Layer Graphene/Al2O3Nanocomposites with Tunable Charge Carrier Type. *Adv. Funct. Mater.* **2012**, *22*, 3882−3889.

(29) Sun, H.; Che, R.; You, X.; Jiang, Y.; Yang, Z.; Deng, J.; Qiu, L.; Peng, H. Cross-Stacking Aligned Carbon-Nanotube Films to Tune Microwave Absorption Frequencies and Increase Absorption Intensities. *Adv. Mater.* **2014**, *26*, 8120−8125.

(30) *Fundamentals of the Physics of Solids*; Sólyom, J., Ed.; Springer Berlin Heidelberg: Berlin, 2009.

(31) Hussainova, I.; Shamshirgar, A. S.; Ivanov, R.; Volobujeva, O.; Romanov, A. E.; Gasik, M. Directional Conductivity in Layered Alumina. *Curr. Appl. Phys.* **2020**, DOI: 10.1016/j.cap.2020.06.009.

(32) Nguyen, V. H.; Hoang, M. H.; Phan, H. P.; Hoang, T. Q. V.; Vuong, T. P. Measurement of Complex Permittivity by Rectangular Waveguide Method with Simple Specimen Preparation. *2014 International Conference on Advanced Technologies for Communications (ATC 2014)*; IEEE, 2014; Vol. *2015-Febru*, pp 397−400.

(33) Thorp, J. S.; Akhtaruzzaman, M.; Evans, D. The Dielectric Properties of Alumina Substrates for Microelectronic Packaging. *J. Mater. Sci.* **1990**, *25*, 4143−4149.

(34) Zhao, Q.; Zhou, J.; Zhang, F.; Lippens, D. Mie Resonance-Based Dielectric Metamaterials. *Mater. Today* **2009**, *12*, 60−69.

(35) Isakov, D. V.; Lei, Q.; Castles, F.; Stevens, C. J.; Grovenor, C. R. M.; Grant, P. S. 3D Printed Anisotropic Dielectric Composite with Meta-Material Features. *Mater. Des.* **2016**, *93*, 423−430.

(36) Meng, F.; Wang, H.; Huang, F.; Guo, Y.; Wang, Z.; Hui, D.; Zhou, Z. Graphene-Based Microwave Absorbing Composites: A Review and Prospective. *Composites, Part B* **2018**, *137*, 260−277.

(37) *Microwave Materials and Applications*; Sebastian, M. T., Ubic, R., Jantunen, H., Eds.; John Wiley & Sons, 2017.

(38) Zhang, X. F.; Guan, P. F.; Dong, X. L. Multidielectric Polarizations in the Core/Shell Co/Graphite Nanoparticles. *Appl. Phys. Lett.* **2010**, *96*, 223111.

(39) Qing, Y. C.; Zhou, W. C.; Jia, S.; Luo, F.; Zhu, D. M. Electromagnetic and Microwave Absorption Properties of Carbonyl

Iron and Carbon Fiber Filled Epoxy/Silicone Resin Coatings. *Appl. Phys. A: Mater. Sci. Process.* **2010**, *100*, 1177−1181.

(40) Sorrentino, R.; Bianchi, G. *Microwave and RF Engineering*; John Wiley & Sons, 2010.9780470758625.

(41) Semenenko, B.; Esquinazi, P. Diamagnetism of Bulk Graphite Revised. *Magnetochemistry* **2018**, *4*, 52.

(42) Nakai, Y.; Tsukada, R.; Miyata, Y.; Saito, T.; Hata, K.; Maniwa, Y. Observation of the Intrinsic Magnetic Susceptibility of Highly Purified Single-Wall Carbon Nanotubes. *Phys. Rev. B: Condens. Matter Mater. Phys.* **2015**, *92*, 041402.

(43) Ando, T. Magnetoresistance Due to Diamagnetic Response in Two-Dimensional System. *J. Phys. Soc. Jpn.* **2020**, *89*, 124708.

(44) Silveirinha, M. G.; Belov, P. A. Spatial Dispersion in Lattices of Split Ring Resonators with Permeability near Zero. *Phys. Rev. B: Condens. Matter Mater. Phys.* **2008**, *77*, 233104.

(45) Koschny, T.; Markoš, P.; Smith, D. R.; Soukoulis, C. M. Resonant and Antiresonant Frequency Dependence of the Effective Parameters of Metamaterials. *Phys. Rev. E: Stat., Nonlinear, Soft Matter Phys.* **2003**, *68*, 065602.

(46) Zhao, B.; Guo, X.; Zhao, W.; Deng, J.; Shao, G.; Fan, B.; Bai, Z.; Zhang, R. Yolk-Shell Ni@SnO2 Composites with a Designable Interspace To Improve the Electromagnetic Wave Absorption Properties. *ACS Appl. Mater. Interfaces* **2016**, *8*, 28917−28925.

(47) Liu, Q.; Cao, Q.; Bi, H.; Liang, C.; Yuan, K.; She, W.; Yang, Y.; Che, R. CoNi@SiO2@TiO2and CoNi@Air@TiO2Microspheres with Strong Wideband Microwave Absorption. *Adv. Mater.* **2016**, *28*, 486−490.

Paper IV

Saffar Shamshirgar, A., Belmonte, M., Tewari, G. C., Rojas Hernández, R. E., Seitsonen, J., Ivanov, R., Miranzo, P., Karppinen, M., & Hussainova, I. (2021). Thermal Transport and Thermoelectric Effect in Composites of Alumina and Graphene-Augmented Alumina Nanofibers. Materials, 14(9), 2242. https://doi.org/10.3390/ma14092242.

Article

Thermal Transport and Thermoelectric Effect in Composites of Alumina and Graphene-Augmented Alumina Nanofibers

Ali Saffar Shamshirgar [1],*, Manuel Belmonte [2], Girish C. Tewari [3], Rocío E. Rojas Hernández [1], Jani Seitsonen [4], Roman Ivanov [1], Maarit Karppinen [3], Pilar Miranzo [2] and Irina Hussainova [1],*

[1] Department of Mechanical and Industrial Engineering, Tallinn University of Technology, 19086 Tallinn, Estonia; rocio.rojas@taltech.ee (R.E.R.H.); roman.ivanov@taltech.ee (R.I.)
[2] Institute of Ceramics and Glass (ICV-CSIC), Kelsen 5, 28049 Madrid, Spain; mbelmonte@icv.csic.es (M.B.); pmiranzo@icv.csic.es (P.M.)
[3] Department of Chemistry and Materials Science, Aalto University, FI-00076 Aalto, Finland; girish.tewari@aalto.fi (G.C.T.); maarit.karppinen@aalto.fi (M.K.)
[4] Department of Applied Physics, Aalto University, FI-00076 Aalto, Finland; jani.seitsonen@aalto.fi
* Correspondence: ali.saffarshamshirgar@taltech.ee (A.S.S.); irina.hussainova@taltech.ee (I.H.)

Abstract: The remarkable tunability of 2D carbon structures combined with their non-toxicity renders them interesting candidates for thermoelectric applications. Despite some limitations related to their high thermal conductivity and low Seebeck coefficients, several other unique properties of the graphene-like structures could out-weight these weaknesses in some applications. In this study, hybrid structures of alumina ceramics and graphene encapsulated alumina nanofibers are processed by spark plasma sintering to exploit advantages of thermoelectric properties of graphene and high stiffness of alumina. The paper focuses on thermal and electronic transport properties of the systems with varying content of nanofillers (1–25 wt.%) and demonstrates an increase of the Seebeck coefficient and a reduction of the thermal conductivity with an increase in filler content. As a result, the highest thermoelectric figure of merit is achieved in a sample with 25 wt.% of the fillers corresponding to ~3 wt.% of graphene content. The graphene encapsulated nanofibrous fillers, thus, show promising potential for thermoelectric material designs by tuning their properties via carrier density modification and Fermi engineering through doping.

Keywords: nanofibers; graphene; ceramic; thermal conductivity; thermoelectric

1. Introduction

Almost all energy conversion systems are associated with waste of energy in the form of heat. Thermoelectric (TE) conversion is an attractive and technologically viable solution to directly harvest this waste heat. The thermoelectric effect is described as the conversion of heat (temperature gradient) to a voltage potential through the Seebeck effect and vice versa through the Peltier effect. The efficiency of a TE material is defined by the thermoelectric figure-of-merit which is proportional to the Seebeck coefficient and electrical conductivity of the material, and inversely to its thermal conductivity. Therefore, in order to achieve high conversion efficiency, the TE materials are required to have a high Seebeck coefficient, high electrical conductivity, and low thermal conductivity. However, the tradeoff that exists between these three properties makes the design of TE materials challenging. As an example, electrical conductivity increases by increasing carrier density through the following relationship $\sigma = ne\mu$. However, an increase in carrier density results in a decline in Seebeck coefficient. An increase of the carrier density also increases the electrical contribution to the thermal conductivity and subsequently a decline in the thermoelectric Figure of Merit [1]. A number of organic [2] and inorganic [3] materials have been exploited for thermoelectric applications. However, many of the applicable semiconductor materials including but not limited to Bi_2Te_3 [4], PbTe [5], and Sb_2Te_3 [6] are

cost-intensive to manufacture and constitute of rare and/or toxic elements [1,6]. Carbon-based structures have attracted a great deal of attention due to their abundance, nontoxicity, and ease of processing [7–15]. Among them, graphene presents a remarkable potential for precise nanostructure tailoring and subsequently, on-demand tuning of properties [16]. Introducing bandgap to graphene through doping, controlling carrier density, and Fermi engineering have a direct effect on the Seebeck coefficient. Furthermore, embedding graphene into nanostructures can provide a large number of boundaries, which strongly scatter phonons, resulting in significantly suppressed thermal conductivity [17,18].

Recently, hybrid nanofillers representing graphene-augmented alumina nanofibers (GAIN) were produced through a one-step catalyst-free chemical vapor deposition (CVD) and used as nanofillers to manufacture GAIN/α-Al$_2$O$_3$ composites with various graphene contents. The results have shown that the presence of GAIN fillers up to 10 wt.% does not influence hardness, however, a significant inhibition of the grain growth was observed. It was also shown that the electrical percolation threshold of the composites lies at 3 wt.% filler content [19]. In the current study, the GAIN/α-Al$_2$O$_3$ structures are consolidated using spark plasma sintering (SPS) and their TE properties are characterized. Moreover, an in-depth discussion on thermal conductivity and its anisotropy in the structures is provided.

2. Experimental

2.1. Processing of the Composites

As the matrix, commercially available α-alumina nano-powder with an average particle size of 100 nm (TM-DAR, Taimei, Tokyo, Japan) was used. As nanofillers, GAIN fibers produced with the help of a cost-effective catalyst-free CVD method of carbon deposition onto ceramic nanostructures as detailed in [20,21] were considered. GAIN fibers were crushed in a mortar, dispersed in ethanol, and sonicated using a sonication rod (Hielscher UP400S, Hielscher Ultrasonics, Teltow, Germany) for 20 min at 30 W using the alternative regime of 4 s ON—1 s OFF, and dried in a muffle furnace following the procedure detailed in [22]. The dried fibers of 400–800 nm in length and 8–20 nm in diameter, were weighed with corresponding amounts of α-alumina, in order to prepare samples with 1–25 wt.% GAIN. Each powder composition was further sonicated for 20 min at 30 W for homogenization. After drying at 70 °C for 12 h, the blends were collected, sieved, and sintered using spark plasma sintering (FCT System GmbH SPS furnace, FCT System GmbH, Frankenblick, Germany) in a graphite die with 20 mm diameter at 1150 °C and 75 MPa in a vacuum. A full index of the samples is listed in Table 1.

Table 1. Graphene content and relative density of the produced samples.

Sample Name	α-Al$_2$O$_3$ [wt.%]	GAIN [wt.%]	GAIN [vol.%]	Graphene * [vol.%]	Relative Density
α-Al$_2$O$_3$	100	0	0	0	99.99
G1	99	1	1.13	0.21	99.32
G3	97	3	3.39	0.63	99.45
G5	95	5	5.65	1.04	98.98
G15	85	15	16.74	3.10	93.80
G25	75	25	27.56	5.10	89.51

* Calculated based on the measured 12 wt.% graphene content of GAIN.

2.2. Characterization

The microstructural characterization was carried out using scanning electron microscope (HR-SEM Zeiss Merlin, ZEISS, Oberkochen, Germany) equipped with an energy dispersive X-ray spectrometer (Bruker EDX-XFlash6/30 detector, Bruker, Billerica, MA, USA) with an operating voltage of 5 kV. The morphology of the hybrid GAIN was examined by JEOL JEM-2800 high resolution transmission electron microscope (HRTEM, JEOL Ltd., Tokyo, Japan). Confocal Raman spectra of the synthesized materials were recorded using a Horiba's LabRAM 800 (Horiba, Ltd., Kyoto, Japan) high-resolution spectrometer

equipped with a 532 nm laser excitation wavelength at room temperature (RT) and a 50× objective lens (NA = 0.95). Collected spectra are processed and analyzed using Witec Control Plus software 2.08. The incident laser power was 2.8 mW. Carbon content of the GAIN fillers was determined using a LECO CS 200 carbon-Sulphur analyzer (LECO, Minato, Japan) based on arithmetic mean of three readings. The densities (ρ) of the sintered specimens were determined using the Archimedes method with distilled water as the immersive media. The rule of mixtures using the manufacturers' density specification for alumina powder (3.96 g·cm^{-3}), alumina fibers (3.65 g·cm^{-3}), and published density value for graphene (2.2 g·cm^{-3}) was used to calculate the relative densities. The in-plane thermal diffusivity ($\alpha^{||}$) (perpendicular to the SPS pressure axis) was measured on discs with 20 mm diameter and 600 μm thickness by the laser-flash method (Thermaflash 2200, Holometrix, Netzsch GmbH, Selb, Germany). The through-plane thermal diffusivity ($\alpha^{\perp}$) (Transversal to the SPS pressure axis) was measured on square samples (8.8 × 8.8 mm^2) from 298 to 1073 K. Prior to the procedure, thin matte graphite layers were sprayed onto the samples' surfaces exposed to the laser excitation; to avoid energy loss due to surface reflection and maximize absorption. The low-temperature thermoelectric transport properties were measured using a physical property measurement system (PPMS, Quantum Design GmbH, San Diego, CA, USA); equipped with 9 T magnetic field). A set of specimens were cut using a precision diamond wheel to bars of 5 × 10 × 1 mm^3. Simultaneously, resistivity (ρ), Seebeck coefficient (S), and thermal conductivity were measured using the thermal transport puck (TTO) of the PPMS on the rectangular bars with the four-probe contact arrangement. In this procedure, at the steady state, a small amount of heat is applied to one end of the rectangular bars and the temperature difference together with the Seebeck voltage are simultaneously recorded. The Seebeck coefficient is estimated by dividing the Seebeck voltage by the temperature difference. The thermal conductivity ($k^{||}$) is calculated using the dimensions of the specimen, distance between the probes, and the temperature difference.

3. Results and Discussion

3.1. Microstructure and Composition

A schematic view of GAIN fillers and the optical images of γ-Al$_2$O$_3$ nanofibers before and after CVD are provided in Figure 1a. SEM images in Figure 1a demonstrate self-alignment of alumina nanofibers. In Figure 1b, a discontinues highly defective multilayered graphene coating is observed. TEM images of various regions of the fibers indicate a variety of stacked graphene structures ranging from 2 to 5 layers with a wide range of layer lengths. An example of a tri-layer graphene structure on the γ-Al$_2$O$_3$ fibers is shown in Figure 1c.

Raman spectra presented in Figure 1d,e show the main features of carbon materials, Raman D, G, and 2D peaks. The high intensity of the D peak as compared to G, indicates very small sp^2 graphene domains which is consistent with the HRTEM observations. Based on the double resonant Raman scattering theory, the I_D/I_G ratio of ~1.8 for GAIN corresponds to on-site and vacancy-like defect types [23,24]. The 2D peak for single-layer graphene consists of a single component that is ~5 times stronger than the G peak intensity. The broadening of the 2D peak is directly in connection with increasing graphene layer count, and its shape and locations can be used to monitor layer count and carbon structure type [25]. In GAIN structures the full width at half maximum (FWHM) of the 2D peak centered at 2669 cm^{-1} is ~116, almost five times that of the 2D peak of a common single-layer graphene, which together with the presence of a notable first order D peak at 1342 cm^{-1} corresponds to the results reported for turbostratic carbon [25]. Functionalization of graphene with hydrogen and sp^3 hybridization introduce a peak at ~2915 cm^{-1}. This peak is the second order of the intra-valley D′ peak at ~1620 [25], which is present in defected carbon structures [26]. The 2D band is 21 cm^{-1} downshifted as a result of the local strain caused by the γ-Al$_2$O$_3$ substrate [27]. In other words, a lattice mismatch between the substrate and graphene exerts physical strain on the graphene and consequently decreases phonon energies, promoting a downshift. In the case of a uniaxial

strain, the G peak is split into two features, where the second one (D′) at ~1620 cm^{-1} is in connection with the D peak [28]. Considering that D and 2D peak positions in carbon are dispersive, for comparison of the Raman shifts the laser excitation energy needs to be taken into account [25], hence, the cited reference positions are reported values obtained by 532 nm laser. In addition to the 2D band, both mechanical strain and increasing number of graphene layers should promote a downshift of the G band; however, for the GAIN fillers, the G peak is 5 cm^{-1} upshifted as compared to the 1580 cm^{-1} for single layer free-standing graphene [29]. This observation can be attributed to the doping effect of the substrate γ-Al$_2$O$_3$ [30]. To clarify, the Raman G peak corresponds to the in-plane vibration of the E$_{2g}$ phonons at the Γ point at the Brillouin zone center. Both *n*- and *p*-doping shift Fermi level away from the Diract point, decreasing the probability of charge carriers' recombination. This results in non-adiabatic perturbation of the phonons, removing the Kohn anomaly. The outcome is an increase in the phonon energy of the G peak, and the corresponding upshift [31,32]. Deconvolution of the 1100–1800 cm^{-1} range (Figure 1e) shows that in addition to the D′, two more defect-driven D* and D** peaks are present at 1210 and 1510 cm^{-1}, respectively. The D* is known to be in connection with sp^3 orbitals in disordered amorphous carbon [33] and nanocrystalline diamond [34]. The D* was also observed in graphene oxide where vibration restrictions were posed by the presence of oxygen-containing groups [35] and few-layer wrinkled graphene (FLwG) [36]. However, both bands were postulated by Ferarri et al. [34] to be in connection with sp^2-bonded configurations of transpolyacetylene segments at grain boundaries and surfaces of CVD carbon.
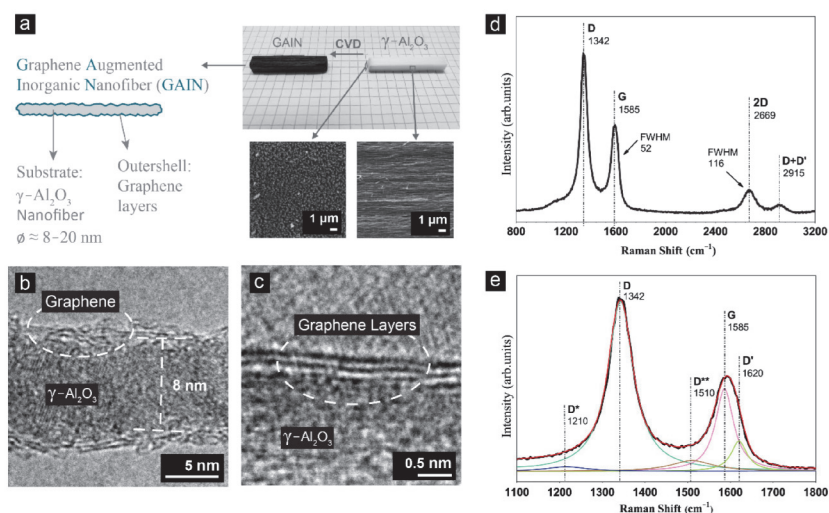

Figure 1. (**a**) Schematic of GAIN with γ-Al$_2$O$_3$ core and polycrystalline graphene coating together with SEM images of γ-Al$_2$O$_3$ nanofibers; (**b**,**c**) HRTEM images of a GAIN fiber with 2–3 layers of graphene coating; (**d**) Raman spectrum of GAIN; and (**e**) deconvolution of the peaks providing details on the Raman shift ranging from 1100 to 1800 cm^{-1}.

In Figure 2a–f the dispersion of the GAIN fillers in the powder mixtures is demonstrated in the SEM micrographs. SEM images and the microstructural features of the SPS processed composites are shown in Figure 2g–l. A gradual decrease in the grain size with an increase in the filler content is well-recognized starting from coarse 1–5 μm grains in the pristine alumina (Figure 2g) to the refined grains of around 100 nm in the G25 composite with 25 wt.% GAIN (Figure 2l). At the filler contents higher than 5 wt.%, the relative density rapidly decreases due to the pinning effect and reduced mass transport in the presence of high carbon content, which hinders densification [37]. The presence of γ-Al$_2$O$_3$

as the core of the GAIN in the α-Al_2O_3 matrix can trigger $\gamma \rightarrow \delta \rightarrow \theta \rightarrow \alpha$-$Al_2O_3$ phase transformation process in the temperature interval of 1050–1200 °C producing a vermicular microstructure [38,39]. However, under the employed sintering parameters, none of the samples demonstrate features of a vermicular structure. A discussion on the sintering temperature and its effect on the microstructure of GAIN/Al_2O_3 is detailed in [40]. The GAIN fillers are visibly located at the grain boundaries with a slight preferential orientation which is more pronounced for the composites of the high filler contents. A discussion on anisotropy will be provided in Section 3.2.
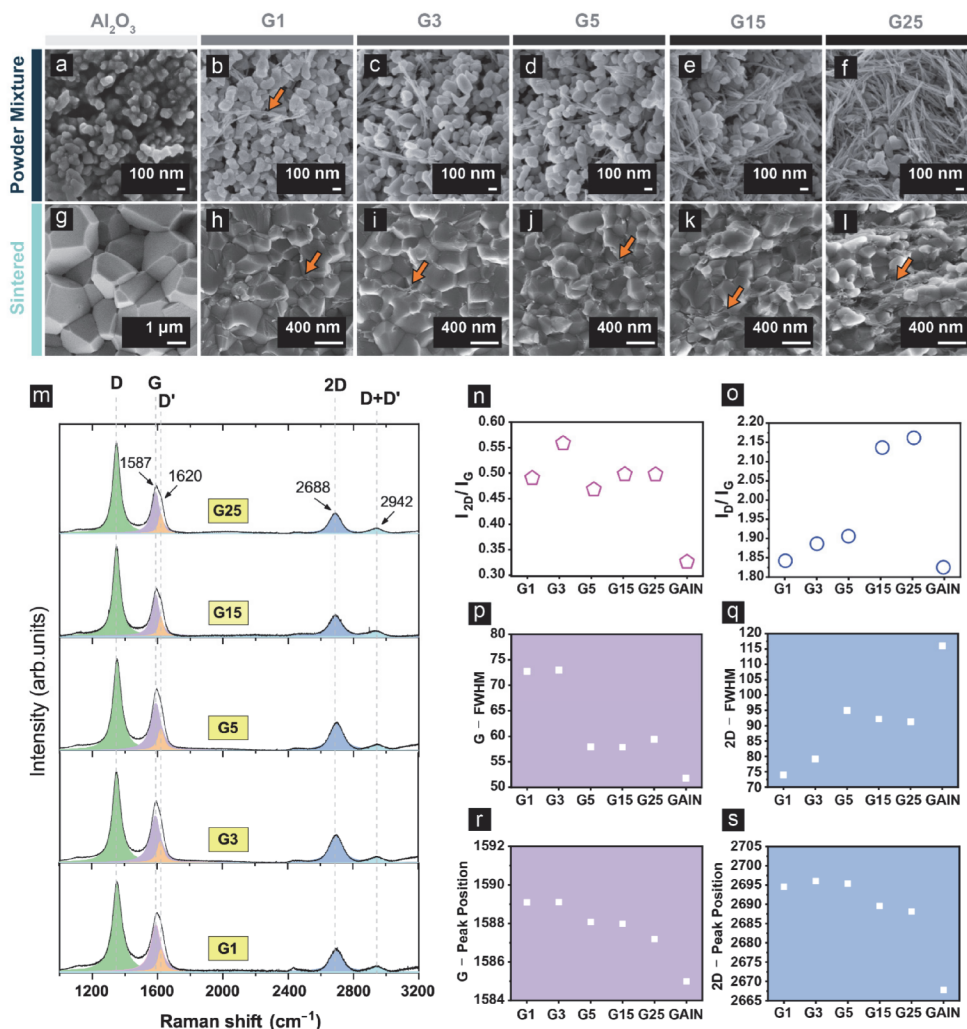

Figure 2. SEM micrographs of (**a–f**) alumina powder with various GAIN content; (**g–l**) sintered bulks consisting of reference alumina and GAIN/alumina compositions; (**m**) Raman spectra of composites with 1–25 wt.% GAIN content; (**n**) I_{2D}/I_G ratio; (**o**) I_D/I_G ratio; (**p**) G peak FWHM; (**q**) 2D peak FWHM; (**r**) G peak positions; (**s**) 2D peak position for GAIN and composites containing 1–25 wt.% GAIN fillers.

Even though the structure of the graphene is preserved in the sintering procedure, the upshift of the G and 2D peaks and broadening of FWHM of G peak in comparison with GAIN, can be evidence of both *n*- and *p*-doping induced by the α-Al_2O_3 matrix

(Figure 2m–s) [25]. However, the presence of aluminum interstitials and oxygen vacancies in the α-Al$_2$O$_3$ is more likely to contribute to the localization of electrons in the graphene sheets, promoting *p*-doping. Specifically, the upshift of the 2D band in composite structures (Figure 2s) as compared to GAIN fibers can be another supporting argument for the *p*-doping induced by the matrix [41]. A further evidence of this interpretation is the positive sign of the Seebeck coefficient that will be discussed in Section 3.3. Regardless of the doping effect in the composites, the presence of compressive stresses emanated from the opposite thermal expansion and contraction of the carbon and alumina can increase the phonon frequency of various bands and virtually cause an upshift of the spectrum [27] as evidenced in Figure 2r,s.

3.2. Thermal Properties

To calculate thermal conductivity (k) using the following equation $k = \alpha \cdot \rho \cdot C_p$, values for specific heat capacity (C_p) of γ-Al$_2$O$_3$, α-Al$_2$O$_3$, and carbon were extracted from the NIST-JANAF database [42] (Figure 3a) and the corresponding C_p values of the specimens were determined using the rule of mixture. The density (ρ) values were obtained from Archimedes density measurement and diffusivity (α) from the laser flash method. The C_p values of the composites are plotted as a function of temperature in Figure 3b.
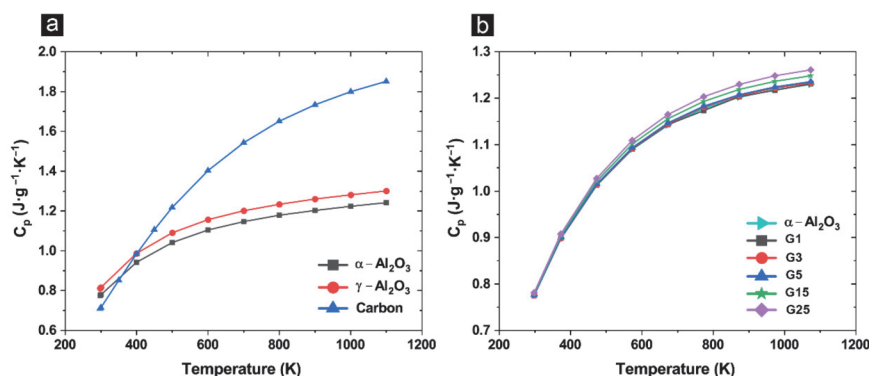

Figure 3. (**a**) Specific heat capacity (C_p) versus temperature for alumina (α and γ) and carbon using NIST-JANAF database; and (**b**) calculated C_p of the composites as a function of the GAIN content and temperature.

Both in-plane and through-plane thermal diffusivity and conductivity decrease as a function of GAIN content, as seen in Figure 4a,b. At filler contents higher than 5 wt.%, the through-plane values for both diffusivity and conductivity decrease at a higher rate as compared to in-plane values indicating a certain anisotropy in the microstructure and/or the alignment of the fillers perpendicular to the SPS pressure axis. The impact of this anisotropy can be seen in Figure 4b-inset, where the in-plane to through-plane ratio is plotted as a function of GAIN content. The higher in-plane thermal conductivity was also reported for SWCNT/alumina composites with 10 and 15 vol. % CNT content [43]. For both α and k, a significant drop can be observed specifically at up to 5 wt.% filler content, indicating a large contribution of the thermal contact and boundary resistance introduced by the presence of the fillers. Moreover, phonon-defect scattering at *Al* interstitials and *O* vacancies and presumed *p*-doping are other possible limiting factors for the thermal transport. Therefore, a detailed analysis is required to understand the thermal conductivity of the GAIN/alumina composites.
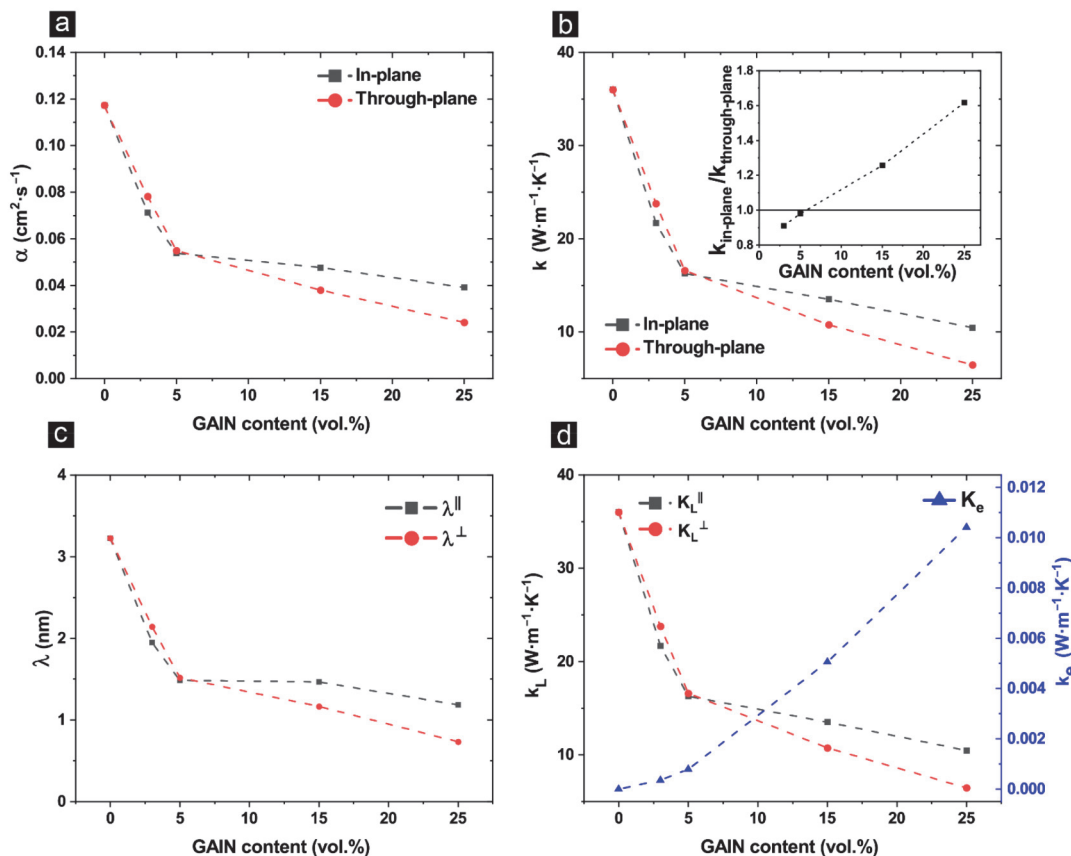
Figure 4. (**a**) Thermal diffusivity and (**b**) thermal conductivity as a function of GAIN content—inset: in-plane vs. through-plane thermal conductivity; (**c**) in-plane and through-plane mean free path as a function of GAIN content; (**d**) lattice thermal conductivity (K_L) and electronic thermal conductivity (K_e) as a function of GAIN content.

Employing Wiedemann–Franz law, the electronic (K_e) contribution to the total thermal conductivity (k) was calculated using Equation (1) in which L is the Lorenz constant equal to 2.44×10^{-8} W·Ω·K^{-2}, σ is electrical conductivity and T is the room temperature [44]. The corresponding values for composite specimens were calculated and subtracted from the total transport to obtain lattice thermal conductivity (K_L). The K_L can be correlated to phonon mean free path (λ) using Equation (2), in which C_p is the specific heat capacity, and V is the phonon group velocity of the bulk material [45]. The phonon group velocity of the bulk can be determined using Equation (3), where ρ is the bulk density, and E is the elastic modulus, attained from the previous paper of the authors [40]. The values of λ are presented in Figure 4c for both in-plane and through-plane directions. The estimated value of λ for α-alumina at 3.2 nm agrees with the reported value for polycrystalline bulks [46] and decreases by increasing GAIN content. Since electrical conductivity in all composites is in the semiconducting range, the contribution of the electronic component to the thermal conductivity is negligible (Figure 4d), therefore, the main mode of thermal transport is expected to be by phonon interactions. As the GAIN fillers are added into the alumina matrix, impurity scattering, and boundary scattering interactions limit the mean free path which in turn negatively impacts diffusivity. The latter interaction is presumed to be the reason for lower $\lambda^\perp$, since theoretically, thermal boundary resistance is more significant in transversal direction to filler alignment (refer to Section 3.1 for the discussion

on microstructural anisotropy at high filler content). At filler contents higher than 5 wt.%, despite the decrease in relative density, a slower decline of the α and k is associated with the connectivity of the fillers preserving phonon mean free path specifically for in-plane direction (Figure 4a–c) [18]. Additionally, since the grain size distribution is higher at low filler contents and decreases as a function of GAIN, the contribution of the microstructure to the phonon mean free path should not be neglected. In the present case, since the values of a few nanometers for phonon mean free path are much smaller than the grain sizes of the composites (several hundreds of nanometers), defect and impurity scatterings could be contributing more to the decrease of the phonon mean free path as compared to the boundary scattering [47]. Similar observation was done on graphene–alumina composites [48] and composites of MWCNT/alumina where the 35 W·m^{-1}·K^{-1} room temperature thermal conductivity of alumina matrix decreased as a function of MWCNT to 15 W·m^{-1}·K^{-1} for ~10 vol.% MWCNT [49].

$$K_e = L \times \sigma \times T \tag{1}$$

$$K_L = \frac{1}{3}C_P \times v \times \lambda \tag{2}$$

$$v = \sqrt{E} \times \frac{1}{\sqrt{\rho}} \tag{3}$$

In all compositions, $\alpha^{\perp}$ and $k^{\perp}$ decrease by increasing temperature from 293 K to 1100 K (Figure 5a,b). Figure 5b-inset shows the $k^{\perp}$ versus reciprocal of temperature for the composite structures. Theoretically, a straight line in this plot is an artifact of anharmonic Umklapp phonon scattering. However, in all composites, a slight deviation from a liner relationship, suggests presence of extra phonon scattering mechanisms. It is known that the presence of GAIN at grain boundaries of alumina matrix can induce interface scattering (thermal boundary resistance) which reduce mean free path at room temperature. Nonetheless, since the boundary resistance decreases by temperature, its contribution to scattering processes are less pronounced at elevated temperature [50]. In fact, temperature dependency of the GAIN/alumina composites follow the k~T^{-B} relation where the exponent "*B*" varies from 0.82 to 0.78 for G3 to G25 respectively (predicted k~T^{-B} values are shown as solid lines in Figure 5b).
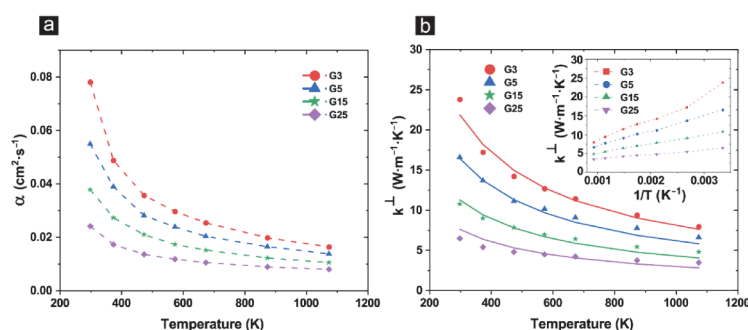

Figure 5. (**a**) through-plane diffusivity of the composite structures as a function of temperature; (**b**) through-plane thermal conductivity of the composite structures as a function of temperature (solid lines represent fittings for k~T^{-B})—inset: effective thermal conductivity versus 1/T.

3.3. Thermoelectric Performance

Resistivity decreases as a function of GAIN content (Figure 6a) and decreases in all samples by increasing temperature from 4 K to 400 K (Figure 6b). The slope of the ρ vs. *T* shows the semiconducting/semi-metallic nature of the transport while the semi-metallic behavior is more pronounced at higher filler contents. The bandgap was calculated from

the slope of the Arrhenius plot for bulk composites with 1–25 wt.% GAIN and ranges from 1.0 to 0.6 meV. Previously it was shown that both carrier types are present in the GAIN/alumina structures owing to the *n*-type GAIN fillers and the *p*-doping of the matrix alumina in the presence of point defects such as *Al* interstitials and *O* vacancies [40]. The positive values of the Seebeck coefficient in Figure 6c prove that the majority carriers are *p*-type. The values of the Seebeck coefficient increase both with temperature and GAIN content. In fact, induced Seebeck voltage is directly in connection with the diffusion process of the charged species and phonon drag. In graphene structures, the magnitude and sign of the Seebeck coefficient are influenced by the asymmetry in the distribution of the density of states near the Fermi level [2,44]. In general, increasing the Seebeck coefficient is inversely proportional to carrier density. However, increasing mobility and decreasing bandgap are associated with augmenting both σ and S [1]. Increasing carrier mobility and carrier density was established as a function of GAIN content [40]. Therefore, in the sample with the highest GAIN content (25 wt.%), and correspondingly higher carrier density and mobility, an overall higher S is achieved which peaks at 18 $\mu \cdot V \cdot K^{-1}$ at 350 K. Similar values were obtained for 17 vol.% GNP-Si_3N_4 composites [51]. Thermal conductivity rapidly increases from 4 K to peak at 120 K due to a rapid increase in thermally enabled vibration modes (Figure 6d). As the temperature increases, impurity scattering, defect-phonon scattering, and phonon-electron scattering together with the promotion of more charge carriers result in a decline of $k^{||}$ up to 400 K [44]. Thermal conductivity also decreases as a function of GAIN content due to a decline in the relative density and impurity scattering as a higher concentration of the fillers are introduced, following the same mechanisms discussed in Section 3.2. The thermal conductivity values at room temperature measured by PPMS, agree with the calculated values based on diffusivity measurement using the laser flash method.

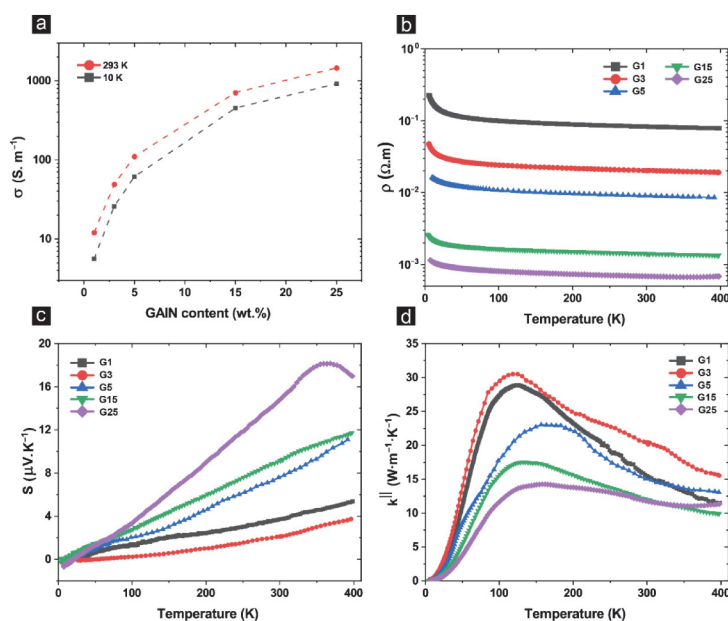**Figure 6.** (**a**) electrical conductivity as a function of GAIN content; (**b**) Temperature dependence of resistivity; (**c**) temperature dependence of Seebeck coefficient; (**d**) low temperature in-plane thermal conductivity of the composite structures.

The power factor (P.F.) and ZT values were calculated using Equations (4) and (5), respectively, and their corresponding temperature dependence values are presented in

Figure 7a,b. In these equations, σ is electrical conductivity, S is the Seebeck coefficient, k is the thermal conductivity and T is temperature.

$$P.F. = \sigma\, S^2 \qquad (4)$$

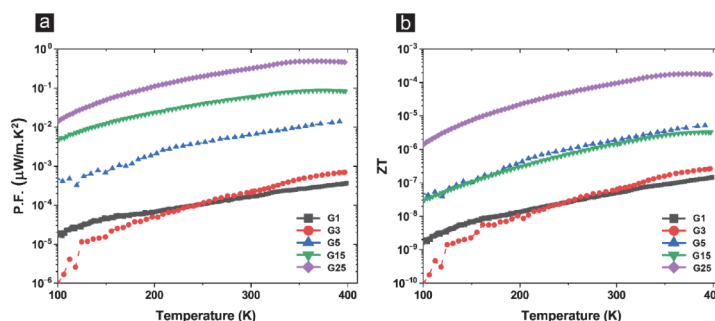$$ZT = \frac{\sigma S^2 T}{k} \qquad (5)$$

Figure 7. (**a**) Temperature dependence of power factor and (**b**) thermoelectric figure-of-merit, of composite structures.

The highest P.F. is expectedly achieved in the sample G25 with the highest GAIN content and subsequently the highest σ and S. In fact, P.F. obeys the same pattern for σ and S for all composites, however ZT values of the samples with 5 and 15 wt.% are almost identical, suggesting the same TE efficiency attributed to comparable S^2 component between the two. All in all, the highest ZT is achieved in the sample with the highest filler content due to a low thermal conductivity together with the highest power factor.

4. Conclusions

Hybrid composites of α-alumina matrix and graphene augmented γ-Al$_2$O$_3$ nanofibers as fillers have been manufactured by SPS at 1150 °C under 75 MPa uniaxial pressure in a vacuum. The filler content has been varied from 1 up to 25 wt.%, which corresponds to 0.21 to 5.10 vol.% of graphene content in the form of polycrystalline graphene consisting of 2–5 layers of highly defective structures. Raman spectroscopy on GAIN fibers have shown that the 2D peak is 21 cm^{-1} downshifted attributed to the physical strain exerted on graphene by γ-Al$_2$O$_3$ substrate, and the G peak is 5 cm^{-1} upshifted as compared to free standing single layer graphene, which was attributed to the doping effect of the substrate and surface physisorbed water. In the matrix of alumina, GAIN fillers successfully inhibit an extensive grain growth during processing, resulting in fine-structured materials as a function of the filler content. Raman spectroscopy has indicated a slight upshift of the G and 2D bands, which are inversely related to the GAIN filler content, and attributed to the doping effect of the matrix alumina. At room temperature, thermal conductivity decreases from ~35 to ~10 W·m^{-1}·K^{-1} and diffusivity from 0.12 to 0.04 cm^2·S^{-1} both for in-plane and through-plane directions as a function of GAIN content. An anisotropic thermal conductivity has been revealed for composites with filler contents >5 wt.%, slightly above the percolation threshold. The diffusivity and the thermal conductivity are slightly higher for the in-plane direction (perpendicular to the SPS pressure axis). Moreover, further decline of the thermal conductivity from room temperature to 1100 °C was correlated to the presence of various scattering mechanisms and shown to obey k ~ T^{-B} relation. Resistivity was shown to decrease with temperature and filler content from 4 K to 400 K while majority carriers in all composites were holes. The highest Seebeck coefficient and the thermoelectric Figure of Merit have been exhibited by a composite with the highest filler content (25 wt.% GAIN). The graphene augmented nanofibers have demonstrated a

great potential for thermoelectric applications by considering precise tuning of the carrier concentration and distribution of the density of states.

Author Contributions: Conceptualization, A.S.S. and I.H.; data curation, M.B., M.K. and P.M.; formal analysis, A.S.S., M.B., and P.M.; funding acquisition, I.H., M.B. and R.E.R.H.; investigation, A.S.S., M.B., G.C.T., R.E.R.H., J.S. and R.I.; methodology, A.S.S., M.B., G.C.T., J.S. and R.I.; project administration, I.H.; resources, M.B., M.K. and I.H.; software, A.S.S., G.C.T. and R.E.R.H.; supervision, I.H.; validation, G.C.T., M.K. and I.H.; visualization, A.S.S.; writing—original draft, A.S.S.; writing—review & editing, I.H. All authors have read and agreed to the published version of the manuscript.

Institutional Review Board Statement: Not applicable.

Informed Consent Statement: Not applicable.

Data Availability Statement: Not applicable.

Conflicts of Interest: The authors declare no conflict of interest.

References

1. Blackburn, J.L.; Ferguson, A.J.; Cho, C.; Grunlan, J.C. Carbon-Nanotube-Based Thermoelectric Materials and Devices. *Adv. Mater.* **2018**, *30*, 1704386. [CrossRef] [PubMed]
2. Russ, B.; Glaudell, A.; Urban, J.J.; Chabinyc, M.L.; Segalman, R.A. Organic thermoelectric materials for energy harvesting and temperature control. *Nat. Rev. Mater.* **2016**, *1*, 16050. [CrossRef]
3. Wei, J.; Yang, L.; Ma, Z.; Song, P.; Zhang, M.; Ma, J.; Yang, F.; Wang, X. Review of current high-ZT thermoelectric materials. *J. Mater. Sci.* **2020**, *55*, 12642–12704. [CrossRef]
4. Witting, I.T.; Chasapis, T.C.; Ricci, F.; Peters, M.; Heinz, N.A.; Hautier, G.; Snyder, G.J. The Thermoelectric Properties of Bismuth Telluride. *Adv. Electron. Mater.* **2019**, *5*, 1800904. [CrossRef]
5. Xiao, Y.; Zhao, L.-D. Charge and phonon transport in PbTe-based thermoelectric materials. *NPJ Quantum Mater.* **2018**, *3*, 55. [CrossRef]
6. Snyder, G.J.; Toberer, E.S. Complex thermoelectric materials. In *Materials for Sustainable Energy*; World Scientific Publishing Co.: Singapore, 2010; Volume 7, pp. 101–110. ISBN 9789814317665.
7. Li, Q.-Y.; Feng, T.; Okita, W.; Komori, Y.; Suzuki, H.; Kato, T.; Kaneko, T.; Ikuta, T.; Ruan, X.; Takahashi, K. Enhanced Thermoelectric Performance of As-Grown Suspended Graphene Nanoribbons. *ACS Nano* **2019**, *13*, 9182–9189. [CrossRef]
8. Yamawaki, M.; Ohnishi, M.; Ju, S.; Shiomi, J. Multifunctional structural design of graphene thermoelectrics by Bayesian optimization. *Sci. Adv.* **2018**, *4*, eaar4192. [CrossRef]
9. Harzheim, A.; Spiece, J.; Evangeli, C.; McCann, E.; Falko, V.; Sheng, Y.; Warner, J.H.; Briggs, G.A.D.; Mol, J.A.; Gehring, P.; et al. Geometrically Enhanced Thermoelectric Effects in Graphene Nanoconstrictions. *Nano Lett.* **2018**, *18*, 7719–7725. [CrossRef] [PubMed]
10. Anno, Y.; Imakita, Y.; Takei, K.; Akita, S.; Arie, T. Enhancement of graphene thermoelectric performance through defect engineering. *2D Mater.* **2017**, *4*, 025019. [CrossRef]
11. Wang, J.; Mu, X.; Sun, M. The Thermal, Electrical and Thermoelectric Properties of Graphene Nanomaterials. *Nanomaterials* **2019**, *9*, 218. [CrossRef]
12. Li, T.; Pickel, A.D.; Yao, Y.; Chen, Y.; Zeng, Y.; Lacey, S.D.; Li, Y.; Wang, Y.; Dai, J.; Wang, Y.; et al. Thermoelectric properties and performance of flexible reduced graphene oxide films up to 3000 K. *Nat. Energy* **2018**, *3*, 148–156. [CrossRef]
13. Kim, S.L.; Hsu, J.-H.; Yu, C. Intercalated graphene oxide for flexible and practically large thermoelectric voltage generation and simultaneous energy storage. *Nano Energy* **2018**, *48*, 582–589. [CrossRef]
14. Huang, L.; Lu, J.; Ma, D.; Ma, C.; Zhang, B.; Wang, H.; Wang, G.; Gregory, D.H.; Zhou, X.; Han, G. Facile in situ solution synthesis of SnSe/rGO nanocomposites with enhanced thermoelectric performance. *J. Mater. Chem. A* **2020**, *8*, 1394–1402. [CrossRef]
15. Wang, L.; Xin, B.; Elsukova, A.; Eklund, P.; Solin, N. Mechanochemical Formation of Protein Nanofibril: Graphene Nanoplatelet Hybrids and Their Thermoelectric Properties. *ACS Sustain. Chem. Eng.* **2020**, *8*, 17368–17378. [CrossRef]
16. Li, D.; Gong, Y.; Chen, Y.; Lin, J.; Khan, Q.; Zhang, Y.; Li, Y.; Zhang, H.; Xie, H. Recent Progress of Two-Dimensional Thermoelectric Materials. *Nano-Micro Lett.* **2020**, *12*, 36. [CrossRef]

17. Nolas, G.S.; Sharp, J.; Goldsmid, H.J. *Thermoelectrics*; Springer Series in Materials Science; Springer: Berlin/Heidelberg, Germany, 2001; Volume 45, ISBN 9783642074516.

18. Zong, P.; Liang, J.; Zhang, P.; Wan, C.; Wang, Y.; Koumoto, K. Graphene-Based Thermoelectrics. *ACS Appl. Energy Mater.* **2020**, *3*, 2224–2239. [CrossRef]

19. Drozdova, M.; Hussainova, I.; Pérez-Coll, D.; Aghayan, M.; Ivanov, R.; Rodríguez, M.A. A novel approach to electroconductive ceramics filled by graphene covered nanofibers. *Mater. Des.* **2016**, *90*, 291–298. [CrossRef]

20. Ivanov, R.; Hussainova, I.; Aghayan, M.; Drozdova, M.; Pérez-Coll, D.; Rodríguez, M.A.; Rubio-Marcos, F. Graphene-encapsulated aluminium oxide nanofibers as a novel type of nanofillers for electroconductive ceramics. *J. Eur. Ceram. Soc.* **2015**, *35*, 4017–4021. [CrossRef]

21. Ivanov, R.; Mikli, V.; Kübarsepp, J.; Hussainova, I. Direct CVD Growth of Multi-Layered Graphene Closed Shells around Alumina Nanofibers. *Key Eng. Mater.* **2016**, *674*, 77–80. [CrossRef]

22. Hussainova, I.; Shamshirgar, A.S.; Ivanov, R.; Volobujeva, O.; Romanov, A.E.; Gasik, M. Directional conductivity in layered alumina. *Curr. Appl. Phys.* **2020**. [CrossRef]

23. Venezuela, P.; Lazzeri, M.; Mauri, F. Theory of double-resonant Raman spectra in graphene: Intensity and line shape of defect-induced and two-phonon bands. *Phys. Rev. B* **2011**, *84*, 035433. [CrossRef]

24. Eckmann, A.; Felten, A.; Mishchenko, A.; Britnell, L.; Krupke, R.; Novoselov, K.S.; Casiraghi, C. Probing the Nature of Defects in Graphene by Raman Spectroscopy. *Nano Lett.* **2012**, *12*, 3925–3930. [CrossRef]

25. Ferrari, A.C. Raman spectroscopy of graphene and graphite: Disorder, electron–phonon coupling, doping and nonadiabatic effects. *Solid State Commun.* **2007**, *143*, 47–57. [CrossRef]

26. Ferrari, A.C.; Basko, D.M. Raman spectroscopy as a versatile tool for studying the properties of graphene. *Nat. Nanotechnol.* **2013**, *8*, 235–246. [CrossRef]

27. Tsoukleri, G.; Parthenios, J.; Papagelis, K.; Jalil, R.; Ferrari, A.C.; Geim, A.K.; Novoselov, K.S.; Galiotis, C. Subjecting a Graphene Monolayer to Tension and Compression. *Small* **2009**, *5*, 2397–2402. [CrossRef]

28. Mohiuddin, T.M.G.; Lombardo, A.; Nair, R.R.; Bonetti, A.; Savini, G.; Jalil, R.; Bonini, N.; Basko, D.M.; Galiotis, C.; Marzari, N.; et al. Uniaxial strain in graphene by Raman spectroscopy: G peak splitting, Grüneisen parameters, and sample orientation. *Phys. Rev. B* **2009**, *79*, 205433. [CrossRef]

29. Saito, R.; Hofmann, M.; Dresselhaus, G.; Jorio, A.; Dresselhaus, M.S. Raman spectroscopy of graphene and carbon nanotubes. *Adv. Phys.* **2011**, *60*, 413–550. [CrossRef]

30. Stamatin, S.N.; Hussainova, I.; Ivanov, R.; Colavita, P.E. Quantifying Graphitic Edge Exposure in Graphene-Based Materials and Its Role in Oxygen Reduction Reactions. *ACS Catal.* **2016**, *6*, 5215–5221. [CrossRef]

31. Pisana, S.; Lazzeri, M.; Casiraghi, C.; Novoselov, K.S.; Geim, A.K.; Ferrari, A.C.; Mauri, F. Breakdown of the adiabatic Born–Oppenheimer approximation in graphene. *Nat. Mater.* **2007**, *6*, 198–201. [CrossRef] [PubMed]

32. Das, A.; Pisana, S.; Chakraborty, B.; Piscanec, S.; Saha, S.K.; Waghmare, U.V.; Novoselov, K.S.; Krishnamurthy, H.R.; Geim, A.K.; Ferrari, A.C.; et al. Monitoring dopants by Raman scattering in an electrochemically top-gated graphene transistor. *Nat. Nanotechnol.* **2008**, *3*, 210–215. [CrossRef] [PubMed]

33. Schwan, J.; Ulrich, S.; Batori, V.; Ehrhardt, H.; Silva, S.R.P. Raman spectroscopy on amorphous carbon films. *J. Appl. Phys.* **1996**, *80*, 440–447. [CrossRef]

34. Ferrari, A.C.; Robertson, J. Origin of the 1150-cm^{-1} Raman mode in nanocrystalline diamond. *Phys. Rev. B* **2001**, *63*, 121405. [CrossRef]

35. Lee, A.Y.; Yang, K.; Anh, N.D.; Park, C.; Lee, S.M.; Lee, T.G.; Jeong, M.S. Raman study of D* band in graphene oxide and its correlation with reduction. *Appl. Surf. Sci.* **2021**, *536*, 147990. [CrossRef]

36. Kaniyoor, A.; Ramaprabhu, S. A Raman spectroscopic investigation of graphite oxide derived graphene. *AIP Adv.* **2012**, *2*, 032183. [CrossRef]

37. Inam, F.; Yan, H.; Peijs, T.; Reece, M.J. The sintering and grain growth behaviour of ceramic–carbon nanotube nanocomposites. *Compos. Sci. Technol.* **2010**, *70*, 947–952. [CrossRef]

38. Lamouri, S.; Hamidouche, M.; Bouaouadja, N.; Belhouchet, H.; Garnier, V.; Fantozzi, G.; Trelkat, J.F. Control of the γ-alumina to α-alumina phase transformation for an optimized alumina densification. *Boletín la Soc. Española Cerámica y Vidr.* **2017**, *56*, 47–54. [CrossRef]

39. Aghayan, M.; Hussainova, I.; Gasik, M.; Kutuzov, M.; Friman, M. Coupled thermal analysis of novel alumina nanofibers with ultrahigh aspect ratio. *Thermochim. Acta* **2013**, *574*, 140–144. [CrossRef]

40. Shamshirgar, A.S.; Rojas Hernández, R.E.; Tewari, G.C.; Ivanov, R.; Mikli, V.; Karppinen, M.; Hussainova, I. Layered structure of alumina/graphene-augmented-inorganic-nanofibers with directional electrical conductivity. *Carbon* **2020**, *167*, 634–645. [CrossRef]

41. Casiraghi, C.; Pisana, S.; Novoselov, K.S.; Geim, A.K.; Ferrari, A.C. Raman fingerprint of charged impurities in graphene. *Appl. Phys. Lett.* **2007**, *91*, 233108. [CrossRef]

42. Chase, M.W., Jr. NIST-JANAF Themochemical Tables, 4th Edition. *J. Phys. Chem. Ref. Data* **1998**, 1–1951. [CrossRef]

43. Zhan, G.D.; Kuntz, J.D.; Wang, H.; Wang, C.M.; Mukherjee, A.K. Anisotropic thermal properties of single-wall-carbon-nanotube-reinforced nanoceramics. *Philos. Mag. Lett.* **2004**, *84*, 419–423. [CrossRef]

44.　Amollo, T.A.; Mola, G.T.; Kirui, M.S.K.; Nyamori, V.O. Graphene for Thermoelectric Applications: Prospects and Challenges. *Crit. Rev. Solid State Mater. Sci.* **2018**, *43*, 133–157. [CrossRef]

45.　Chen, G. Thermal conductivity and ballistic-phonon transport in the cross-plane direction of superlattices. *Phys. Rev. B* **1998**, *57*, 14958–14973. [CrossRef]

46.　Oka, N.; Arisawa, R.; Miyamura, A.; Sato, Y.; Yagi, T.; Taketoshi, N.; Baba, T.; Shigesato, Y. Thermophysical properties of aluminum oxide and molybdenum layered films. *Thin Solid Films* **2010**, *518*, 3119–3121. [CrossRef]

47.　Yang, D.J.; Zhang, Q.; Chen, G.; Yoon, S.F.; Ahn, J.; Wang, S.G.; Zhou, Q.; Wang, Q.; Li, J.Q. Thermal conductivity of multiwalled carbon nanotubes. *Phys. Rev. B* **2002**, *66*, 165440. [CrossRef]

48.　Lin, C.-J.; Lin, I.-C.; Tuan, W.-H. Effect of graphene concentration on thermal properties of alumina–graphene composites formed using spark plasma sintering. *J. Mater. Sci.* **2017**, *52*, 1759–1766. [CrossRef]

49.　Ahmad, K.; Wei, P.; Wan, C. Thermal conductivities of alumina-based multiwall carbon nanotube ceramic composites. *J. Mater. Sci.* **2014**, *49*, 6048–6055. [CrossRef]

50.　Swartz, E.T.; Pohl, R.O. Thermal boundary resistance. *Rev. Mod. Phys.* **1989**, *61*, 605–668. [CrossRef]

51.　Ramirez, C.; Leborán, V.; Rivadulla, F.; Miranzo, P.; Osendi, M.I. Thermopower and hall effect in silicon nitride composites containing thermally reduced graphene and pure graphene nanosheets. *Ceram. Int.* **2016**, *42*, 11341–11347. [CrossRef]

List of publications not included in this thesis

V   **Saffar Shamshirgar, A.**, Aghayan, M., Tripathi, T. S., Karppinen, M., Gasik, M., & Hussainova, I. (2018). Time-effective synthesis of rhombohedral CuAlO2 from mesoporous alumina substrate. Materials & Design, 147, 48–55. https://doi.org/10.1016/j.matdes.2018.03.031.

VI   Kamboj, N., **Saffar Shamshirgar, A.**, Shirshneva-Vaschenko, E. V., & Hussainova, I. (2019). Deposition of iron oxide nanoparticles on mesoporous alumina network by wet-combustion technology. Materials Chemistry and Physics, 225340–346. https://doi.org/10.1016/j.matchemphys.2018.12.095.

VII **Saffar Shamshirgar, A.**, Ivanov, R., & Hussainova, I. (2019). Spark plasma sintering of layered γ-Al2O3/graphene reinforced nanocomposites. Proceedings of the Estonian Academy of Sciences, 68(2), 140–144. https://doi.org/10.3176/proc.2019.2.04.

VIII Glukharev, A., Glumov, O., Temnikova, M., **Saffar Shamshirgar, A.**, Kurapova, O., Hussainova, I., & Konakov, V. (2021). YSZ-rGO composite ceramics by spark plasma sintering: The relation between thermal evolution of conductivity, microstructure and phase stability. Electrochimica Acta, 367, 137533. https://doi.org/10.1016/j.electacta.2020.137533

Curriculum vitae

Personal data

Name:	Ali Saffarshamshirgar
Date of birth:	20.01.1986
Place of birth:	Ahvaz
Citizenship:	Iran

Contact data

E-mail:	ali.saffar.sh@gmail.com

Education

2017–2021	Tallinn University of Technology – PhD
2015–2017	Materials and Processes of Sustainable Energetics, Tallinn University of Technology – MSc (Cum Laude)
2006–2009	Electrical Engineering, Azad University, Bushehr, Iran – BSc
2004–2006	Electrical Engineering, Azad University, Bushehr, Iran – A.Eng.
2001–2004	High school – Fatholmobin, Ahvaz, Iran

Language competence

Persian	Native
English	Fluent

Professional employment

2019–2020	FACT Industries CTO/Test and Verification Specialist: Investigation of Additive Manufacturing of Improved Ceramic Packages for Detectors (SiC), European Space Agency (ESA) (Ref. ESA AO/1-9431/19/NL/CRS ESA)
2018–2019	FACT Industries Materials Engineer: FACT-THERM project funded by EIT-Raw Materials Booster (PA15099-BCLC-2018-3)
2013–2015	Petro Tadbir Pars Engineering Company – Oil & Gas R&D Expert
2010–2013	Petro Sina Aria Oil and Gas Company – Oil & Gas R&D Expert – Petrosina Arya is an EPC Contractor for oil, gas, and petrochemical projects

Projects

2020–2024	Bio-replicating Engineering Structures for Tribo-application – PRG643
2020–2023	Enhanced and wavelength-tunable luminescence in nanostructured phosphor films – PSG466
2016–2019	Nanonet of ceramic fibers with targeted functionalities – PUT1063
2017–2019	Multi-scale structured ceramic-based composites for extreme applications – IUT19-29

Research visits

2020 (6 months)	Institute of Ceramics and Glass, Spanish National Research Council (ICV-CSIC), Spain
03.07.2019–06.07.2019	Aalto University, Finland
14.05.2018–20.05.2018	Institute of Advanced Manufacturing Technology, Krakow, Poland
2016–2017	Aalto University, Finland

Elulookirjeldus

Isikuandmed

Nimi:	Ali Saffarshamshirgar
Sünniaeg:	20.01.1986
Sünnikoht:	Ahvaaz
Kodakondsus:	Iraani

Kontaktandmed

E-post:	ali.saffar.sh@gmail.com

Hariduskäik

2017–2021	Tallinna Tehnikaülikool – PhD
2015–2017	Tallinna Tehnikaülikool – MSc (Cum Laude)
2006–2009	Azad University, Bushehr, Iraan – BSc
2004–2006	Azad University, Bushehr, Iraan – A.Eng.
2001–2004	Keskharidus – Fatholmobin, Ahvaaz, Iraan

Keelteoskus

Pärsia keel	Emakeel
Inglise keel	Kõrgtase

Teenistuskäik

2019–2020	FACT Industries
2018–2019	FACT Industries
2013–2015	Petro Tadbir Pars Engineering Company – Nafta ja gaas R&D ekspert
2010–2013	Petro Sina Aria Oil and Gas Company – Nafta ja gaas R&D ekspert

Projektid

2020–2024	PRG643 "Biojäljendatud tehnostruktuurid triboloogilisteks rakendusteks (1.01.2020–31.12.2024)", Irina Hussainova, Tallinna Tehnikaülikool, Inseneriteaduskond, Mehaanika ja tööstustehnika instituut
2020–2023	PSG466 "Suurendatud ning häälestatav luminestsents fosforipõhistes nanostruktuursetes kiledes (EWANUFILMs) (1.09.2020–31.12.2023)", Rocio Estefania Rojas Hernandez, Tallinna Tehnikaülikool, Inseneriteaduskond, Mehaanika ja tööstustehnika instituut
2016–2019	PUT1063 "Keraamika kiudude nanovõrgustik sihitute funktsioonidega (1.01.2016–31.12.2019", Irina Hussainova, Tallinna Tehnikaülikool, Mehaanikateaduskond, Tallinna Tehnikaülikool, Inseneriteaduskond, Mehaanika ja tööstustehnika instituut

2017–2019	IUT19-29 "Mitmeastmeliselt struktureeritud keraamika-baasil komposiitmaterjalid kasutamiseks ekstreemtingimustes (1.01.2014–31.12.2019)", Jakob Kübarsepp, Tallinna Tehnikaülikool, Mehaanikateaduskond, Tallinna Tehnikaülikool, Inseneriteaduskond, Mehaanika ja tööstustehnika instituut

Välismaal teadustöö

2020 (6 kuud)	Institute of Ceramics and Glass, Madrid, Hispaania
03.07.2019– 06.07.2019	Aalto ülikool, Soome
14.05.2018– 20.05.2018	Institute of Advanced Manufacturing Technology, Krakow, Poola
2016–2017	Aalto ülikool, Soome